THE UNIVERSITY OF CHICAGO

UNRAVELING THE NEURAL BASIS OF PREHENSION TO BUILD BETTER BIONIC HANDS

A DISSERTATION SUBMITTED TO

THE FACULTY OF THE DIVISION OF THE BIOLOGICAL SCIENCES

AND THE PRITZKER SCHOOL OF MEDICINE

IN CANDIDACY FOR THE DEGREE OF

DOCTOR OF PHILOSOPHY

COMMITTEE ON COMPUTATIONAL NEUROSCIENCE

BY

ELIZAVETA OKOROKOVA

CHICAGO, ILLINOIS

AUGUST 2023

Table of contents

List of Figures

Acknowledgments

Advisor

Sliman Bensmaia

Thesis Committee

Wim van Drongelen

Nicholas Hatsopoulos

Lee Miller

Current and former Bensmaia Lab members

John Downey

Charles Greenspon

Anton Sobinov

Giacomo Valle

Natalya Shelchkova

Patrick Jordan

Drew Sheets

Rashi Bhatt

Ashley van Driesche

Paul Arters

Holden Higgins

Victoria Arriola

Emily Fitzgerald

Dillan Prasad

Efe Dogruoz

Neema Darabi

Benoit Delhaye

Hannes Saal

James Goodman

Justin Lieber

Katie Long

Aneesha Suresh

Qinpu He

Thierri Callier

Yuke Yan

Collaborators

Matthew Kaufman

Jennifer Collinger

Robert Gaunt

Michael Boninger

Gregory Clark

Jacob George

Lee Fisher

Human participants

Scott Imbrie

Bill Rinaldi

Nathan Copeland

Dom

Monkeys

Bud

Jameson

Bacardi

Daiquiri

Mojito

Pimms

Family and friends

Mom and dad, for giving me everything they could to nurture my scientific curiosity.

Sasha, for showing me the joys of learning outside of books and classrooms.

Miron, for his continuing love and support along this journey.

Ali, for teaching me that the journey is often more valuable than the destination.

Dexter, for bringing infinite happiness to my life.

Abstract

The human hand is a complex and versatile effector that mediates most of our interactions with the environment. The objective of my dissertation is to shed light on the neural mechanisms that mediate manual behavior in human and non-human primates, focusing on three aspects of prehension: postural control, grasp force control, and force feedback. First, we compare neural population responses in the motor cortex during grasp to that of reach and find that neural dynamics associated with grasp are fundamentally different from those associated with reach. During grasp, unlike reach, population responses do not exhibit smooth linear dynamics. Second, we investigate how hand kinematics and interaction forces are encoded in the motor cortex of macaques and develop decoders that accurately track these behavioral variables. We find that linear models can account for the relationship between neural activity in the motor cortex and hand posture but not grasp force. Rather, force signals are weak and more dynamic than postural ones. Capturing these dynamics requires more complex models that can exploit the force-related dynamics.

Next, we use insights gleaned from able-bodied animals to develop real-time kinematic and force decoders for individuals with tetraplegia. We confirm that, while kinematics can be decoded linearly from the motor cortex, grasp force is best decoded by incorporating non-linear dynamics in the human motor cortex, consistent with our results in monkeys. Finally, we develop approaches to incorporate biomimetic sensory feedback into brain-computer interfaces aimed at restoring manual dexterity. To this end, we develop a sensory encoding model – which converts the outputs of sensors on the bionic hand into regimes of electrical stimulation applied to the nerve – designed to mimic biological responses and demonstrate that the resulting feedback is more natural and intuitive. The same algorithm can be seamlessly applied to sensory feedback via interfaces with

the somatosensory cortex. These results pave the way toward biologically inspired brain-computer interfaces that mimic the functionality of biological hands.

Chapter 1 | Introduction: neural mechanisms of hand function and its restoration through neural prosthetics

"*The hand is the window on to the mind."*

- Immanuel Kant

1.1 Anatomy of the hand

The primate hand is a remarkable structure that has evolved over millions of years to enable primates to grasp and manipulate tools with great dexterity (Kivell et al., 2016). The anatomy of the primate hand is characterized by a complex arrangement of bones and muscles that allow for a wide range of movements and functions (Napier, 1993; Sobinov & Bensmaia, 2021).

The human hand consists of 27 bones, including carpal bones, metacarpal bones, and phalanges (Kivell et al., 2016). At the core of the primate hand is the wrist, which is composed of eight small bones called carpals. The carpal bones are connected to the forearm bones, the radius, and the ulna, which allow for movements of the hand and wrist. The metacarpal bones extend from the wrist to the fingers and are responsible for providing support and structure to the hand. In primates, the thumb and fingers have distinct movements and can be moved independently from each other, allowing for precision grip and fine object manipulation. The thumb has two phalanges, while the other four fingers have three phalanges each, providing greater flexibility and range of motion. The bones of the hand are linked together by ligaments and are covered by muscles and tendons.

The primate hand is characterized by a complex system of muscles that allow for the fine movements and precision grip necessary for tool use and other manual activities. These muscles are divided into two groups: intrinsic muscles, which originate within the hand itself, and extrinsic muscles, which originate in the forearm and extend into the hand. The intrinsic muscles of the

hand are responsible for controlling the movements of the fingers and thumb. These muscles are divided into three groups: thenar muscles, hypothenar muscles, and interosseous muscles. The thenar muscles are responsible for moving the thumb, while the hypothenar muscles are responsible for moving the little finger. The extrinsic muscles of the hand are responsible for movements of the wrist and forearm. These muscles are divided into three groups: the flexor muscles, the extensor muscles, and the abductor muscles. The flexor muscles are responsible for bending the fingers and wrist, while the extensor muscles are responsible for straightening them. The abductor muscles are responsible for moving the fingers away from the hand, allowing for a wider grip.

The remarkable dexterity of the primate hand is the result of millions of years of evolution. The earliest primates had hands that were suited for simple prehensile behaviors, such as climbing, however, over time primate hands evolved for more advanced tool use. This evolution was driven by the development of the opposable thumb (Figure 1.1), which allowed for precision grip and fine object manipulation. While various degrees of opposability exist across primates, only humans possess fully opposable thumbs. Full opposability is facilitated by the relatively long length of the human thumb, which allows for broad contact between the pads of the thumb and other fingers. Although non-primate animals also possess prehensile abilities and opposing digits, none exhibit the intricate movements of the primate thumb (Sobinov & Bensmaia, 2021).

1.2 Neural control of the hand

1.2.1 Lateral corticospinal tract

The lateral corticospinal tract, also known as the pyramidal tract, is the primary descending pathway responsible for voluntary hand movements (Lemon, 2008; Welniarz et al., 2017). This tract originates in the primary motor cortex (M1) and consists of axons of motor neurons that travel

through the brainstem down the spinal cord. At the level of the medulla, most of these axons cross over to the contralateral side and continue through the lateral funiculus of the spinal cord to synapse directly or indirectly through spinal interneurons in the ventral horn to the target muscle fibers. The corticospinal tract has evolved in nonhuman primates and humans to have an increased number of directly connected motoneurons, which is thought to correlate with manual dexterity (Figure 1.1) (Courtine et al., 2007; Heffner & Masterton, 1975; Lemon, 2008; Rathelot & Strick, 2009; Sobinov & Bensmaia, 2021). Damage to the corticospinal tract results in a permanent loss of fine control of the extremities, which can significantly impair an individual's ability to perform coordinated movements such as playing an instrument or typing on a keyboard. While other descending pathways can recover the function of more coarse movements, they are not able to generate fine, skilled movements.

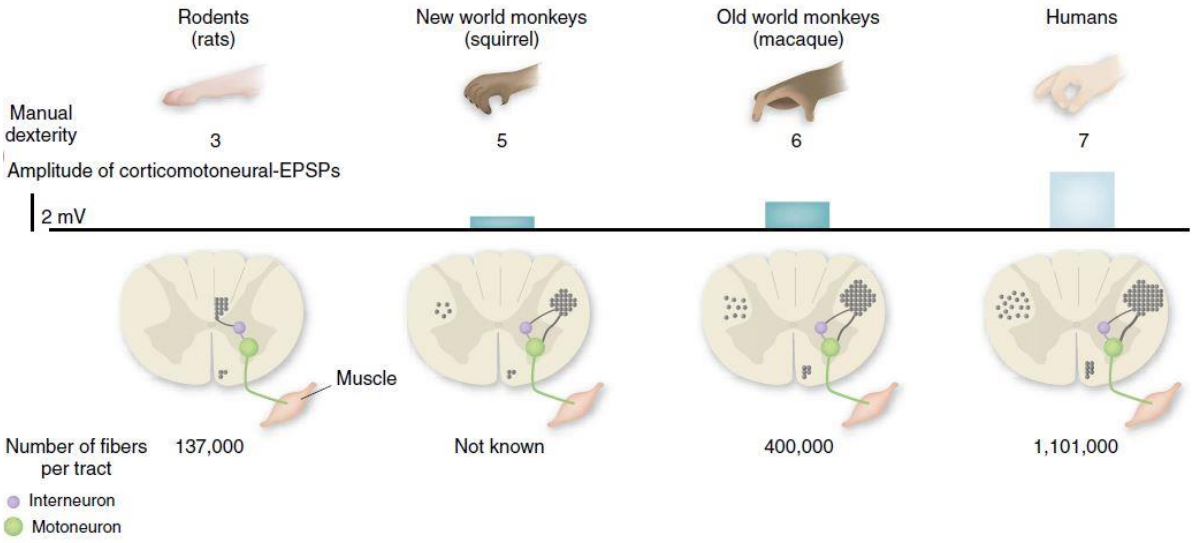

Figure 1.1 – Relationship between the development of the corticospinal tract and fine motor control abilities. In rodents, cortical input is relayed to motor neurons through interneurons, while nonhuman primates and humans also have direct corticospinal connections with motoneurons. The size and number of corticospinal fibers and the amplitude of excitatory postsynaptic potential (EPSP) elicited by cortical neurons on motoneurons have increased during primate evolution. Additionally, the development of the corticospinal tract correlates with improved finger-thumb precision grip abilities. Figure reproduced from Courtine at.al. (2007).

1.2.2 Primary motor cortex

The primary motor cortex (M1, area 4) is organized in a somatotopic manner, in which different areas of the brain contribute to the movement of different parts of the body (Baldwin et al., 2018; Luppino & Rizzolatti, 2000; Penfield & Boldrey, 1937; Rizzolatti & Luppino, 2001; Schieber, 2001). The hand, despite only accounting for a small percentage of the body's weight and surface area, occupies a disproportionately large amount of the motor homunculus in M1, as evidenced by electrical stimulation of M1 (Baldwin et al., 2018; Mayer et al., 2019; Strick et al., 2021). In primates, including humans, other areas of the cortex outside of M1 also correlate with hand movement, suggesting that there is widespread neural circuitry involved in supporting manual control (Baldwin et al., 2018; Sobinov & Bensmaia, 2021).

The function of M1 has been studied for decades, yet principles that underlie the coding structure in the M1 upper limb representation are unclear. Two major (not mutually exclusive) theories prevail in the field of limb motor control. One, often referred to as the representational view, states that motor neurons encode features of motor behavior, such as limb kinematics, direction of movement, or muscle activations. Another popular theory called the dynamical systems perspective, attempts to isolate the basic patterns and their dynamics in the population neural response from which the final output might be built (Churchland et al., 2012; Shenoy et al., 2013). Both theories have been well supported in the studies of the proximal limb movement, the distal limb has received comparatively less attention. M1 activity related to the proximal limb shows a strong response during movement but a weaker response during the maintained posture, while hand-related M1 activity encodes postural changes without a preference for movement (Goodman et al., 2019; E. V. Okorokova et al., 2020). Population responses in M1 exhibit smooth linear dynamics during reaching movements (Churchland et al., 2012), but not during isolated grasping

movements (Suresh et al., 2021). The differences in neuronal activity at the single-cell and population levels may reflect fundamentally different control strategies for arms and hands, or differences in their biomechanics (Sobinov & Bensmaia, 2021).

1.3 Somatosensation: touch and proprioception

Manual dexterity depends not only on sophisticated control of the muscles of the hand that drive movement but also on two sensory modalities of the hand: touch and proprioception. The absence of tactile or proprioceptive feedback in the hand leads to severe motor impairments (Dürr et al., 1996; Sainburg et al., 1993, 1995; Sghirlanzoni et al., 2005; Spinazzi et al., 2010; Valdmanis et al., 2004; Yahya et al., 2019).

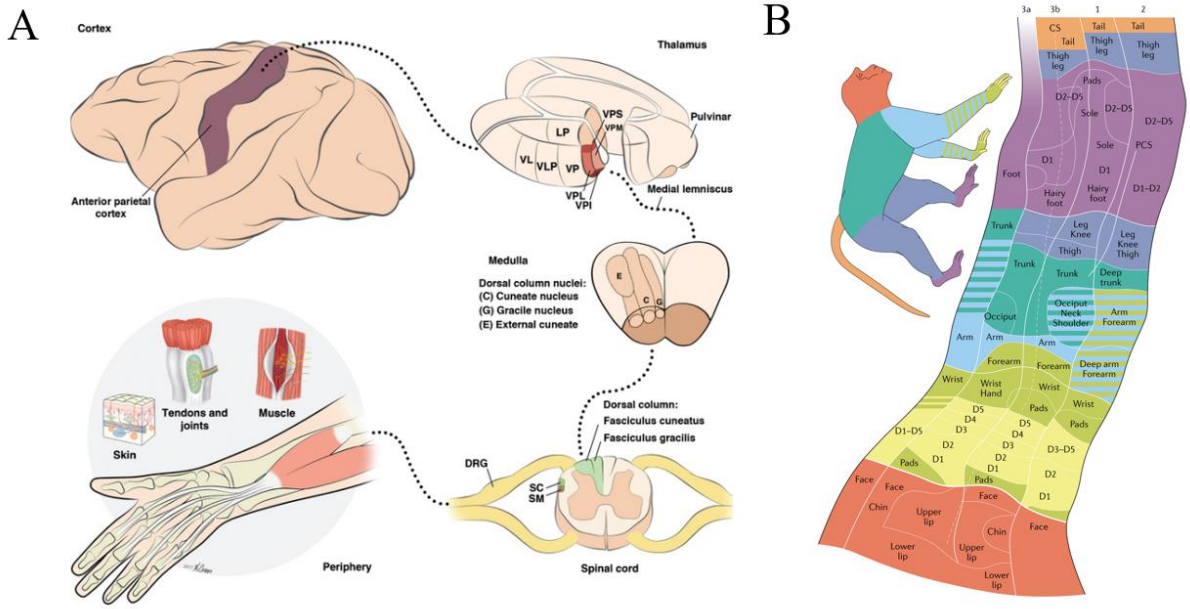

Figure 1.2 – Somatosensory pathways. (A) Afferent fibers originating from the somatosensory periphery bundle in fascicles to form nerves. The cell bodies of these afferent fibers are clustered in the dorsal root ganglia (DRG). Upon entering the spinal cord through the dorsal root, the afferent axons branch out, with one projection extending to the dorsal horn and another projection reaching the dorsal column nuclei (DCN) via the dorsal column. The DCN, in turn, projects contralaterally through the medial lemniscus to the ventroposterior complex of the thalamus, which relays the sensory information to the cortex. Reproduced from Delhaye et al., 2018. (B) Somatotopic organization of areas 3a, 3b, 1 and 2 in primary somatosensory cortex of macaque. Reproduced from Sobinov & Bensmaia, 2021.

The human hand is highly sensitive to tactile stimuli and can detect differences in texture and shape at the nanometer scale. Such sensitivity is facilitated by about 17000 afferents that enervate the skin of the hand (Delhaye et al., 2018; Goodman & Bensmaia, 2018; Sobinov & Bensmaia, 2021). Cutaneous afferents can be split into four categories based on their response properties and receptive field (RF) size. Mechanoreceptors innervated by type I afferents lie close to the surface of the skin and have small and clearly defined RFs, whereas mechanoreceptors innervated by type II afferents are deeper in the skin and have large RFs. Slowly adapting afferents produce a sustained response to a static indentation of the skin, whereas rapidly adapting afferents respond only at the onset and offset of the indentation (Delhaye et al., 2018). The diverse properties of tactile receptors allow us to process a wide range of features of objects we interact with, including shape, curvature, texture, vibrations, and motion.

Proprioceptive afferents, also known as "deep" afferents, are responsive to deep palpation of muscles and joint movements, but not to light touch (Delhaye et al., 2018). They consist of muscle spindle afferents, Golgi tendon organs (GTOs), and joint receptors. Muscle spindles run in parallel with muscle fibers and are sensitive to muscle length and the rate of change of muscle length, which is relevant for tracking changes in limb position and movements. Golgi tendon organs run in series with the muscles and respond to muscle tension, providing information about force and preventing excessive force on the tendon. Afferents that innervate joint receptors mostly respond when joints are in extreme positions of flexion or extension, preventing damage to the body. Integration of information from the three types of afferents allows accurate tracking of limb position and applied forces.

The information gathered by peripheral receptors located in the skin, muscles, and tendons is transmitted via the spinal cord to the brainstem, then to the thalamus, and finally to the primary

and secondary somatosensory cortices (S1, S2) in the brain (Figure 1.2(A)). The somatotopic organization of S1 is highly precise, with a more defined somatotopy compared to the primary motor cortex (Kaas, 1983; Pons et al., 1985; Pons & Kaas, 1986) (Figure 1.2 (B)). As we move along the somatosensory pathway, the cell properties become less specific, resulting in increased complexity of encoded features and receptive field sizes. Such submodality convergence is observed as early as the first synapse in the cuneate nucleus of the brainstem (Suresh et al., 2021).

There is strong evidence of anatomical and functional connectivity between somatosensory and motor cortices in both non-human primates and humans (Brochier et al., 1999; Entz et al., 2014; Osborn et al., 2021; Pons & Kaas, 1986; Shelchkova et al., 2022; Sobinov & Bensmaia, 2021). These connections likely play a role in sensorimotor integration, allowing sensory information to guide and refine motor actions (Scott, 2004).

1.4 Restoring functionality of the hand through Brain-Computer Interfaces

Hand dexterity is an essential component of daily life that allows individuals to interact with their environment. Injuries or diseases, resulting in full of partial loss of hand function have a devastating impact on the quality of life that can deprive individuals of the most basic actions of daily living. Fortunately, brain-computer interfaces have emerged as a promising technology for replacing biological hand functionality with prosthetic devices.

1.4.1 Peripheral neural prosthetics

Nearly 2 million people are living with limb loss in the United States and about 30% of that number are people with upper limb amputations[1]. Hand function can be restored in upper-limb amputees by equipping them with prostheses controlled with signals from residual muscles. In the past years,

[1] https://www.amputee-coalition.org/resources/limb-loss-statistics/#1

there has been a significant advancement in the development of anthropomorphic prosthetic hands that are now capable of replicating the functionality of human hands to a remarkable extent. One of the largest advances in the field has been the development of technologies that are capable of stimulating the residual nerves to elicit tactile sensations in the missing limb (George et al., 2019; Valle et al., 2018). These include implantable slanted Utah electrode arrays, regenerative electrodes, nerve calves, and dorsal root ganglion implants (Figure 1.3(A)) (Saal & Bensmaia, 2015).

1.4.2 Cortical neural prosthetics

Another type of BCIs that can restore a level of independence in paralyzed individuals is cortical neural prosthetics (Figure 1.3(B), Pandarinath & Bensmaia, 2022). These devices allow the user to control an artificial limb by reading out signals from cortical areas such as M1 (primary motor cortex), extracting relevant motor-related information, and translating it to an external device. The state-of-the-art upper limb cortical prosthesis can currently operate only several degrees of freedom simultaneously. These include the robotic arm movement in 3D space, wrist rotation, power grasp, and several discrete types of precision grip (Collinger et al., 2013; Hochberg et al., 2012a; Wodlinger et al., 2014). While certainly impressive, there still needs to be more work done on increasing the number of degrees

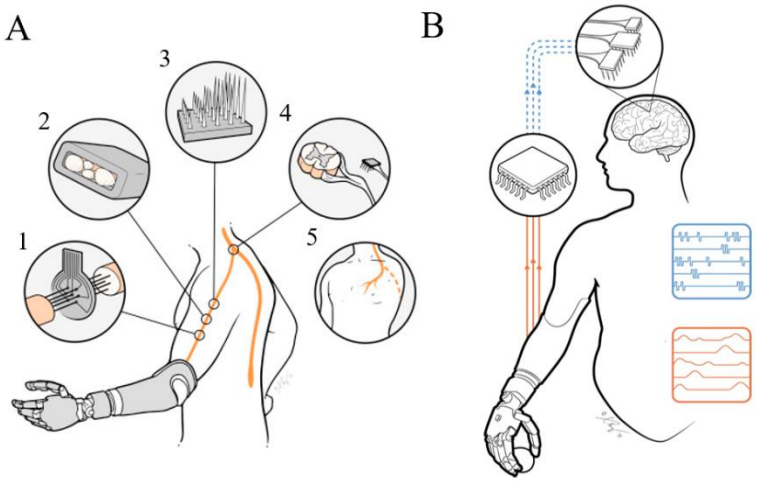

Figure 1.3 – Peripheral and cortical neural prosthetics. (A) Different technologies to restore the sense of touch through a peripheral interface. 1 - Regenerative electrodes. 2 - Extra-fascicular electrodes. 3 - Intra-fascicular electrodes. 4 - Dorsal root ganglion implant. 5 - Targeted sensory reinnervation. Reproduced from Saal & Bensmaia, 2015. (B) Restoring the sense of touch through cortical interface. Signals from sensors on the prosthetic hand are converted into intracortical microstimulation pulse trains delivered to somatosensory cortex. Reproduced from Bensmaia, 2015.

of control, such as individuated finger movement, to achieve hand functionality that could approximate biological human hands. Providing sensory feedback is also possible through electrical stimulation if stimulating arrays are implanted in the somatosensory cortex (Bensmaia & Miller, 2014; Flesher et al., 2016; Pandarinath & Bensmaia, 2022).

1.4.3 Decoding motor commands

A large body of literature is dedicated to various computational techniques for decoding motor commands with neural responses, in both monkeys and humans (Glaser et al., 2020). These methods range from simple models (e.g. linear filters and classifiers, Okorokova et al., 2020), to extremely complicated non-linear cascade techniques that require significant computational resources (Dyer et al., 2017; Pandarinath et al., 2018). The main class of problems that decoders are aimed to answer is stability, robustness to noise, and the ability to translate to online control. Indeed, decoders that work well offline, often fail to generalize to online applications due to the inherent non-stationarily of neural signals and the necessity to operate quickly in the causal regime. (Pandarinath & Bensmaia, 2022)

1.4.4 Towards natural somatosensory feedback

Somatosensory feedback through electrical stimulation has become a common practice in both peripheral and cortical BCI (Bensmaia, 2015; Bensmaia et al., 2023; Bensmaia & Miller, 2014). However, the quality of sensations and, as a result, the functional significance of electrical stimulation is still very far from those of biological hands. One possible solution to improve sensation quality is to increase the spatial specificity of the implantable devices. Alternatively, parameters of stimulation need to be tuned in a way that approximates neural population activation that would mimic that of natural touch (Saal & Bensmaia, 2015). The so-called biomimetic approaches attempt to characterize neural population response during natural hand control and

then mimic them in the patterns of electrical stimulation (E. V. Okorokova et al., 2018). Such biomimetic approaches have already proved fruitful in both peripheral and cortical BCIs (George et al., 2019; Greenspon et al., 2023; Valle et al., 2018).

As BCIs continue to advance, they hold the promise of transforming the lives of millions of individuals worldwide who have lost their hand function. Further research and development are necessary to fully realize the potential of these technologies and make them widely available to those who need them.

1.5 References

Bensmaia, S. J. (2015). Biological and bionic hands: Natural neural coding and artificial perception. *Philosophical Transactions of the Royal Society B: Biological Sciences*, *370*(1677), 20140209. https://doi.org/10.1098/rstb.2014.0209

Bensmaia, S. J., & Miller, L. E. (2014). Restoring sensorimotor function through intracortical interfaces: Progress and looming challenges. *Nature Reviews Neuroscience*, *15*(5), Article 5. https://doi.org/10.1038/nrn3724

Bensmaia, S. J., Tyler, D. J., & Micera, S. (2023). Restoration of sensory information via bionic hands. *Nature Biomedical Engineering*, *7*(4), Article 4. https://doi.org/10.1038/s41551-020-00630-8

Churchland, M. M., Cunningham, J. P., Kaufman, M. T., Foster, J. D., Nuyujukian, P., Ryu, S. I., & Shenoy, K. V. (2012). Neural population dynamics during reaching. *Nature*, *487*(7405), 51–56. https://doi.org/10.1038/nature11129

Courtine, G., Bunge, M. B., Fawcett, J. W., Grossman, R. G., Kaas, J. H., Lemon, R., Maier, I., Martin, J., Nudo, R. J., Ramon-Cueto, A., Rouiller, E. M., Schnell, L., Wannier, T., Schwab, M. E., & Edgerton, V. R. (2007). Can experiments in nonhuman primates expedite the translation of treatments for spinal cord injury in humans? *Nature Medicine*, *13*(5), Article 5. https://doi.org/10.1038/nm1595

Delhaye, B. P., Long, K. H., & Bensmaia, S. J. (2018). Neural Basis of Touch and Proprioception in Primate Cortex. *Comprehensive Physiology*, *8*(4), 1575–1602. https://doi.org/10.1002/cphy.c170033

Dyer, E. L., Gheshlaghi Azar, M., Perich, M. G., Fernandes, H. L., Naufel, S., Miller, L. E., & Körding, K. P. (2017). A cryptography-based approach for movement decoding. *Nature Biomedical Engineering*, *1*(12), Article 12. https://doi.org/10.1038/s41551-017-0169-7

George, J. A., Kluger, D. T., Davis, T. S., Wendelken, S. M., Okorokova, E. V., He, Q., Duncan, C. C., Hutchinson, D. T., Thumser, Z. C., Beckler, D. T., Marasco, P. D., Bensmaia, S. J., & Clark, G. A. (2019). Biomimetic sensory feedback through peripheral nerve stimulation improves dexterous use of a bionic hand. *Science Robotics*, *4*(32). https://doi.org/10.1126/scirobotics.aax2352

Glaser, J. I., Benjamin, A. S., Chowdhury, R. H., Perich, M. G., Miller, L. E., & Kording, K. P. (2020). *Machine learning for neural decoding* (arXiv:1708.00909). arXiv. https://doi.org/10.48550/arXiv.1708.00909

Greenspon, C. M., Valle, G., Hobbs, T. G., Verbaarschot, C., Callier, T., Shelchkova, N. D., Sobinov, A. R., Jordan, P. M., Weiss, J. M., Fitzgerald, E. E., Prasad, D., Driesche, A. van, Lee, R. C., Satzer, D., Gonzalez-Martinez, J., Warnke, P. C., Miller, L. E., Boninger, M. L., Collinger, J. L., …

Bensmaia, S. J. (2023). *Biomimetic Multi-channel Microstimulation of Somatosensory Cortex Conveys High Resolution Force Feedback for Bionic Hands* (p. 2023.02.18.528972). bioRxiv. https://doi.org/10.1101/2023.02.18.528972

Kivell, T. L., Lemelin, P., Richmond, B. G., & Schmitt, D. (Eds.). (2016). *The Evolution of the Primate Hand: Anatomical, Developmental, Functional, and Paleontological Evidence*. Springer. https://doi.org/10.1007/978-1-4939-3646-5

Lemon, R. N. (2008). Descending pathways in motor control. *Annual Review of Neuroscience*, *31*, 195–218. https://doi.org/10.1146/annurev.neuro.31.060407.125547

Napier, J. R. (1993). *Hands*. Princeton University Press.

Okorokova, E. V., Goodman, J. M., Hatsopoulos, N. G., & Bensmaia, S. J. (2020). Decoding hand kinematics from population responses in sensorimotor cortex during grasping. *Journal of Neural Engineering*, *17*(4), 046035. https://doi.org/10.1088/1741-2552/ab95ea

Okorokova, E. V., He, Q., & Bensmaia, S. J. (2018). Biomimetic encoding model for restoring touch in bionic hands through a nerve interface. *Journal of Neural Engineering*, *15*(6), 066033. https://doi.org/10.1088/1741-2552/aae398

Pandarinath, C., O'Shea, D. J., Collins, J., Jozefowicz, R., Stavisky, S. D., Kao, J. C., Trautmann, E. M., Kaufman, M. T., Ryu, S. I., Hochberg, L. R., Henderson, J. M., Shenoy, K. V., Abbott, L. F., & Sussillo, D. (2018). Inferring single-trial neural population dynamics using sequential auto-encoders. *Nature Methods*, *15*(10), 805–815. https://doi.org/10.1038/s41592-018-0109-9

Rathelot, J.-A., & Strick, P. L. (2009). Subdivisions of primary motor cortex based on cortico-motoneuronal cells. *Proceedings of the National Academy of Sciences*, *106*(3), 918–923. https://doi.org/10.1073/pnas.0808362106

Scott, S. H. (2004). Optimal feedback control and the neural basis of volitional motor control. *Nature Reviews Neuroscience*, *5*(7), Article 7. https://doi.org/10.1038/nrn1427

Shenoy, K. V., Sahani, M., & Churchland, M. M. (2013). Cortical control of arm movements: A dynamical systems perspective. *Annual Review of Neuroscience*, *36*, 337–359. https://doi.org/10.1146/annurev-neuro-062111-150509

Sobinov, A. R., & Bensmaia, S. J. (2021). The neural mechanisms of manual dexterity. *Nature Reviews. Neuroscience*, *22*(12), 741–757. https://doi.org/10.1038/s41583-021-00528-7

Suresh, A. K., Greenspon, C. M., He, Q., Rosenow, J. M., Miller, L. E., & Bensmaia, S. J. (2021). Sensory computations in the cuneate nucleus of macaques. *Proceedings of the National Academy of Sciences*, *118*(49), e2115772118. https://doi.org/10.1073/pnas.2115772118

Valle, G., Mazzoni, A., Iberite, F., D'Anna, E., Strauss, I., Granata, G., Controzzi, M., Clemente, F., Rognini, G., Cipriani, C., Stieglitz, T., Petrini, F. M., Rossini, P. M., & Micera, S. (2018). Biomimetic Intraneural Sensory Feedback Enhances Sensation Naturalness, Tactile Sensitivity, and Manual Dexterity in a Bidirectional Prosthesis. *Neuron*, *100*(1), 37-45.e7. https://doi.org/10.1016/j.neuron.2018.08.033

Chapter 2 | Decoding hand kinematics from population responses in sensorimotor cortex during grasping[2]

2.1 Abstract

Objective. The hand—a complex effector comprising dozens of degrees of freedom of movement—endows us with the ability to flexibly, precisely, and effortlessly interact with objects. The neural signals associated with dexterous hand movements in primary motor cortex (M1) and somatosensory cortex (SC) have received comparatively less attention than have those associated with proximal upper limb control. *Approach.* To fill this gap, we trained two monkeys to grasp objects varying in size and shape while tracking their hand postures and recording single-unit activity from M1 and SC. We then decoded their hand kinematics across tens of joints from population activity in these areas. *Main results.* We found that we could accurately decode kinematics with a small number of neural signals and that different cortical fields carry different amounts of information about hand kinematics. In particular, neural signals in rostral M1 led to better performance than did signals in caudal M1, whereas Brodmann's area 3a outperformed areas 1 and 2 in SC. Moreover, decoding performance was higher for joint angles than joint angular velocities, in contrast to what has been found with proximal limb decoders. Significance. We conclude that cortical signals can be used for dexterous hand control in brain machine interface applications and that postural representations in SC may be exploited via intracortical stimulation to close the sensorimotor loop.

[2] This chapter was published: Okorokova, E. V., Goodman, J. M., Hatsopoulos, N. G., & Bensmaia, S. J. (2020). Decoding hand kinematics from population responses in sensorimotor cortex during grasping. Journal of Neural Engineering, 17(4), 046035. https://doi.org/10.1088/1741-2552/ab95ea Supplementary materials are available online.

2.2 Introduction

The hand, a complex effector comprising dozens of degrees of freedom (Belić & Faisal, 2015), allows us to flexibly, precisely, and effortlessly manipulate objects. The loss of hand function—as a consequence of spinal cord injury, for example—can have devastating consequences on quality of life (K. D. Anderson, 2004). In patients whose sensorimotor cortex is intact, some measure of independence can be restored with brain-machine interfaces (BMIs) that tap into the central neural pathways mediating manual dexterity (Bensmaia & Miller, 2014). Translating patterns of neural population activity into control signals for external devices is critical to advance such interfaces.

Reach-to-grasp movements have been traditionally decoded from cortical areas associated with the planning and execution of movement. Primary motor, premotor, and posterior parietal cortices have been the main targets of previous BMIs, yielding remarkable control of a robotic limb in both non-human primates (Lebedev et al., 2005; Mulliken et al., 2008; Velliste et al., 2008; Wessberg et al., 2000) and human tetraplegic patients (Hochberg et al., 2012b; S.-P. Kim et al., 2008, 2011; Wodlinger et al., 2014). However, the focus of most decoding studies has been on reaching movements performed by the proximal limb (elbow and shoulder) (Dyer et al., 2017; Gilja et al., 2012). The distal limb (wrist and finger joints), critical to object interactions, has received comparatively little attention (but see Menz et al., 2015) primarily due to the greater complexity of manual behavior (Ingram et al., 2008) and the difficulty of simultaneously tracking tens of hand joints (Schaffelhofer & Scherberger, 2012).

A critical complement to neural signals involved in controlling movements are signals responsible for conveying sensory feedback about the consequences of those movements (Scott, 2004). Indeed, the motor apparatus receives continuous proprioceptive feedback from joints and muscles that signal the position of body in space, the forces it exerts, and mediates error-corrective motor

adjustments (Soechting & Flanders, 1989). Proprioceptive impairments lead to major deficits in motor behavior, leading to slow, effortful, and imprecise movements (Cole & Sedgwick, 1992; Ghez & Sainburg, 1995; Sainburg et al., 1995). Two cortical fields in somatosensory cortex (SC)—Brodmann's areas 3a and 2 (Krubitzer et al., 2004; Pons & Kaas, 1986) — contain neurons that respond to active and passive manipulation of joints and muscles (Gardner & Costanzo, 1981; London & Miller, 2013; Prud'homme & Kalaska, 1994), to forces applied by the muscles, and to torques applied to the joints (Fromm & Evarts, 1982). However, the vast majority of previous studies of proprioceptive representations in SC have focused on the proximal limb, particularly during reaching movements.

Hand-related responses of individual SC neurons have been characterized during passive deflections of the hand joints (Costanzo & Gardner, 1981; Gardner & Costanzo, 1981) and during active hand movements (Goodman et al., 2019). However, the degree to which hand movements and postures are encoded across populations of SC neurons has not been investigated. One way to address this question is by assessing our ability to decode hand kinematics from the responses of populations of SC neurons. Earlier decoding studies focused on the transport component (i.e. reaching), which primarily involves the proximal limb (Farrokhi & Erfanian, 2018; Glaser et al., 2020; Weber et al., 2011). Those that incorporated distal-limb movements either attempted to classify a small set of discrete hand postures (Branco et al., 2017) or to decode (1-dimensional) continuous grip aperture or grip force (Carmena et al., 2003). To the extent that somatosensory neurons carry detailed information about hand movements, these neural representations might be exploited to convey artificial proprioceptive feedback through intracortical microstimulation (ICMS) (Armenta Salas et al., 2018; London et al., 2008; Tomlinson & Miller, 2016), paralleling efforts to convey artificial tactile feedback through ICMS (Bensmaia, 2015; Flesher et al., 2016).

The goal of the present study is to assess the degree to which hand kinematics can be decoded from the responses of populations of sensorimotor neurons, the main novelty being the attempt to decode hand state from SC. To this end, we trained two monkeys to grasp 35 objects of varying sizes, shapes and orientations, while tracking their time-varying hand kinematics using a camera-based motion tracking system. We simultaneously recorded the responses in the hand representations of M1 and SC using chronically implanted electrode arrays. We then inferred object identity (referred henceforth as 'classification') as well as continuous joint kinematics (referred henceforth as 'decoding') from neural signals while the hand preshaped to grasp an object (before contact). First, we show that neural signals in both M1 and SC carry faithful representations of the hand by using these signals to classify objects before they are grasped or to reconstruct time-varying joint trajectories. Second, we show that different cortical fields in M1 and SC carry different amounts of information about hand state. Finally, we find that we can better decode posture than movement, in contrast to what has been shown for motor representations of the proximal limb, suggesting possible differences in cortical encoding for proximal and distal limb. Our results underscore the promise of using M1 signals to achieve control of the hand during grasping in a BMI setting and demonstrate that SC populations carry a faithful representation of time-varying hand configuration that could in principle be exploited to restore proprioception through ICMS.

2.3 Methods

2.3.1 Animals and surgery

We took recordings from two male Rhesus macaques ranging in age between 6 and 15 years and weighing between 8 and 11 kg. Monkey 2 was implanted twice (monkey 2a and 2b) with an interval of 2 years between recording periods and using different recording techniques. All animal

procedures were performed in accordance with the rules and regulations of the University of Chicago Animal Care and Use Committee. Monkeys received care from a full-time husbandry staff, and a full-time veterinary staff monitored animals' health.

Surgical procedures consisted of implantation of a head-fixing post onto the skull, craniotomy, implantation of a sealed recording chamber (monkey 2a), and implantation of Utah electrode arrays (UEAs, Blackrock Microsystems, Inc. Salt Lake City, UT, monkeys 1 and 2b) and floating microelectrode arrays (FMAs, Microprobes for life science, Gaithersburg, MD; monkey 1) or of semi-chronic Microdrive electrode arrays (Gray Matter Research, Bozeman, MT (Dotson et al.,

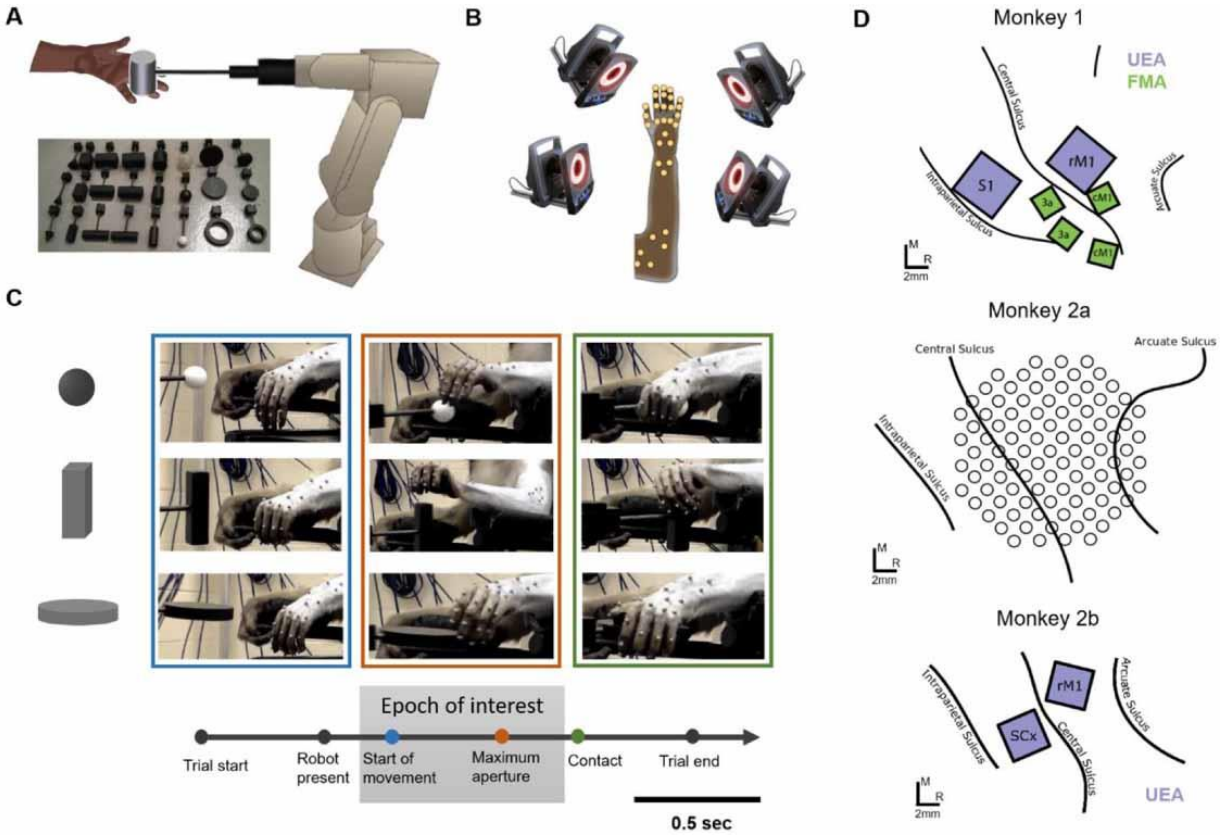

Figure 2.1 - Behavioral task and experimental set-up. (A) Experimental apparatus. On each trial, a robotic arm presented the animal one of 35 objects (inset, supplementary figure 1 and supplementary table 1). (B) Motion tracking. We placed 30 reflective markers on the animal's joints and tracked their 3D position with a 14-camera Vicon motion tracking system. For joint names and locations, see supplementary figure 2. (C) Trial structure. We focused our analysis on the interval from the start of monkey's hand movement until just before contact with the object. Images show hand postures at the start of movement (blue box), at maximum aperture (orange box), and during grasp (green box) for three example objects. (D) Array placement: Utah electrode arrays (UEA, purple, monkey 1 and 2b), floating microelectrode arrays (FMA, green, monkey 1), and Gray Matter array (monkey 2a). For sample sizes, see supplementary table 2. R: rostral, M: medial.

2017; Gray et al., 2007); monkey 2a). All procedures were performed under aseptic conditions and anesthesia induced with ketamine HCl (20 mg kg–1, IM) and maintained with isoflurane (10–25 mg kg–1 per hour, inhaled).

2.3.2 Behavioral task

We trained monkeys to grasp 35 objects varying in shape, size, and orientation to induce a wide range of hand postures (Figure 2.1A, inset and supplementary figure 1). Throughout the session, the head-fixed monkey sat in a chair facing a three DoF robotic arm (Figure 2.1A, top). The arm of the monkey rested on the cushioned armrest and remained largely immobile during the grasp. At the beginning of each trial, an object was attached to the robotic arm using a weak magnet and presented to the animal. The monkey's task was to grasp the object and exert enough grip force so that, when the robot retracted, the object would be disengaged from its magnetic coupling with the robot and remain in the monkey's hand (Figure 2.1C). Animals were trained to keep their elbow on the armrest to minimize movements of the proximal limb. Motionlessness of the proximal limb was enforced by a photosensor embedded into the armrest that triggered an early, unrewarded end to a trial if the arm was lifted to expose it to light.

2.3.3 Kinematics

We recorded hand and elbow kinematics using a camera-based motion tracking system (Vantage, VICON, Los Angeles, CA). To this end, we placed 30 reflective markers on the joints of the hand, wrist, and proximal limb (Figure 2.1B, Online supplementary figure 2). Ten cameras were used to capture the kinematics of the first monkey at a rate of 250 Hz, and fourteen cameras were used to capture the kinematics of the second monkey at a rate of 100 Hz. We then labeled each marker using Nexus software (VICON, Los Angeles, CA) and performed inverse kinematics (OpenSim, Delp et al., 2007) from the resulting time-varying marker positions to infer time-varying joint

angles of the limb (22 DoFs for monkey 1 and 30 DoFs for monkey 2). Joint angles were smoothed with a 50-ms moving average and the angular velocities were computed from these. For each trial, we identified the start of movement (finger and wrist), maximum aperture of fingers, and contact with an object (finger and palm). For monkey 1, we labeled these events manually for all trials. For monkey 2, we only labeled a subset of trials and then used joint angular kinematic trajectories spanning 200 ms before and after each frame as features to train a multi-class linear discriminant classifier to discriminate among 6 classes: all events of interest and 'no event'. The log likelihood ratio was used to determine which of the events was more probable relative to 'no event'. Additional constraints were imposed to ensure that start of movement preceded maximum aperture and maximum aperture preceded grasp. Among all sessions of monkey 2, the mean and the standard error of the model deviation from hand-labeled events were 16 ± 9.5 ms for start of finger movement, 21 ± 8.8 ms for start of wrist movement, 11 ± 8.8 ms for maximum aperture, –25 ± 9.7 ms for palm contact with an object, and –48 ± 12.1 ms for finger contact with an object.

Across trials and objects, the mean interval ± standard deviation between the start of wrist movement and maximum aperture was 524 ± 164 ms, 466 m ± 70 ms and 426 ± 110 ms and that between maximum aperture and first contact with fingers was 273 ± 115 ms, 447 ± 24 ms, 114 ± 43 ms, for monkeys 1, 2a and 2b, respectively.

2.3.4 Electrophysiology

We recorded neural signals from monkeys 1 and 2b using UEAs placed in the pre- and post-central gyri and, for monkey 1, from FMAs placed in the posterior and anterior banks of the central sulcus (Figure 2.1D). For monkey 2a, we recorded neural signals using arrays of depth-adjustable electrodes (SC96) positioned over the central sulcus (Figure 2.1D). We used offline spike sorting

(Offline Sorter, Plexon, Dallas, TX) to remove non-spike threshold crossings and isolate individual units in the high-pass filtered signal.

Motor units recorded from the crest of the precentral gyrus were classified as rostral M1 (rM1), whereas those recorded from the depth of the anterior bank of the central sulcus were classified as caudal M1 (cM1) (Rathelot & Strick, 2009). The provenance of somatosensory units was defined by anatomical location and manual functional mapping prior to recordings (as previously described in (Goodman et al., 2019)).

2.3.5 Neural data preprocessing

Time-varying firing rates of all recorded neurons were computed by summing all events in 10-ms bins. We then soft-normalized the firing rates (divided by their range plus a small increment) and convolved the resulting rates with a Gaussian kernel with a standard deviation of 15 ms.

2.3.6 Session stitching

To achieve a sufficient sample size from each cortical field, we pooled data from all sessions for each monkey (Online supplementary table 2). To this end, we first aligned the kinematics from each condition (object) to maximum hand aperture. Then, we eliminated trials on which the animal adopted a grasping strategy for a given object that was different from that used for that same object on other trials to ensure that the pooled neuronal responses were associated with similar kinematics. Specifically, we discarded trials on which any one time-varying joint angle trajectory exhibited a correlation with its time-varying trial-averaged angle that was lower than 0.7. The remaining kinematics were consistent enough from trial to trial to warrant averaging across trials. We then used the average kinematic traces from 600 ms before maximum aperture to just before finger contact with an object, estimated as an average time to finger contact within each monkey (273, 447 and 114 ms for monkeys 1, 2a, 2b, respectively).

2.3.7 Classification

To assess the degree to which grasping different objects involved different patterns of kinematics and neuronal activity, we attempted to classify the 35 objects using either kinematics or neural data. Specifically, we used multiclass linear discriminant analysis, where the independent variables were the mean joint position or neuronal activity over an interval spanning 150 ms before finger contact with the object, when the hand had nearly reached its final posture before grasp. We trained the classifier using all but one randomly selected trial from each class (object) and tested it on the left-out trial. We performed the random trial selection 10 times and reported mean performance across folds.

2.3.8 Decoding

For continuous decoding, we fit the standard Kalman filter to all recorded joints. The Kalman filter comprises two estimates of some variable, x_t, which in our case was a joint angle or joint angular velocity at some time t. These estimates are:

$$\hat{x}_t^k = Ax_{t-1} + q_t \quad 2.1$$

$$\hat{x}_t^n = Bz_t + w_t \quad 2.2$$

where $\hat{x}_t^k$ is the estimate of x_t based on past kinematics; A is a state transition matrix; q_t is a Gaussian process with zero mean and covariance matrix Q; $\hat{x}_t^n$ is an estimate of x_t based on current neural activity; z_t is observed spiking activity with accumulated lags/leads over interval $\tau \in [-150, 150]$ ms for acausal filters and $\tau \in [-150, 0]$ ms for causal ones, in steps of 30 ms; B is an observation model matrix; and w_t is a Gaussian process with zero mean and covariance matrix W. We used a fusion algorithm to obtain a single best estimate of x_t for each time t (see details in Faragher, 2012; Okorokova et al., 2015).

To obtain filter parameters (A,B,Q,W), we fit the model using 80% of randomly selected trials, validated the hyperparameters on half of the remaining trials (10%), and gauged model performance on the other half (10%). We used L2-norm regularization, which penalizes the L2-norm of matrix B by an amount determined by a hyperparameter, λ. Performance was assessed using the coefficient of determination (R^2). To compare our results to previous ones, we also computed Pearson's correlation and the normalized Root Mean Squared Error (rRMSE), prediction error expressed as a proportion of the joint's range of motion (see Menz et al., 2015 for details and Online supplementary figure 3).

2.3.9 Optimal single-lag latency

To find the optimal asynchrony between kinematics and neural responses, we tested the model with neural data shifted relative to kinematics to different degrees (at +-250 ms, +-200 ms, +-150 ms, +-90 ms, +-50 ms, +-3 ms, +-2 ms, +-1 ms, 0 ms) using a single-lag model and a causal filter (half Gaussian kernel). We then found the lag or lead at which cross-validated performance was highest for each joint. We used this lag/lead across all joints for each single-lag model. Asynchronies were optimized separately for posture and movement.

2.3.10 Controls

In a Kalman filter, the autocorrelation in the observed process is captured by matrix A in equation 2.1. To control for the possibility that kinematics were predictable from their past state alone, we randomly shifted spikes within each trial (preserving the spike count) and recomputed decoding performance. In addition, we compared the standard Kalman filter decoder to other types of linear and non-linear decoders, including Wiener Filter, Wiener Cascade Filter, Extreme Gradient Boosting, Dense Feedforward Neural Network, Recursive Neural Network, Gated Recurrent Unit,

and Long Short Term Memory Network described in detail in Glaser et al., 2020. (Online supplementary figure 4).

2.4 Results

2.4.1 Complexity of the task and associated neuronal responses

First, we wished to characterize the complexity of the grasping behavior—to what extent did the animal produce different hand movements when grasping different objects? — and of the associated neuronal responses in sensorimotor cortex. The large and varied set of objects elicited a variety of hand conformations and neural responses in M1 and SC (Figure 2.2A). To characterize the complexity of the task, we first performed principal component analysis (PCA) on the hand kinematics and found that only 7–8 principal components explain most (95%) of its variance (Figure 2.2B). We then assessed whether the remaining components carry any information about the task. To that end, we projected kinematics on a subset of PCs, removing PCs in decreasing order, and inferred the object identity with projected kinematics. We found that even after subtracting the first eight PCs, we were still able to classify objects well above chance (Figure 2.2C)(c.f. Yan et al., 2020). Classifier performance was tightly linked to how different the kinematics were for different objects—more stereotyped grasps led to poorer classification performance as expected (Online supplementary figure 5). These results indicate that the monkeys produced a variety of hand configurations in an object-dependent way.

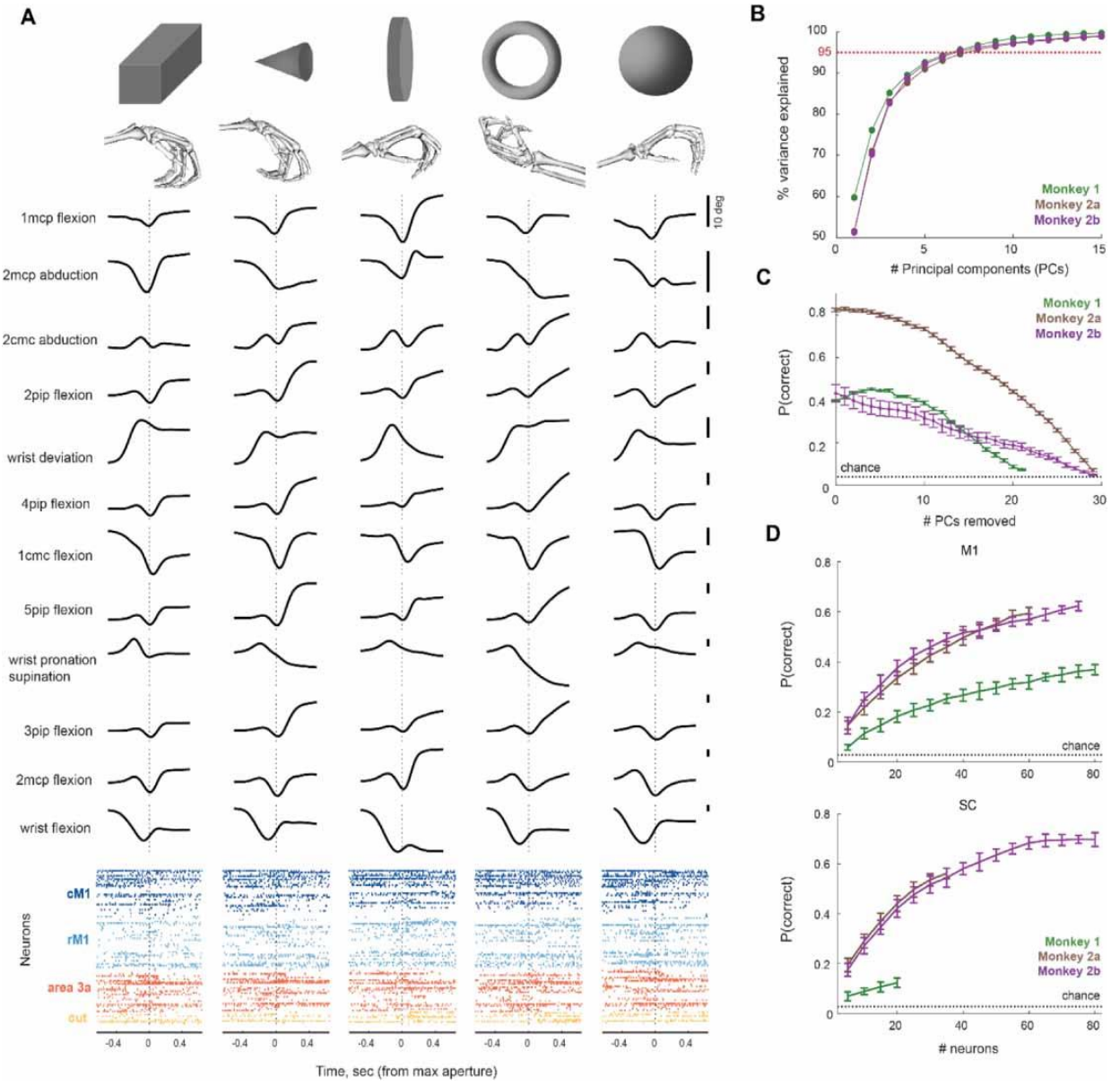

Figure 2.2 - Grasping objects of different shapes elicits varying kinematics and neural responses. (A) Example hand postures just before contact with corresponding mean kinematic trajectories of the 12 joints that move the most along with the evoked spiking activity of populations of neurons pooled from all sessions from caudal M1 (dark blue, N = 24), rostral M1 (light blue, N = 32), area 3a (orange, N = 25), and cutaneous neurons from areas 1 and 2 (yellow, N = 6) for 5 grasped objects (medium horizontal block, point, large outward disk, vertical ring and large sphere, see supplementary figure 1 for details). Trials were aligned to maximum aperture of the hand (t = 0). Hand nomenclature is described in supplementary figure 2. (B) Cumulative percentage of variance vs. number of principal cmponents of kinematics for the two monkeys. (C) Classification of objects based on kinematics projected on a decreasing number of principal components (the abscissa shows the number of removed components, ranked by variance) for all monkeys. Dotted horizontal line indicates probability of randomly selecting an object (1/35). Error bars denote the standard error of the mean classification performance across sessions. (D) Classification of objects based on neural signals (top—M1, bottom—SC) as a function of neuronal sample size. Error bars denote the standard error of the mean.

We then asked whether these object-dependent differences in kinematics were reflected in the neuronal responses. We found that in all monkeys as few as 5 neurons in a population were enough

to achieve above chance classification performance. Performance increased steadily with population size in both M1 and SC (Figure 2.2D).

2.4.2 Decoding single-trial kinematics from M1 and SC signals

Next, we assessed the degree to which the responses of neuronal populations in M1 and SC convey information about time-varying hand kinematics. We found that we could accurately decode single-trial kinematics of most joints in sessions for which we had enough simultaneously recorded neurons (average performance across joints: R^2= 0.52 for 44 M1 neurons in monkey 1, R^2 = 0.43 and 0.39 for 36 M1 and 37 SC neurons, respectively, in monkey 2b; Figure 2.3A, Online supplementary figure 3). Furthermore, M1 decoders significantly outperformed SC ones (Figure 2.3B).

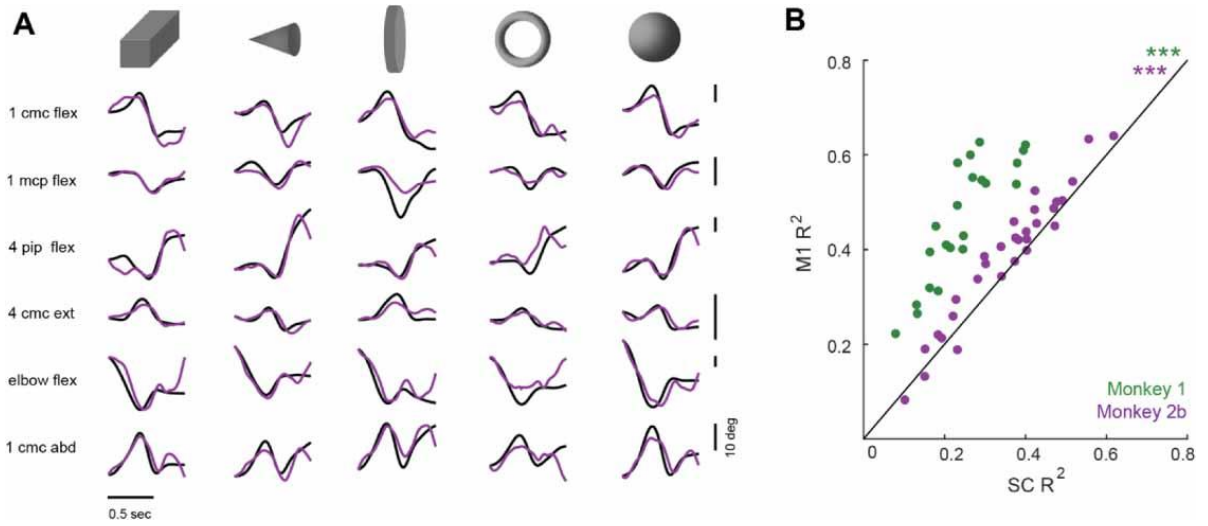

*Figure 2.3 - Decoding single-trial kinematics from M1 and SC signals. (A) Six joint angle trajectories produced during one grasp of each of five objects (black) along with the same trajectories decoded from the responses of 36 M1 neurons in monkey 2b (purple). Hand nomenclature is described in supplementary figure 2. (B) Performance of single-trial kinematics decoder for one session each from two monkeys with the same number of neurons in M1 and SC (N = 15 and 36 for monkeys 1 and 2b, respectively). Each dot corresponds to the mean decoding performance for one joint averaged over 5 cross-validation folds with randomly selected neurons from the recorded population. Stars indicate significance of Wilcoxon Signed Rank Test for matched samples: ***—alpha level of 0.001. Only sessions with a sufficient number of simultaneously recorded units were used in this analysis (monkeys 1 and 2b).*

To assess the degree to which performance was decoder dependent, we implemented 8 other linear and non-linear decoders (Online supplementary figure 4). We found that performance was very

similar across decoders and thus only report performance of the Kalman Filter in the main text given its simplicity and prevalence.

As expected, performance was slightly poorer if we constrained the decoder to be causal, as is required in online applications (Online supplementary figure 6A).

2.4.3 Decoding kinematics averaged across trials from M1 and SC signals

We recorded data over many sessions that individually did not yield enough neural signals to decode single-trial kinematics. To expand our data set, we pooled neural responses across all sessions from each monkey and used these pooled responses to decode the kinematics trajectory for each object, averaged across trials and sessions (see Methods). Importantly, we verified that, for sessions with sufficient sample size, decoding performance for single-trial and mean kinematics was comparable and yielded similar conclusions about the kinematics representations in M1 and SC (Online supplementary figure 6B). We then compared decoding performance of trial-averaged kinematics from M1 and SC using these neuronal responses pooled across sessions. For monkeys 1 and 2b, like their single-trial counterparts, trial-averaged decoders based on M1 responses tended to outperform those based on SC responses (Online supplementary figure 6C, Wilcoxon Signed Rank Test for matched samples: $Z = 4.0$ and 4.5 for monkeys 1 and 2b, respectively, $p < 0.0001$. However, for monkey 2a, the reverse was true ($Z = –4.4$, $p < 0.0001$). The difference between monkeys is likely due to the respective locations of SC recordings (area 3a vs. area 2; see online supplementary table 2 for sampling of cortical fields).

2.4.4 Comparing cortical areas

Next, we performed a more detailed analysis of how information about hand posture is distributed within M1 and SC (Figure 2.4). Given the small samples collected from each cortical field in a given session, we pooled data from each monkey across sessions and decoded trial-averaged

kinematics, having verified that this approach does not introduce systematic biases (Online supplementary figure 6B).

The caudal region of M1 contains more corticomotoneuronal (CM) cells—which make

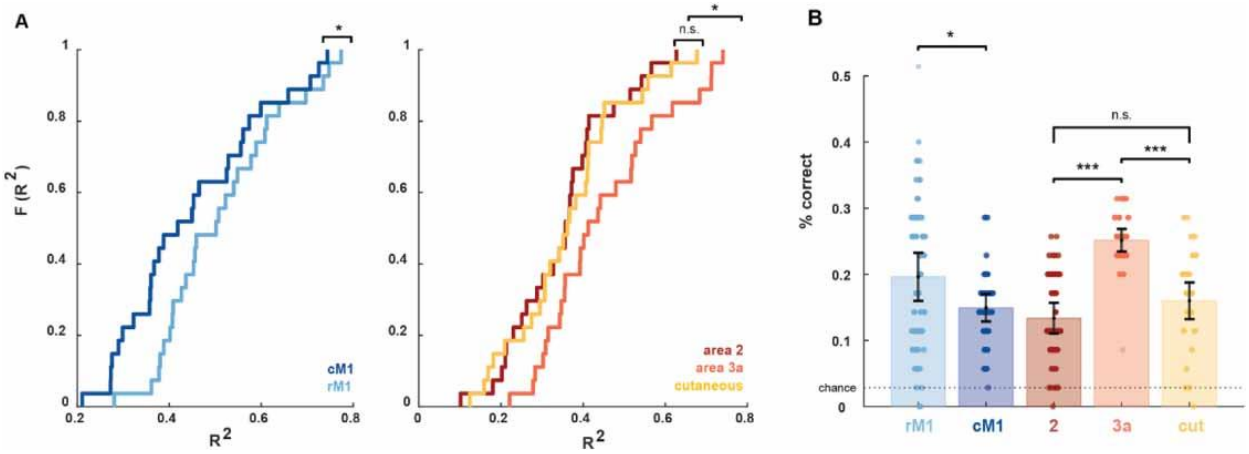

*Figure 2.4 - Comparison of cortical fields. (A) Left: cumulative distribution of the accuracy (R2) with which trial-averaged kinematics for all joint angles were decoded based on rM1 and cM1 responses. Right: Cumulative distributions of trial-averaged decoding accuracy for individual joint angles based on different cortical fields of SC. (B) Performance of an object classifier based on neuronal responses for monkey 2 (including both 2a and 2b) with each cortical area assessed separately. Each point indicates classification performance for one cross-validation fold. Stars in all plots indicate significance of a one-sided Mann-Whitney U test: n.s.—not significant, *—alpha level of 0.05 ***—alpha level of 0.001. Sessions from monkey 2 (a and b) were pooled together for this analysis. We discarded monkey 1 since we did not have sufficient number of units from all subfields shown here.*

monosynaptic connections with motoneurons—than does its rostral counterpart, and these CM neurons are thought to be critical for highly skilled movements, particularly of the hand (Rathelot & Strick, 2009). When comparing performance between areas (keeping the sample size equal), however, we found that decoding based on signals from rostral M1 systematically outperformed that from caudal M1 signals (one-sided Mann-Whitney U test: $Z = 1.83$, $p = 0.033$) (Figure 2.4A, left), thereby violating our expectations.

While neurons in Brodmann's area 3a exhibit almost exclusively proprioceptive responses, those in area 2 exhibit mixed proprioceptive and cutaneous responses (S. S. Kim et al., 2015). Cutaneous responses to skin stretch caused by joint movement may interfere with proprioceptive representations of the hand or contribute to them. We found that populations of neurons in area 3a yielded significantly better performance than did proprioceptive neurons in area 2 and neurons in

areas 1 and 2 that are classified as cutaneous during hand mapping (one-sided Mann-Whitney U test: area 3a vs area 2, Z = 2.3, p = 0.0107; area 3a vs cutaneous, Z = 1.95 p = 0.0253; area 2 vs cutaneous, Z = 0.329, p = 0.37) (Figure 2.4A, right).

We also assessed our ability to classify objects based on the responses evoked in different cortical populations and found results to be consistent with those of our kinematics decoding analysis: rM1 was more informative about object identity than was cM1 and area 3a was more informative about object identity than were areas 1 and 2 (Figure 2.4B).

2.4.5 Decoding joint groups

Next, we investigated whether the sampled subpopulations of M1 and SC preferentially encoded movements of different portions of the hand. Indeed, both M1 and SC are somatotopically organized (Hudson et al., 2017; Penfield & Boldrey, 1937; Pons et al., 1985; Wong et al., 1978; Woolsey et al., 1979), so incidental electrode placement might have led to better decoding for some hand regions than others. With this in mind, we divided the joints into 7 groups—distal, proximal, interphalangeal, metacarpophalangeal, carpometacarpal hand joints, wrist joints (pronation-supination, flexion, extension), and proximal arm joints (elbow)—and assessed the average decoding performance for each group (Figure 2.5A). With the exception of a few distal hand joints, all joint groups were decoded well, and decoding accuracy improved as the joint's range of motion increased ($r = 0.5$, $p = 5.3 \times 10^{-7}$ for M1 and $r = 0.46$, $p = 5.1 \times 10^{-6}$ for SC; Figure 2.5B). Significant positive correlations with motion variance were observed within metacarpophalangeal ($r = 0.79$, $p = 2.4 \times 10^{-7}$ for M1 and $r = 0.53$, $p = 0.0025$ for SC), carpometacarpal ($r = 0.63$, $p = 0.002$ for M1 and $r = 0.64$, $p = 0.002$ for SC) and wrist ($r = 0.74$, $p = 0.024$ for M1 and $r = 0.88$, $p = 0.0016$ for SC) joint groups, but not within distal ($r = 0.16$, $p = 0.62$ for M1 and $r = –0.07$, $p = 0.83$ for SC) or proximal ($r = 0.36$, $p = 0.25$ for M1 and $r = 0.15$, p

= 0.63 for SC) joints. These observations suggest that the arrays impinged upon neural populations that spanned the representation of the entire hand in both M1 and SC and that decoding performance was partially dependent on the range of joint motion.

2.4.6 Decoding kinematic synergies

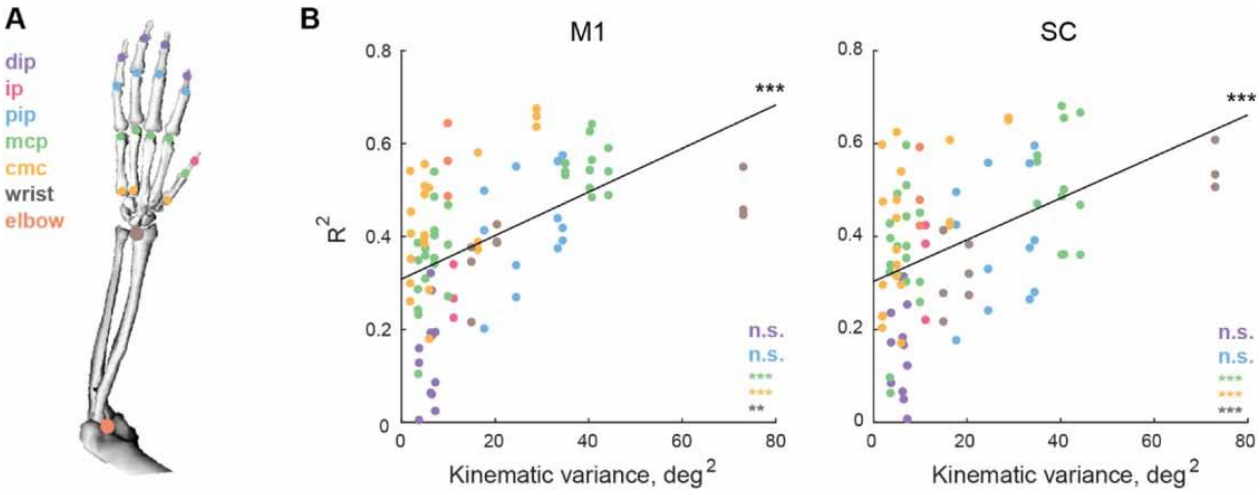

*Figure 2.5 - Decoding performance broken down by joint groups. (A) Location of joints color-coded by group: distal (dip, purple), proximal (pip, blue), interphalangeal (ip, pink), metacarpophalangeal (mcp, green), carpometacarpal (cmc, yellow), wrist (brown), elbow (orange). (B) Single joint decoding performance color-coded according to the scheme in A as a function of kinematic variance for all sessions of monkey 2b using M1 (N = 16 in each session) and SC (N = 19) populations. Each point denotes the mean over 5-fold cross-validation of each DoF. Black lines show best linear fit between kinematic variance and decoder performance of all DoFs. Stars indicate significance of correlation coefficient color-coded by joint group: ***—alpha level of 0.001, **—alpha level of 0.01, n.s.—not significant. Only sessions with a sufficient number of simultaneously recorded units in both areas were used in this analysis (monkey 2b). Monkey 1 was discarded due to incomplete set of recorded joints.*

Joint kinematics of the hand have been shown to exhibit systematic correlational structure, with some joints tending to move together. One possibility is that only patterns of highly correlated joint movements can be decoded from the neuronal activity in M1 and SC and that more subtle aspects of hand movements cannot. To this hypothesis, we performed a principal component analysis (PCA), projected kinematics onto a sequentially reduced sets of principal components (PCs), removing PCs in decreasing order of eigenvalue (i.e. higher-variance components first). We then decoded kinematics in this reduced space from neuronal signals in M1 and SC. Chance performance was computed by randomly permuting the spike times within each trial to distort the

temporal structure of the neuronal response, predictably yielding poor performance. We found that higher order (low-variance) components could still be decoded above chance (Figure 2.6), despite the fact that 95% of the variance in the kinematics can be explained with only 7–8 principal components (Figure 2.2B). Note that the trajectories projected onto higher order components of kinematics are still object dependent and thus under volitional control (Figure 2.2C) (Yan et al., 2020).

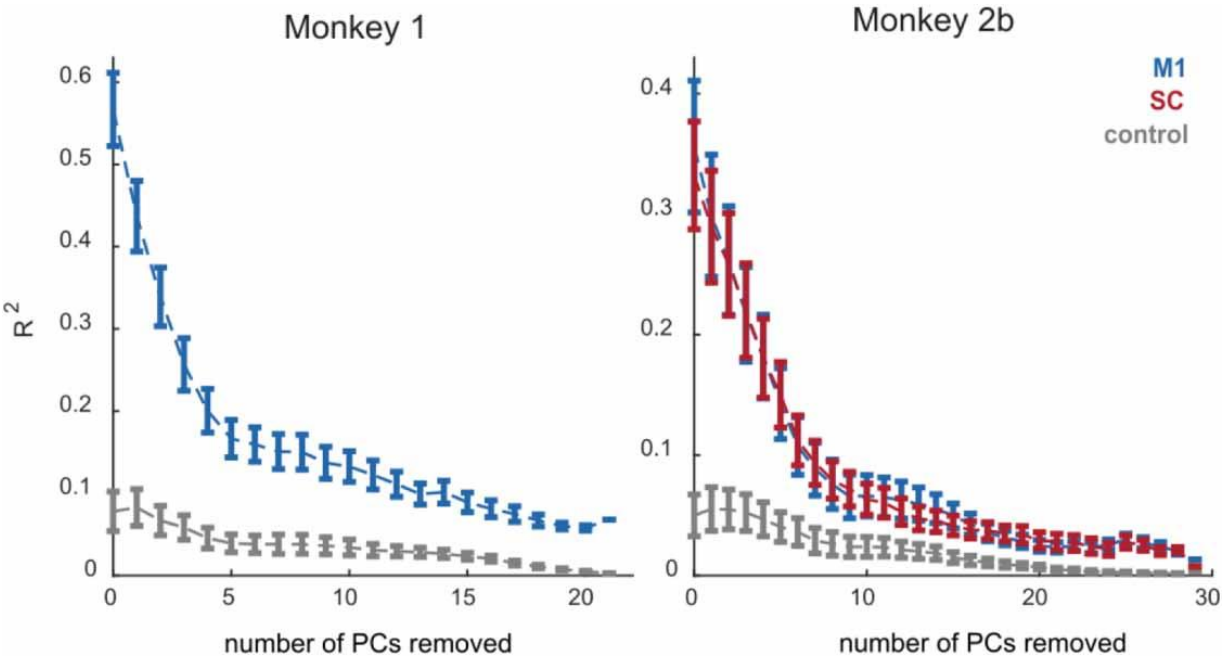

Figure 2.6 - Decoding synergistic movements. Average performance of decoding kinematics projected on decreasing number of principal components (x axis represents the number of removed components, ranked by variance) using populations of M1 (blue) and SC (red) neurons. Grey bars show decoding performance with randomly shifted spikes. Error bars denote the standard error of the mean. Only sessions with a sufficient number of simultaneously recorded units were used in this analysis (M1 and SC in monkey 1 and M1 only in monkey 2b).

2.4.7 Decoding postures vs. movements

In the above analyses, we showed that time-varying postures could be directly decoded from neuronal activity. This approach stands in contrast to that adopted for proximal limb kinematics or the application of proximal limb-related M1 activity to cursor control, which typically involve decoding joint or endpoint velocities from neuronal responses and then integrating these to obtain

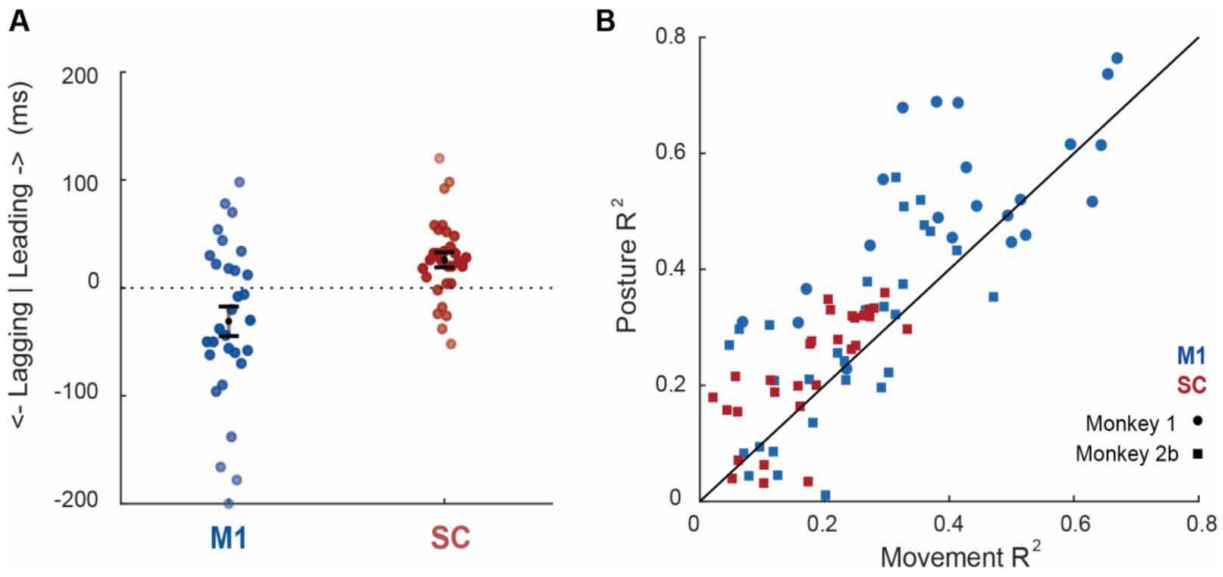

Figure 2.7 - Posture vs. movement decoding. (A) Optimal neural latencies for each joint of monkey 2b for M1 (blue) and SC (red). Error bars indicate mean and standard errors of the mean of latencies for each area. 'Leading' denotes more sensory-like neurons, where the kinematics lead the neuronal response. (B) Decoding performance of posture (y-axis) and movement (x-axis) decoding for a randomly selected population of 36 M1 (blue) or SC (red) neurons. Each marker indicates performance for one joint averaged over 5 folds. Different marker symbols denote different monkeys. Only sessions with a sufficient number of simultaneously recorded units were used in this analysis (M1 and SC in monkey 2b and M1 only in monkey 1).

postures (Chase et al., 2009; S.-P. Kim et al., 2011; Koyama et al., 2010; Taylor et al., 2002; Velliste et al., 2008). Indeed, even SC decoders for reaching movements appear to perform better when decoding limb velocity than limb posture (Weber et al., 2011). With this in mind, we assessed whether neuronal responses in M1 and SC preferentially encode postures or movements during grasp. To this end, we reconstructed joint angular velocities from sensorimotor responses and compared these to our reconstructions of angular positions. For this analysis, we used a single latency—determined to yield peak performance (for posture and movement separately within each area) (Figure 2.7A)—because multi-lag models allow for integration (from a velocity to a position signal) or differentiation (from a position to a velocity signal), thereby obscuring the distinction between postural and movement coding (Goodman et al., 2019). Using 20 units from each cortical subpopulation, we found that postures could be significantly better reconstructed than could movements (Figure 2.7B) (Wilcoxon Signed Rank Test for matched samples: Z = 2.91 and 2.01,

p = 0.004 and 0.044, for M1 in monkeys 1 and 2b, respectively; Z = 3.42, p = 0.0006 for SC in monkey 2b) in contrast to what has been observed for the proximal limb (S.-P. Kim et al., 2011; Wang et al., 2007; Weber et al., 2011).

2.5 Discussion

2.5.1 High dimensional decoding

Most decoding studies to date have focused on continuous movement of a few degrees of freedom, usually including shoulder and elbow (Ganguly & Carmena, 2009; Gilja et al., 2012; Lebedev et al., 2005; Mulliken et al., 2008; Suminski et al., 2010; Wessberg et al., 2000; Yu et al., 2007) and, less frequently, wrist (Hochberg et al., 2012b; Wodlinger et al., 2014) and finger joints (Aggarwal et al., 2013; Menz et al., 2015). Because of the complexity of the space of hand kinematics, most previous efforts to decode hand postures were either discrete, focusing on classification of a finite number of finger-wrist configurations (Branco et al., 2017; Carpaneto et al., 2011; Chestek et al., 2013; Schaffelhofer et al., 2015) or limited to a few common continuous finger movements, such as pinch, scoop, grip, and whole finger flexion/extension, and whole-hand aperture (Acharya et al., 2008; Bansal et al., 2012; Hochberg et al., 2012b; Wodlinger et al., 2014). As new hand tracking technologies are becoming available (Mathis et al., 2018; Pereira et al., 2019; Schaffelhofer & Scherberger, 2012), decoding tens of joints simultaneously is becoming increasingly manageable (Menz et al., 2015). Here, we show that up to 30 degrees of freedom can be decoded with a relatively small population of sensorimotor neurons even with a simple linear decoder.

2.5.2 Decoding from M1

Our approach is similar to that described in Menz et al. (2015), in which 27 degrees of freedom of grasping kinematics were reconstructed from the responses of neurons in posterior parietal cortex

and M1. Decoders built from the one area the two studies have in common, M1, yielded comparable performance (Online supplementary figure 3).

Anatomically, M1 can be divided into two regions: rostral and caudal M1. A large fraction of neurons in the caudal part of M1 make direct connections with motoneurons in the spinal cord and might be particularly relevant for dexterous hand control whereas neurons in the rostral region comprises a larger fraction of neurons that contact mainly spinal interneurons and only indirectly drive muscles (Rathelot & Strick, 2009). Counter to predictions derived from the anatomy, we found that decoders built with signals from rostral M1 actually outperformed decoders built with signals from caudal M1. Because grasp is so habitual and involves highly correlated patterns of joint movements, it may not constitute an 'expert' behavior and thus may not require a direct line to muscles. Had the animals been performing non-prehensile dexterous hand movements, we might have found an advantage of caudal M1 (Bortoff & Strick, 1993).

2.5.3 Decoding from SC

Previous attempts to decode kinematics from SC activity focused on proximal limb movements. Decoding reaching movements from combined M1 and SC activity yielded better performance than that achieved using M1 signals alone (Carmena et al., 2003; Lebedev et al., 2005). Decoding limb kinematics using electrocorticographic (ECoG) signals from SC achieved similar performance as with ECoG signals from M1 (Branco et al., 2017; Farrokhi & Erfanian, 2018).

In the present study, we decode, for the first time, hand kinematics from the spiking activity of neurons in Brodmann's areas 3a and 2 and find that both areas yield performance well above chance for all degrees of freedom. Area 3a showed performance comparable to M1, consistent with earlier observations that single-unit responses in areas 3a and 4 are tightly linked to time-varying hand postures (Goodman et al., 2019). Area 2, which lies downstream of area 3a but also receives

cutaneous input, yielded significantly worse performance than did M1, consistent with the hypothesis that the cutaneous input to this area obscures the proprioceptive representations, even before contact. While movement has been previously shown to activate cutaneous neurons in the absence of contact (S. S. Kim et al., 2015; Rincon-Gonzalez et al., 2011), our results suggest that cutaneous signals obscure rather than complement muscle- and tendon-derived signals about hand posture.

2.5.4 Posture and movement decoding

Neurons in motor cortex and proprioceptive areas of somatosensory cortex have been shown to preferentially encode velocity of the proximal limb (movement), rather than its position (posture) (Paninski et al., 2004; Wang et al., 2007). Consistent with this finding, decoders of velocities generally outperform those of joint positions both online (S.-P. Kim et al., 2008) and offline (Wang et al., 2007; Weber et al., 2011). However, this preferential encoding and decoding of movement over posture has been tested exclusively for the proximal limb. When we directly compared posture and movement decoding of the hand, we found that the former can be more faithfully decoded than can the latter. Importantly, for this analysis, we restricted the decoder to a single lag. Indeed, multi-lag decoders allow for linear integration of movement signals which converts these into postural signals. As might be expected, then, the difference in performance between posture and movement decoders is less pronounced for multi-lag models compared to their single-lag counterparts (Online supplementary figure 7) and multi-lag decoders sometimes lead to an advantage for postural decoding even in the proximal limb (Carmena et al., 2003). Postural preference in our analysis implies a difference between proximal and distal limb representations, which may be inherited from the different inertial and biomechanical properties of the arm and the hand and is well suited to support stereognosis (Goodman et al., 2019).

2.5.5 Decoding methods

The application of machine learning to kinematic/cursor decoding is becoming standard practice (Glaser et al., 2020). However, the extent to which recently developed decoding approaches robustly improve performance of high dimensional decoders (of hand kinematics, e.g.) has not been systematically investigated. Here, we applied a variety of linear and non-linear approaches to decoding hand movements (described in detail in (Glaser et al., 2020)) and found that performance improved with some, but not all non-linear methods, with the best performance increase achieved by Support Vector Regression, Dense Neural Network, and LSTM (Online supplementary figure 4). However, the improvement is typically minimal, confined mostly to well-decoded DoFs, and may not justify the added computational complexity and potential for overfitting. Note, however, that an algorithm that performs better offline does not necessarily perform better online (Chase et al., 2009; Koyama et al., 2010).

2.5.6 Closed-loop robotic limb control

A major application of kinematic decoders is to drive brain machine interfaces aimed at restoring movement in patients with sensorimotor impairments (Bensmaia & Miller, 2014). Indeed, intended movements can be inferred from neural signals in sensorimotor cortex and converted into control commands to an external device, such as a robotic limb. While remarkable control has been previously achieved for a robotic arm and hand, with up to 10 degrees of freedom under independent control (Wodlinger et al., 2014), the control of the hand itself remains relatively primitive, restricted to few of its many potential degrees of freedom. Here, we show that information about up to 30 degrees of freedom can be simultaneously reconstructed using a fast and simple approach with a relatively small number of neurons. Note, however, that the decoding reported here was performed offline and the implications of the present results for online decoding

need to be tested (Chase et al., 2009; Kao et al., 2014; Koyama et al., 2010; Nicolas-Alonso & Gomez-Gil, 2012; Weber et al., 2011).

The dexterity of robotic hands is severely limited by the absence of sensory feedback about hand posture. One approach to convey proprioceptive feedback would be to stimulate proprioceptive neurons in SC (Armenta Salas et al., 2018; London et al., 2008; Tomlinson & Miller, 2016). Our results suggest that SC—particularly area 3 a—carries a faithful representation of hand posture, one that could in principle be exploited to convey intuitive sensory feedback about limb state. However, the success of tactile feedback through intracortical microstimulation (ICMS) has hinged on the somatotopic organization of cutaneous representations in SC. While proprioceptive representations exhibit some somatotopic organization (Costanzo & Gardner, 1981; Iwamura et al., 1983, 1993; Krubitzer et al., 2004), that organization is generally coarser than that seen in tactile representations in cortex and may depend on whether movements are actively generated or imposed on the limb (Goodman et al., 2019; Soso & Fetz, 1980). Thus, whether the proprioceptive representation exhibits a spatial topography that can be exploited to convey artificial proprioceptive feedback remains to be established.

2.5 Supplementary materials

Supplementary materials (Figures and Tables) for this chapter are published online.

2.7 References

Acharya, S., Tenore, F., Aggarwal, V., Etienne-Cummings, R., Schieber, M. H., & Thakor, N. V. (2008). Decoding Individuated Finger Movements Using Volume-Constrained Neuronal Ensembles in the M1 Hand Area. *IEEE Transactions on Neural Systems and Rehabilitation Engineering*, *16*(1), 15–23. https://doi.org/10.1109/TNSRE.2007.916269

Aggarwal, V., Mollazadeh, M., Davidson, A. G., Schieber, M. H., & Thakor, N. V. (2013). State-based decoding of hand and finger kinematics using neuronal ensemble and LFP activity during dexterous reach-to-grasp movements. *Journal of Neurophysiology*, *109*(12), 3067–3081. https://doi.org/10.1152/jn.01038.2011

Anderson, K. D. (2004). Targeting Recovery: Priorities of the Spinal Cord-Injured Population. *Journal of Neurotrauma*, *21*(10), 1371–1383. https://doi.org/10.1089/neu.2004.21.1371

Armenta Salas, M., Bashford, L., Kellis, S., Jafari, M., Jo, H., Kramer, D., Shanfield, K., Pejsa, K., Lee, B., Liu, C. Y., & Andersen, R. A. (2018). Proprioceptive and cutaneous sensations in humans elicited by intracortical microstimulation. *ELife*, *7*, e32904. https://doi.org/10.7554/eLife.32904

Bansal, A. K., Truccolo, W., Vargas-Irwin, C. E., & Donoghue, J. P. (2012). Decoding 3D reach and grasp from hybrid signals in motor and premotor cortices: Spikes, multiunit activity, and local field potentials. *Journal of Neurophysiology*, *107*(5), 1337–1355. https://doi.org/10.1152/jn.00781.2011

Belić, J. J., & Faisal, A. A. (2015). Decoding of human hand actions to handle missing limbs in neuroprosthetics. *Frontiers in Computational Neuroscience*, *9*. https://www.frontiersin.org/articles/10.3389/fncom.2015.00027

Bensmaia, S. J. (2015). Biological and bionic hands: Natural neural coding and artificial perception. *Philosophical Transactions of the Royal Society B: Biological Sciences*, *370*(1677), 20140209. https://doi.org/10.1098/rstb.2014.0209

Bensmaia, S. J., & Miller, L. E. (2014). Restoring sensorimotor function through intracortical interfaces: Progress and looming challenges. *Nature Reviews Neuroscience*, *15*(5), Article 5. https://doi.org/10.1038/nrn3724

Bortoff, G. A., & Strick, P. L. (1993). Corticospinal terminations in two new-world primates: Further evidence that corticomotoneuronal connections provide part of the neural substrate for manual dexterity. *Journal of Neuroscience*, *13*(12), 5105–5118. https://doi.org/10.1523/JNEUROSCI.13-12-05105.1993

Branco, M. P., Freudenburg, Z. V., Aarnoutse, E. J., Bleichner, M. G., Vansteensel, M. J., & Ramsey, N. F. (2017). Decoding hand gestures from primary somatosensory cortex using high-density ECoG. *NeuroImage*, *147*, 130–142. https://doi.org/10.1016/j.neuroimage.2016.12.004

Carmena, J. M., Lebedev, M. A., Crist, R. E., O'Doherty, J. E., Santucci, D. M., Dimitrov, D. F., Patil, P. G., Henriquez, C. S., & Nicolelis, M. A. L. (2003). Learning to Control a Brain–Machine Interface for Reaching and Grasping by Primates. *PLOS Biology*, *1*(2), e42. https://doi.org/10.1371/journal.pbio.0000042

Carpaneto, J., Umiltà, M. A., Fogassi, L., Murata, A., Gallese, V., Micera, S., & Raos, V. (2011). Decoding the activity of grasping neurons recorded from the ventral premotor area F5 of the macaque monkey. *Neuroscience*, *188*, 80–94. https://doi.org/10.1016/j.neuroscience.2011.04.062

Chase, S. M., Schwartz, A. B., & Kass, R. E. (2009). Bias, optimal linear estimation, and the differences between open-loop simulation and closed-loop performance of spiking-based brain–computer interface algorithms. *Neural Networks*, *22*(9), 1203–1213. https://doi.org/10.1016/j.neunet.2009.05.005

Chestek, C. A., Gilja, V., Blabe, C. H., Foster, B. L., Shenoy, K. V., Parvizi, J., & Henderson, J. M. (2013). Hand posture classification using electrocorticography signals in the gamma band over human sensorimotor brain areas. *Journal of Neural Engineering*, *10*(2), 026002. https://doi.org/10.1088/1741-2560/10/2/026002

Cole, J. D., & Sedgwick, E. M. (1992). The perceptions of force and of movement in a man without large myelinated sensory afferents below the neck. *The Journal of Physiology*, *449*(1), 503–515. https://doi.org/10.1113/jphysiol.1992.sp019099

Costanzo, R. M., & Gardner, E. P. (1981). Multiple-joint neurons in somatosensory cortex of awake monkeys. *Brain Research*, *214*(2), 321–333. https://doi.org/10.1016/0006-8993(81)91197-5

Delp, S. L., Anderson, F. C., Arnold, A. S., Loan, P., Habib, A., John, C. T., Guendelman, E., & Thelen, D. G. (2007). OpenSim: Open-source software to create and analyze dynamic simulations of movement. *IEEE Transactions on Bio-Medical Engineering*, *54*(11), 1940–1950. https://doi.org/10.1109/TBME.2007.901024

Dotson, N. M., Hoffman, S. J., Goodell, B., & Gray, C. M. (2017). A Large-Scale Semi-Chronic Microdrive Recording System for Non-Human Primates. *Neuron*, *96*(4), 769-782.e2. https://doi.org/10.1016/j.neuron.2017.09.050

Dyer, E. L., Gheshlaghi Azar, M., Perich, M. G., Fernandes, H. L., Naufel, S., Miller, L. E., & Körding, K. P. (2017). A cryptography-based approach for movement decoding. *Nature Biomedical Engineering*, *1*(12), Article 12. https://doi.org/10.1038/s41551-017-0169-7

Faragher, R. (2012). Understanding the Basis of the Kalman Filter Via a Simple and Intuitive Derivation [Lecture Notes]. *IEEE Signal Processing Magazine*, *29*(5), 128–132. https://doi.org/10.1109/MSP.2012.2203621

Farrokhi, B., & Erfanian, A. (2018). A piecewise probabilistic regression model to decode hand movement trajectories from epidural and subdural ECoG signals. *Journal of Neural Engineering*, *15*(3), 036020. https://doi.org/10.1088/1741-2552/aab290

Flesher, S. N., Collinger, J. L., Foldes, S. T., Weiss, J. M., Downey, J. E., Tyler-Kabara, E. C., Bensmaia, S. J., Schwartz, A. B., Boninger, M. L., & Gaunt, R. A. (2016). Intracortical microstimulation of human somatosensory cortex. *Science Translational Medicine*, *8*(361), 361ra141-361ra141. https://doi.org/10.1126/scitranslmed.aaf8083

Fromm, C., & Evarts, E. V. (1982). Pyramidal tract neurons in somatosensory cortex: Central and peripheral inputs during voluntary movement. *Brain Research*, *238*(1), 186–191. https://doi.org/10.1016/0006-8993(82)90781-8

Ganguly, K., & Carmena, J. M. (2009). Emergence of a Stable Cortical Map for Neuroprosthetic Control. *PLoS Biology*, *7*(7), e1000153. https://doi.org/10.1371/journal.pbio.1000153

Gardner, E. P., & Costanzo, R. M. (1981). Properties of kinesthetic neurons in somatosensory cortex of awake monkeys. *Brain Research*, *214*(2), 301–319. https://doi.org/10.1016/0006-8993(81)91196-3

Ghez, C., & Sainburg, R. (1995). Proprioceptive control of interjoint coordination. *Canadian Journal of Physiology and Pharmacology*, *73*(2), 273–284. https://doi.org/10.1139/y95-038

Gilja, V., Nuyujukian, P., Chestek, C. A., Cunningham, J. P., Yu, B. M., Fan, J. M., Churchland, M. M., Kaufman, M. T., Kao, J. C., Ryu, S. I., & Shenoy, K. V. (2012). A high-performance neural prosthesis enabled by control algorithm design. *Nature Neuroscience*, *15*(12), Article 12. https://doi.org/10.1038/nn.3265

Glaser, J. I., Benjamin, A. S., Chowdhury, R. H., Perich, M. G., Miller, L. E., & Kording, K. P. (2020). *Machine learning for neural decoding* (arXiv:1708.00909). arXiv. https://doi.org/10.48550/arXiv.1708.00909

Goodman, J. M., Tabot, G. A., Lee, A. S., Suresh, A. K., Rajan, A. T., Hatsopoulos, N. G., & Bensmaia, S. (2019). Postural Representations of the Hand in the Primate Sensorimotor Cortex. *Neuron*, *104*(5), 1000-1009.e7. https://doi.org/10.1016/j.neuron.2019.09.004

Gray, C. M., Goodell, B., & Lear, A. (2007). Multichannel Micromanipulator and Chamber System for Recording Multineuronal Activity in Alert, Non-Human Primates. *Journal of Neurophysiology*, *98*(1), 527–536. https://doi.org/10.1152/jn.00259.2007

Hochberg, L. R., Bacher, D., Jarosiewicz, B., Masse, N. Y., Simeral, J. D., Vogel, J., Haddadin, S., Liu, J., Cash, S. S., van der Smagt, P., & Donoghue, J. P. (2012). Reach and grasp by people with tetraplegia using a neurally controlled robotic arm. *Nature*, *485*(7398), Article 7398. https://doi.org/10.1038/nature11076

Hudson, H. M., Park, M. C., Belhaj-Saïf, A., & Cheney, P. D. (2017). Representation of individual forelimb muscles in primary motor cortex. *Journal of Neurophysiology*, *118*(1), 47–63. https://doi.org/10.1152/jn.01070.2015

Ingram, J. N., Körding, K. P., Howard, I. S., & Wolpert, D. M. (2008). The statistics of natural hand movements. *Experimental Brain Research*, *188*(2), 223–236. https://doi.org/10.1007/s00221-008-1355-3

Iwamura, Y., Tanaka, M., Sakamoto, M., & Hikosaka, O. (1983). Functional subdivisions representing different finger regions in area 3 of the first somatosensory cortex of the conscious monkey. *Experimental Brain Research*, *51*(3), 315–326. https://doi.org/10.1007/BF00237868

Iwamura, Y., Tanaka, M., Sakamoto, M., & Hikosaka, O. (1993). Rostrocaudal gradients in the neuronal receptive field complexity in the finger region of the alert monkey's postcentral gyrus. *Experimental Brain Research*, *92*(3), 360–368. https://doi.org/10.1007/BF00229023

Kao, J. C., Stavisky, S. D., Sussillo, D., Nuyujukian, P., & Shenoy, K. V. (2014). Information Systems Opportunities in Brain–Machine Interface Decoders. *Proceedings of the IEEE*, *102*(5), 666–682. https://doi.org/10.1109/JPROC.2014.2307357

Kim, S. S., Gomez-Ramirez, M., Thakur, P. H., & Hsiao, S. S. (2015). Multimodal Interactions between Proprioceptive and Cutaneous Signals in Primary Somatosensory Cortex. *Neuron*, *86*(2), 555–566. https://doi.org/10.1016/j.neuron.2015.03.020

Kim, S.-P., Simeral, J. D., Hochberg, L. R., Donoghue, J. P., & Black, M. J. (2008). Neural control of computer cursor velocity by decoding motor cortical spiking activity in humans with tetraplegia*. *Journal of Neural Engineering*, *5*(4), 455. https://doi.org/10.1088/1741-2560/5/4/010

Kim, S.-P., Simeral, J. D., Hochberg, L. R., Donoghue, J. P., Friehs, G. M., & Black, M. J. (2011). Point-and-Click Cursor Control With an Intracortical Neural Interface System by Humans With Tetraplegia. *IEEE Transactions on Neural Systems and Rehabilitation Engineering*, *19*(2), 193–203. https://doi.org/10.1109/TNSRE.2011.2107750

Koyama, S., Chase, S. M., Whitford, A. S., Velliste, M., Schwartz, A. B., & Kass, R. E. (2010). Comparison of brain–computer interface decoding algorithms in open-loop and closed-loop control. *Journal of Computational Neuroscience*, *29*(1), 73–87. https://doi.org/10.1007/s10827-009-0196-9

Krubitzer, L., Huffman, K. J., Disbrow, E., & Recanzone, G. (2004). Organization of area 3a in macaque monkeys: Contributions to the cortical phenotype. *Journal of Comparative Neurology*, *471*(1), 97–111. https://doi.org/10.1002/cne.20025

Lebedev, M. A., Carmena, J. M., O'Doherty, J. E., Zacksenhouse, M., Henriquez, C. S., Principe, J. C., & Nicolelis, M. A. L. (2005). Cortical Ensemble Adaptation to Represent Velocity of an Artificial Actuator Controlled by a Brain-Machine Interface. *Journal of Neuroscience*, *25*(19), 4681–4693. https://doi.org/10.1523/JNEUROSCI.4088-04.2005

London, B. M., Jordan, L. R., Jackson, C. R., & Miller, L. E. (2008). Electrical Stimulation of the Proprioceptive Cortex (Area 3a) Used to Instruct a Behaving Monkey. *IEEE Transactions on Neural Systems and Rehabilitation Engineering*, *16*(1), 32–36. https://doi.org/10.1109/TNSRE.2007.907544

London, B. M., & Miller, L. E. (2013). Responses of somatosensory area 2 neurons to actively and passively generated limb movements. *Journal of Neurophysiology*, *109*(6), 1505–1513. https://doi.org/10.1152/jn.00372.2012

Mathis, A., Mamidanna, P., Cury, K. M., Abe, T., Murthy, V. N., Mathis, M. W., & Bethge, M. (2018). DeepLabCut: Markerless pose estimation of user-defined body parts with deep learning. *Nature Neuroscience*, *21*(9), 1281–1289. https://doi.org/10.1038/s41593-018-0209-y

Menz, V. K., Schaffelhofer, S., & Scherberger, H. (2015). Representation of continuous hand and arm movements in macaque areas M1, F5, and AIP: A comparative decoding study. *Journal of Neural Engineering*, *12*(5), 056016. https://doi.org/10.1088/1741-2560/12/5/056016

Mulliken, G. H., Musallam, S., & Andersen, R. A. (2008). Decoding Trajectories from Posterior Parietal Cortex Ensembles. *Journal of Neuroscience*, *28*(48), 12913–12926. https://doi.org/10.1523/JNEUROSCI.1463-08.2008

Nicolas-Alonso, L. F., & Gomez-Gil, J. (2012). Brain Computer Interfaces, a Review. *Sensors*, *12*(2), Article 2. https://doi.org/10.3390/s120201211

Okorokova, E., Lebedev, M., Linderman, M., & Ossadtchi, A. (2015). A dynamical model improves reconstruction of handwriting from multichannel electromyographic recordings. *Frontiers in Neuroscience*, *9*. https://www.frontiersin.org/articles/10.3389/fnins.2015.00389

Paninski, L., Fellows, M. R., Hatsopoulos, N. G., & Donoghue, J. P. (2004). Spatiotemporal Tuning of Motor Cortical Neurons for Hand Position and Velocity. *Journal of Neurophysiology*, *91*(1), 515–532. https://doi.org/10.1152/jn.00587.2002

Penfield, W., & Boldrey, E. (1937). Somatic motor and sensory representation in the cerebral cortex of man as studied by electrical stimulation. *Brain*, *60*(4), 389–443. https://doi.org/10.1093/brain/60.4.389

Pereira, T. D., Aldarondo, D. E., Willmore, L., Kislin, M., Wang, S. S.-H., Murthy, M., & Shaevitz, J. W. (2019). Fast animal pose estimation using deep neural networks. *Nature Methods*, *16*(1), Article 1. https://doi.org/10.1038/s41592-018-0234-5

Pons, T. P., Garraghty, P. E., Cusick, C. G., & Kaas, J. H. (1985). The somatotopic organization of area 2 in macaque monkeys. *Journal of Comparative Neurology*, *241*(4), 445–466. https://doi.org/10.1002/cne.902410405

Pons, T. P., & Kaas, J. H. (1986). Corticocortical connections of area 2 of somatosensory cortex in macaque monkeys: A correlative anatomical and electrophysiological study. *The Journal of Comparative Neurology*, *248*(3), 313–335. https://doi.org/10.1002/cne.902480303

Prud'homme, M. J., & Kalaska, J. F. (1994). Proprioceptive activity in primate primary somatosensory cortex during active arm reaching movements. *Journal of Neurophysiology*, *72*(5), 2280–2301. https://doi.org/10.1152/jn.1994.72.5.2280

Rathelot, J.-A., & Strick, P. L. (2009). Subdivisions of primary motor cortex based on cortico-motoneuronal cells. *Proceedings of the National Academy of Sciences*, *106*(3), 918–923. https://doi.org/10.1073/pnas.0808362106

Rincon-Gonzalez, L., Warren, J. P., Meller, D. M., & Helms Tillery, S. (2011). Haptic Interaction of Touch and Proprioception: Implications for Neuroprosthetics. *IEEE Transactions on Neural Systems and Rehabilitation Engineering*, *19*(5), 490–500. https://doi.org/10.1109/TNSRE.2011.2166808

Sainburg, R. L., Ghilardi, M. F., Poizner, H., & Ghez, C. (1995). Control of limb dynamics in normal subjects and patients without proprioception. *Journal of Neurophysiology*, *73*(2), 820–835. https://doi.org/10.1152/jn.1995.73.2.820

Schaffelhofer, S., Agudelo-Toro, A., & Scherberger, H. (2015). Decoding a Wide Range of Hand Configurations from Macaque Motor, Premotor, and Parietal Cortices. *Journal of Neuroscience*, *35*(3), 1068–1081. https://doi.org/10.1523/JNEUROSCI.3594-14.2015

Schaffelhofer, S., & Scherberger, H. (2012). A new method of accurate hand- and arm-tracking for small primates. *Journal of Neural Engineering*, *9*(2), 026025. https://doi.org/10.1088/1741-2560/9/2/026025

Scott, S. H. (2004). Optimal feedback control and the neural basis of volitional motor control. *Nature Reviews Neuroscience*, *5*(7), Article 7. https://doi.org/10.1038/nrn1427

Soechting, J. F., & Flanders, M. (1989). Errors in pointing are due to approximations in sensorimotor transformations. *Journal of Neurophysiology*, *62*(2), 595–608. https://doi.org/10.1152/jn.1989.62.2.595

Soso, M. J., & Fetz, E. E. (1980). Responses of identified cells in postcentral cortex of awake monkeys during comparable active and passive joint movements. *Journal of Neurophysiology*, *43*(4), 1090–1110. https://doi.org/10.1152/jn.1980.43.4.1090

Suminski, A. J., Tkach, D. C., Fagg, A. H., & Hatsopoulos, N. G. (2010). Incorporating Feedback from Multiple Sensory Modalities Enhances Brain–Machine Interface Control. *The Journal of Neuroscience*, *30*(50), 16777. https://doi.org/10.1523/JNEUROSCI.3967-10.2010

Taylor, D. M., Tillery, S. I. H., & Schwartz, A. B. (2002). Direct Cortical Control of 3D Neuroprosthetic Devices. *Science*, *296*(5574), 1829–1832. https://doi.org/10.1126/science.1070291

Tomlinson, T., & Miller, L. E. (2016). Toward a Proprioceptive Neural Interface that Mimics Natural Cortical Activity. *Advances in Experimental Medicine and Biology*, *957*, 367–388. https://doi.org/10.1007/978-3-319-47313-0_20

Velliste, M., Perel, S., Spalding, M. C., Whitford, A. S., & Schwartz, A. B. (2008). Cortical control of a prosthetic arm for self-feeding. *Nature*, *453*(7198), Article 7198. https://doi.org/10.1038/nature06996

Wang, W., Chan, S. S., Heldman, D. A., & Moran, D. W. (2007). Motor Cortical Representation of Position and Velocity During Reaching. *Journal of Neurophysiology*, *97*(6), 4258–4270. https://doi.org/10.1152/jn.01180.2006

Weber, D. J., London, B. M., Hokanson, J. A., Ayers, C. A., Gaunt, R. A., Torres, R. R., Zaaimi, B., & Miller, L. E. (2011). Limb-State Information Encoded by Peripheral and Central Somatosensory Neurons: Implications for an Afferent Interface. *IEEE Transactions on Neural Systems and Rehabilitation Engineering*, *19*(5), 501–513. https://doi.org/10.1109/TNSRE.2011.2163145

Wessberg, J., Stambaugh, C. R., Kralik, J. D., Beck, P. D., Laubach, M., Chapin, J. K., Kim, J., Biggs, S. J., Srinivasan, M. A., & Nicolelis, M. A. L. (2000). Real-time prediction of hand trajectory by ensembles of cortical neurons in primates. *Nature*, *408*(6810), Article 6810. https://doi.org/10.1038/35042582

Wodlinger, B., Downey, J. E., Tyler-Kabara, E. C., Schwartz, A. B., Boninger, M. L., & Collinger, J. L. (2014). Ten-dimensional anthropomorphic arm control in a human brain−machine interface: Difficulties, solutions, and limitations. *Journal of Neural Engineering*, *12*(1), 016011. https://doi.org/10.1088/1741-2560/12/1/016011

Wong, Y. C., Kwan, H. C., MacKay, W. A., & Murphy, J. T. (1978). Spatial organization of precentral cortex in awake primates. I. Somatosensory inputs. *Journal of Neurophysiology*, *41*(5), 1107–1119. https://doi.org/10.1152/jn.1978.41.5.1107

Woolsey, C. N., Erickson, T. C., & Gilson, W. E. (1979). Localization in somatic sensory and motor areas of human cerebral cortex as determined by direct recording of evoked potentials and electrical stimulation. *Journal of Neurosurgery*, *51*(4), 476–506. https://doi.org/10.3171/jns.1979.51.4.0476

Yan, Y., Goodman, J. M., Moore, D. D., Solla, S. A., & Bensmaia, S. J. (2020). Unexpected complexity of everyday manual behaviors. *Nature Communications*, *11*(1), Article 1. https://doi.org/10.1038/s41467-020-17404-0

Yu, B. M., Kemere, C., Santhanam, G., Afshar, A., Ryu, S. I., Meng, T. H., Sahani, M., & Shenoy, K. V. (2007). Mixture of Trajectory Models for Neural Decoding of Goal-Directed Movements. *Journal of Neurophysiology*, *97*(5), 3763–3780. https://doi.org/10.1152/jn.00482.2006

Chapter 3 | Neural population dynamics in motor cortex are different for reach and grasp[3]

3.1 Abstract

Low-dimensional linear dynamics are observed in neuronal population activity in primary motor cortex (M1) when monkeys make reaching movements. This population-level behavior is consistent with a role for M1 as an autonomous pattern generator that drives muscles to give rise to movement. In the present study, we examine whether similar dynamics are also observed during grasping movements, which involve fundamentally different patterns of kinematics and muscle activations. Using a variety of analytical approaches, we show that M1 does not exhibit such dynamics during grasping movements. Rather, the grasp-related neuronal dynamics in M1 are similar to their counterparts in somatosensory cortex, whose activity is driven primarily by afferent inputs rather than by intrinsic dynamics. The basic structure of the neuronal activity underlying hand control is thus fundamentally different from that underlying arm control.

3.2 Introduction

The responses of populations of neurons in primary motor cortex (M1) exhibit rotational dynamics – reflecting a neural oscillation at the population level – when animals make arm movements, including reaching and cycling (Churchland et al., 2012; Lara et al., 2018; Russo et al., 2018; Shenoy et al., 2013). One interpretation of this population-level behavior is that M1 acts as a pattern generator that drives muscles to give rise to movement. A major question is whether such

[3] This chapter was published: Suresh, A. K., Goodman, J. M., Okorokova, E. V., Kaufman, M., Hatsopoulos, N. G., & Bensmaia, S. J. (2020). Neural population dynamics in motor cortex are different for reach and grasp. ELife, 9, e58848. https://doi.org/10.7554/eLife.58848 Supplementary materials are available online.

population dynamics reflect a general principle of M1 function, or whether they underlie some behaviors and effectors but not others. To address this question, we examined the dynamics in the neuronal population activity during grasping movements, which involve a plant (the hand) that serves a different function, comprises more joints, and is characterized by different mechanical properties (Rathelot & Strick, 2009). While the hand is endowed with many degrees of freedom, hand kinematics can be largely accounted for within a small subspace (Ingram et al., 2008; Overduin et al., 2015; Santello et al., 1998; Tresch & Jarc, 2009) so we might expect to observe low-dimensional neural dynamics during hand movements, not unlike those observed during arm movements.

To test this, we recorded the neural activity in M1 using chronically implanted electrode arrays as monkeys performed a grasping task, restricting our analyses to responses before object contact (Online materials Figure 1—figure supplement 1). Animals were required to hold their arms still at the elbow and shoulder joints as a robotic arm presented each object to their contralateral hand. This task – which can be likened to catching a tossed object or grasping an offered one – limits proximal limb movements and isolates grasping movements. For comparison, we also examined the responses of M1 neurons during a center-out reaching task (Hatsopoulos et al., 2007). In addition, we compared grasping responses in M1 to their counterparts in somatosensory cortex (SCx), which is primarily driven by afferent input and therefore should not exhibit autonomous dynamics (Russo et al., 2018).

3.3 Results

First, we used jPCA to search for rotational dynamics in a low-dimensional manifold of M1 population activity (Figure 3.1; Churchland et al., 2012). Replicating previous findings, reaching was associated with a variety of different activity patterns at the single-neuron level (Figure 3.1A)

that were collectively governed by rotational dynamics at the population level (Figure 3.1C,E). During grasp, individual M1 neurons similarly exhibited a variety of different response profiles (Figure 3.1B), but rotational dynamics were weak or absent at the population level (Figure 3.1D,E).

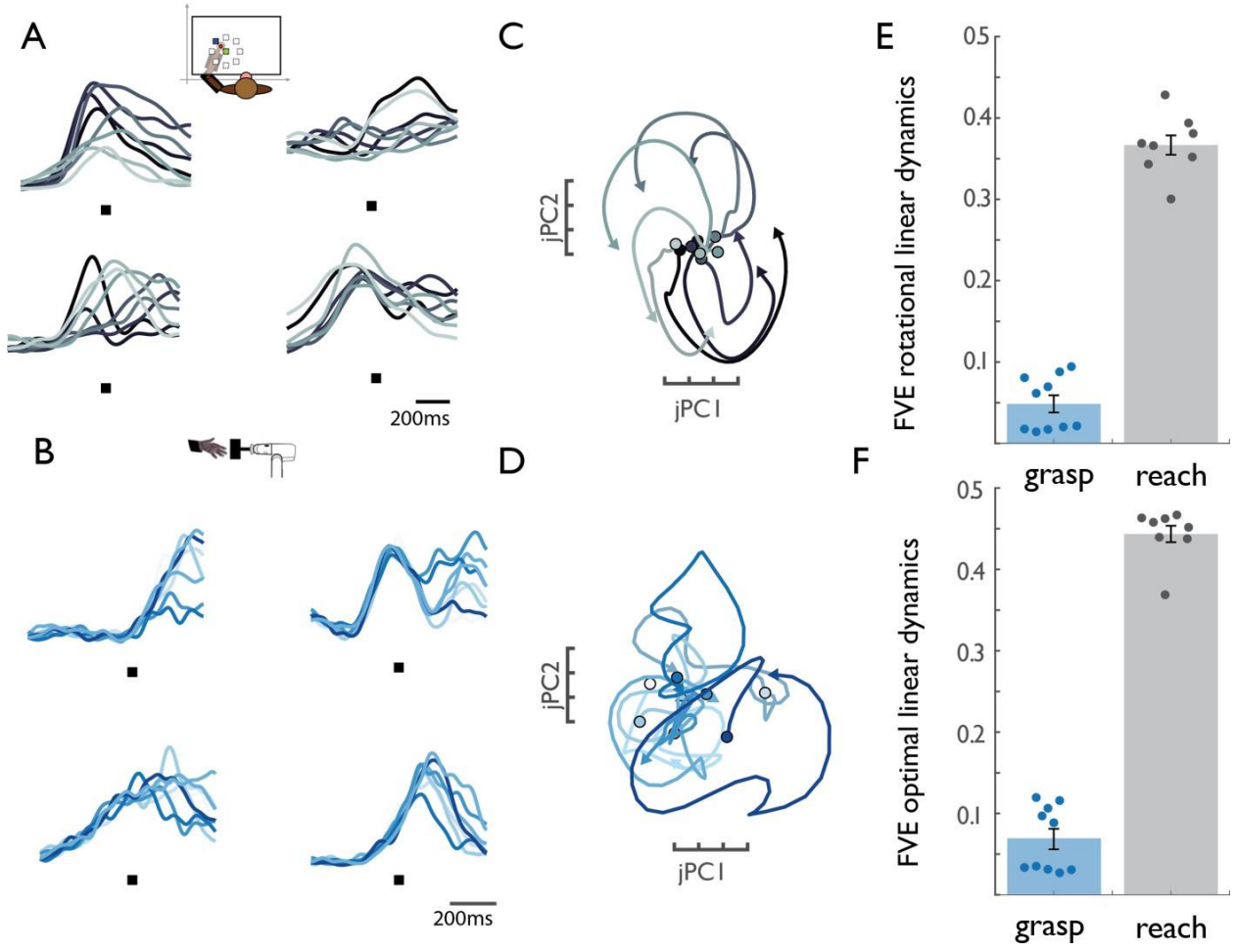

Figure 3.1 - M1 rotational dynamics during reaching and grasping. (A) Tangling metric (Q) for population responses in motor cortex vs. Q for kinematics during reaching. Kinematic tangling is higher than neural tangling, consistent with motor cortex acting as a pattern generation during reach. (B) Q-M1 population vs. Q-kinematics for grasping. Neural tangling is higher than kinematic tangling, which argues against pattern generation as the dominant mode during grasp. (C) Q-M1 population vs. Q-SCx population. Neural tangling is similar in M1 and SCx. For plots A-C, each point represents the max Q value for a (trial-averaged) neural state at a single time point and single task condition for one monkey (Monkey 1, Dataset 1). (D) Log of Q-motor/Q-kinematics of the arm during reach (KA), Q-motor/Q-kinematics of the hand during grasp (KH), and Q-motor/Q-sensory during grasp (Ns). Each point represents the log-ratio for a single condition and time point (pooled across two monkeys each). Black bars denote the mean log-ratio. The differences between reaching-derived and grasping-derived log-ratios are significant and substantial (two-sample two-sided equal-variance t-test: KH | t(2978)=-43, p=1.03e-130; Ns |t(2978)=-39 p=1.87e-121). Tangling is insensitive to the precise dimensionality, provided it exceeds a minimum dimensionality (Figure 3—figure supplement 1).

Given the poor fit of rotational dynamics to neural activity during grasp, we next assessed whether activity could be described by a linear dynamical system of any kind. To test for linear dynamics, we fit a regression model using the first 10 principal components of the M1 population activity ($x(t)$) to predict their rates of change (dx/dt). We found $x(t)$ to be far less predictive of dx/dt in grasp than in reach, suggesting much weaker linear dynamics in M1 during grasp (Figure 3.1F). We verified that these results were not an artifact of data alignment, movement epoch, peak firing rate, smoothing, population size, or number of behavioral conditions (Online materials Figure 1—figure supplement 2).

The possibility remains that dynamics are present in M1 during grasp, but that they are higher-dimensional or more nonlinear than during reach. Indeed, M1 population activity during a reach-grasp-manipulate task is higher dimensional than is M1 activity during reach alone (Rouse & Schieber, 2018). In light of this, we used Latent Factor Analysis via Dynamical Systems (LFADS) to infer and exploit latent dynamics and thereby improve estimation of single-trial firing rates, then applied a decoder to evaluate the level of improvement. Naturally, the benefit of LFADS is only realized if the neural population acts like a dynamical system. Importantly, such dynamics are minimally constrained and can, in principle, be arbitrarily high dimensional and/or highly nonlinear. First, as expected, we found that in both datasets, neural reconstruction of single trials improved with LFADS (Online materials Figure 2—figure supplement 1A,B). However, LFADS yielded a significantly greater improvement in reconstruction accuracy for reach than for grasp ($t(311) = 7.07$, $p=5.11e-12$; Online materials Figure 2—figure supplement 1B). Second, a standard Kalman filter was used to decode joint angle kinematics from the inferred latent factors (Figure 3.2). If latent dynamics in M1 play a key role in the generation of temporal sequences of muscle activations, which in turn give rise to movement, LFADS should substantially improve kinematic

decoding. Replicating previous results, we found decoding accuracy to be substantially improved for reaching when processing firing rates using LFADS (Figure 3.2A,C) (R^2 = 0.93 and 0.57 with and without LFADS, respectively). In contrast, LFADS offered minimal improvement in accuracy when decoding grasping kinematics in two monkeys (Figure 3.2B,C) (R^2 = 0.46 and 0.37), regardless of the latent dimensionality of the model (Online materials Figure 2—figure supplement 1C) or whether external inputs were included (Online materials Figure 2—figure supplement 1D). These decoding results demonstrate that the strong dynamical structure seen in the M1 population activity during reach is not observed during grasp, even when dimensionality and linearity constraints are relaxed.

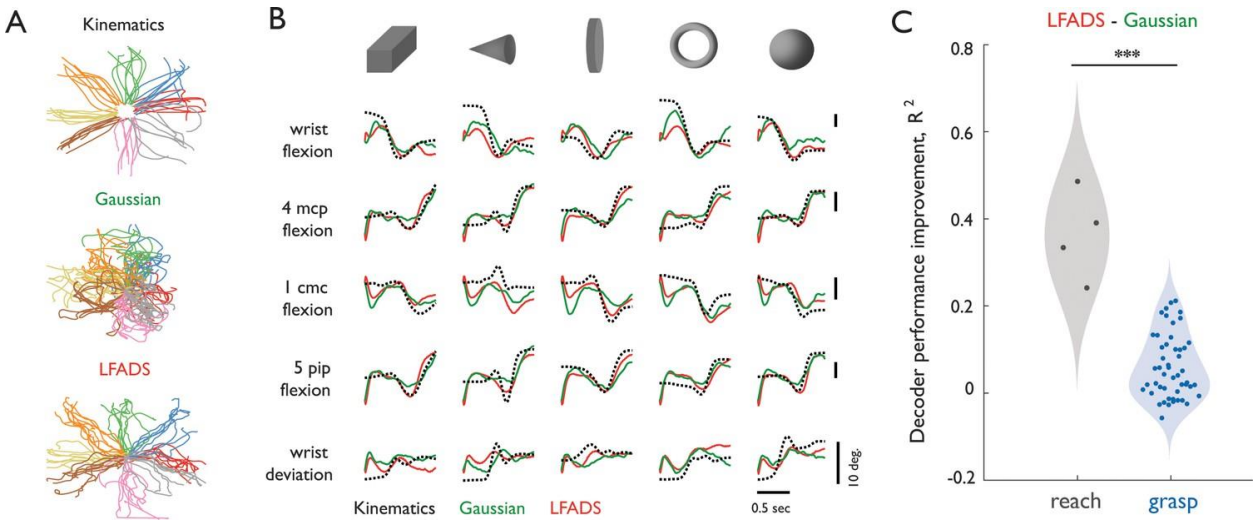

*Figure 3.2 - Decoding of kinematics based on population activity pre-processed with Gaussian smoothing or with LFADS. (A) End-point coordinates of center-out reaching with actual kinematics (top) or kinematics reconstructed with neural data preprocessed with Gaussian smoothing (middle) or LFADS (bottom). Coordinates are color-coded according to the eight directions of movement. While conditions are visually separable in both Gaussian and LFADS reconstructions, the later provides a smoother and more reliable estimate. (B) Single-trial time-varying angles of five hand joints (black, dashed) from monkey three as it grasped five objects along with their decoded counterparts (Gaussian-smoothed in green, LFADS-inferred in red). Both Gaussian-smoothed and LFADS-inferred firing rates yield similar decoding errors. Here, '4mcp flexion' refers to flexion/extension of the fourth metacarpophalangeal joint; '5pip flexion' - flexion/extension of the fifth proximal interphalangeal joint; and '1cmc flexion' - flexion/extension of the first carpo-metacarpal joint. (C) Difference in performance gauged by the coefficient of determination between decoders with LFADS and Gaussian smoothing for reach (gray) and grasp (blue). Each point denotes the mean performance increase across 10-fold cross-validation of all degrees of freedom pooled across monkeys for reach (2 monkeys with 2 DoFs each) and grasp (2 monkeys with 22 and 29 DoFs, respectively). All decoders were fit using a population of 37 M1 neurons. LFADS leads to significantly larger decoder performance improvement for reach than for grasp. Stars indicate significance of a Mann-Whitney-Wilcoxon test for unmatched samples: *** - alpha of 0.001 for one-sided alternative hypothesis.*

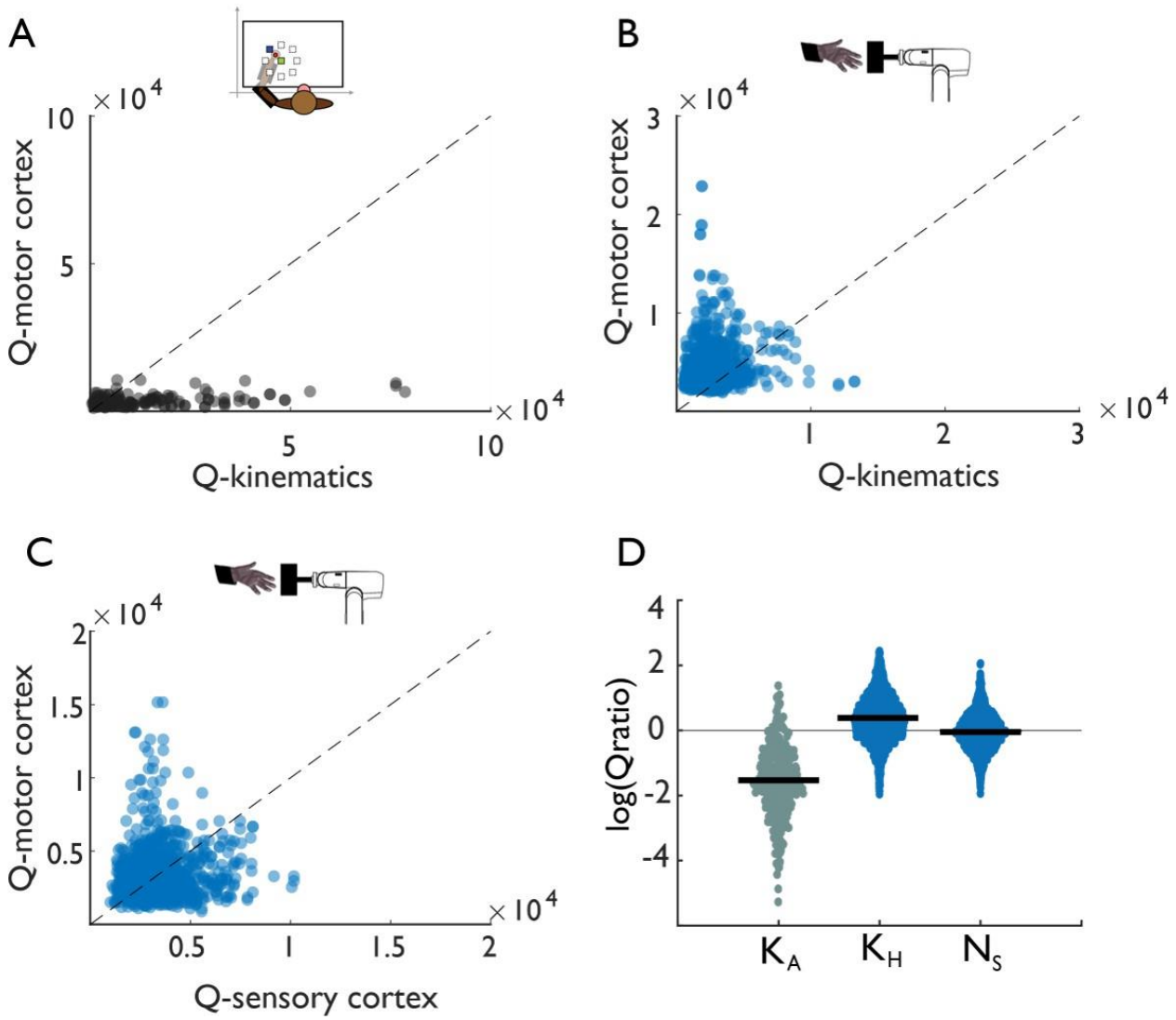

Figure 3.3 - Tangling in reach and grasp. (A) Tangling metric (Q) for population responses in motor cortex vs. Q for kinematics during reaching. Kinematic tangling is higher than neural tangling, consistent with motor cortex acting as a pattern generation during reach. (B) Q-M1 population vs. Q-kinematics for grasping. Neural tangling is higher than kinematic tangling, which argues against pattern generation as the dominant mode during grasp. (C) Q-M1 population vs. Q-SCx population. Neural tangling is similar in M1 and SCx. For plots A-C, each point represents the max Q value for a (trial-averaged) neural state at a single time point and single task condition for one monkey (Monkey 1, Dataset 1). (D) Log of Q-motor/Q-kinematics of the arm during reach (KA), Q-motor/Q-kinematics of the hand during grasp (KH), and Q-motor/Q-sensory during grasp (Ns). Each point represents the log-ratio for a single condition and time point (pooled across two monkeys each). Black bars denote the mean log-ratio. The differences between reaching-derived and grasping-derived log-ratios are significant and substantial (two-sample two-sided equal-variance t-test: KH | t(2978)=-43, p=1.03e-130; Ns |t(2978)=-39 p=1.87e-121). Tangling is insensitive to the precise dimensionality, provided it exceeds a minimum dimensionality (Figure 3—figure supplement 1).

As a separate way to examine the neural dynamics in grasping responses, we computed a neural 'tangling' metric, which assesses the degree to which network dynamics are governed by a smooth and consistent flow field (Russo et al., 2018). In a smooth, autonomous dynamical system, neural trajectories passing through nearby points in state space should have similar derivatives. The

tangling metric (*Q*) assesses the degree to which this is the case over a specified (reduced) number of dimensions. During reaching, muscle activity and movement kinematics have been shown to exhibit more tangling than does M1 activity, presumably because the cortical circuits act as a dynamical pattern generator whereas muscles are input-driven (Russo et al., 2018). We replicated these results for reaching: neural activity was much less tangled than the corresponding arm kinematics (position, velocity, and acceleration of joint angles) (Figure 3.3A), as long as the subspace was large enough (>2D), (Online materials Figure 3—figure supplement 1). For grasp, however, M1 activity was as tangled as the corresponding hand kinematics, or even more so (Figure 3.3B), over all subspaces (Online materials Figure 3—figure supplement 1). Next, we compared tangling in the grasp-related activity in M1 to its counterpart in SCx, which, as a sensory area, is expected to exhibit tangled activity (as shown during reaching movements [Russo et al., 2018]). Surprisingly, population activity patterns in both M1 and SCx were similarly tangled during grasp (Figure 3.3C). In summary, M1 responses during grasp do not exhibit the properties of an autonomous dynamical system, but rather are tangled to a similar degree as are sensory cortical responses (Figure 3.3D).

3.4 Discussion

We find that M1 does not exhibit low-dimensional dynamics during grasp as it does during reach (Churchland et al., 2012), reach-to-grasp (Rouse and Schieber, 2018), or reach-like center-out pointing (Pandarinath et al., 2015). The difference between reach- and grasp-related neuronal dynamics seems to stem from the fundamentally different kinematics and functions of these movements, rather than from effector-specific differences, since dynamics are observed for reach-like finger movements. That rotational dynamics are observed in reach-to-grasp likely reflects the reaching component of the behavior, consistent with the observation that movement signals are

broadcast widely throughout motor cortex (Musall et al., 2019; Stavisky et al., 2019; Willett et al., 2020).

Other factors might also explain the different dynamical profiles in M1 between reach and grasp. One might conjecture that M1 population dynamics are much higher dimensional and/or more nonlinear for grasp than for reach, which might explain our failure to detect dynamics in grasp-related M1 activity. However, both LFADS (Pandarinath et al., 2018); Online materials Figure 2—figure supplement 1) and the tangling metric (Online materials Figure 3—figure supplement 1) can accommodate high-dimensional systems and some degree of nonlinearity in the dynamics. We verified that our failure to observe dynamics did not stem from a failure to adequately characterize a high-dimensional grasp-related response in M1 commensurate with the dimensionality of the movement (See 'Dimensionality of the neuronal response' in the Materials and methods, Online materials Figure 3—figure supplement 2). We cannot exclude the possibility that dynamics may be observed in a much higher dimensional space than we can resolve with our sample, one whose dimensionality far exceeds that of the movement itself. To test this hypothesis will require large-scale neural recordings obtained during grasping.

Another possibility is that M1 dynamics are under greater influence from extrinsic inputs for grasp than for reach: inputs can push neuronal activity away from the trajectories dictated by the intrinsic dynamics, thereby giving rise to tangling. M1 receives input from large swaths of the brain that each exhibit their own dynamics, including the supplementary motor area (Lara et al., 2018; Russo et al., 2018), premotor and posterior parietal cortices (Michaels et al., 2018), and motor thalamus (Sauerbrei et al., 2020), in addition to responding to somatosensory and visual inputs (Suminski et al., 2010). Our findings are consistent with the hypothesis that grasp involves more inputs to M1

than does reach, or that grasp-related inputs are more disruptive to the intrinsic dynamics in M1 than are their reach-related counterparts (Online materials Figure 2—figure supplement 1).

Whatever the case may be, the low-dimensional linear dynamics observed in M1 during reaching are not present during grasping, consistent with an emerging view that the cortical circuits that track and control the hand differ from those that track and control the proximal limb (Goodman et al., 2019; Rathelot & Strick, 2009).

3.5 Materials and methods

3.5.1 Behavior and neurophysiological recordings for grasping task

We recorded single-unit responses in the primary motor and somatosensory cortices (M1 and SCx) of two monkeys (Macaca mulatta) (M1: $N_1 = 58$, $N_2 = 53$ | SCx: $N_1 = 26$ $N_2 = 28$) as they grasped each of 35 objects an average of 10 times per session. We refer to these recordings as Dataset 1 and Dataset 2, which were recorded from Monkey 1 and Monkey 2, respectively. Neuronal recordings were obtained across 6 and 9 sessions, respectively, and are used in the jPCA and tangling analyses. We also recorded simultaneously from populations of neurons in M1 in two monkeys ($N_3 = 44$, $N_4 = 37$) during a single session of this same task. These are called, respectively, Dataset 3 and Dataset 4. The first of these (N_3) was recorded from a third Monkey, Monkey 3; the second population of simultaneously recorded neurons (N_4) was obtained from the same monkey (Monkey 1) as the first set of sequentially recorded neurons (N_1). The recordings in Monkey 1 were achieved with different arrays and separated by 3 years. Simultaneously recorded populations were used for the decoding analyses.

On each trial (Online materials Figure 1 – supplement 1), one of 25 objects was manually placed on the end of an industrial robotic arm (MELFA RV-1A, Mitsubishi Electric, Tokyo, Japan). After a 1-3 second delay, randomly drawn on a trial-by-trial basis, the robot translated the object toward

the animal's stationary hand. The animal was required to maintain its arms in the primate chair for the trial to proceed: if light sensors on the arm rest became unobstructed before the robot began to move, the trial was aborted. We also confirmed that the animal produced minimal proximal limb movement by inspecting videos of the experiments and from the reconstructed kinematics. The object began 12.8 cm from the animal's hand and followed a linear trajectory toward the hand at a constant speed of 16 cm/s for a duration of 800 ms. As the object approached, the animal shaped its hand to grasp it. Some of the shapes were presented at different orientations, requiring a different grasping strategy, yielding 35 unique "objects". Each object was presented eight to eleven times in a given session.

The timing of start of movement, maximum aperture, and grasp events were inferred on the basis of the recorded kinematics. A subset of trials from each session were manually scored for each of these three events. On the basis of these training data, joint angular kinematic trajectories spanning 200 ms before and after each frame were used as features to train a multi-class linear discriminant classifier to discriminate among these four classes: all three events of interest and "no event". Log likelihood ratio was used to determine which "start of movement", "maximum aperture", and "grasp" times were most probable relative to "no event". Events were sequentially labeled for each trial to enforce the constraint that start of movement precedes maximum aperture, and maximum aperture precedes grasp. The median interval between the start of movement and maximum aperture was 450 ± 85 ms (median ± interquartile range) for Monkey 1 (across both sets of recordings), 240.0 ± 10.0 ms for Monkey 2, and 456 ± 216 ms for Monkey 3. The interval between maximum aperture and grasp was 356 ± 230 ms for Monkey 1, 410 ± 160 ms for Monkey 2, and 274 ± 145 ms for Monkey 3. Total grasp times from start of movement to grasp were 825 ± 280 ms for Monkey 1, 650 ± 170 ms for Monkey 2, and 755 ± 303 ms for Monkey 3.

Neural recordings were obtained from two monkeys (N_1 and N_2) using semi-chronic electrode arrays (SC96 arrays, Gray Matter Research, Bozeman, MT) (Dotson et al., 2017) (Online materials Figure 1 – supplement 1). Electrodes, which were individually depth-adjustable, were moved to different depths on different sessions to capture new units. Units spanning both M1 and SCx were recorded using these arrays, and SCx data comprise populations from both proprioceptive subdivisions of SCx, namely, Brodmann's areas 3a and 2. Simultaneous neural recordings were obtained from one monkey (N_3) using a combination of Utah electrode arrays (UEAs, Blackrock Microsystems, Inc., Salt Lake City, UT) and floating microelectrode arrays (FMAs, Microprobes for Life Science, Gaithersburg, MD) targeting rostral and caudal subdivisions of the hand representation of M1, respectively. In the other monkey (N_4), simultaneous population recordings were obtained using a single 64-channel Utah array targeting the hand representation of (rostral) M1. Single units from all sessions (treated as distinct units) were extracted using an Offline Sorter (Plexon Inc., Dallas TX). Units were identified based on inter-spike interval distribution and waveform shape and size.

Hand joint kinematics, namely the angles and angular velocities about all motile axes of rotation in the joints of the wrist and digits, were tracked at a rate of 100 Hz by means of a 14-camera motion tracking system (MX-T series, VICON, Los Angeles, CA). The VICON system tracked the three-dimensional positions of the markers, and time-varying joint angles were computed using inverse kinematics based on a musculoskeletal model of the human arm (https://simtk.org/projects/ulb_project) (F. C. Anderson & Pandy, 1999, 2001; de Leva, 1996; Delp et al., 1990; Dempster & Gaughran, 1967; Holzbaur et al., 2005; Yamaguchi & Zajac, 1989) implemented in Opensim (https://simtk.org/frs/index.php?group_id=91) (Delp et al., 2007) with segments scaled to the sizes of those in a monkey limb using Opensim's built-in scaling function.

Task and kinematic recording methods are reported in an earlier publication (Goodman et al., 2019). We used a linear discriminant classifier as detailed in this previous publication to determine whether objects indeed evoked distinct kinematics (Online materials Figure 1 – supplement 1).

All surgical, behavioral, and experimental procedures conformed to the guidelines of the National Institutes of Health and were approved by the University of Chicago Institutional Animal Care and Use Committee.

3.5.2 Behavior and neurophysiological recordings for reaching task

To compare grasp to reach, we analyzed previously-published single- and multi-unit responses from two additional M1 populations (M1: $N_5 = 76$, $N_6 = 107$) recorded from two additional monkeys (Monkeys 4 and 5, respectively) operantly trained to move a cursor in a variable delay center out reaching task (Hatsopoulos et al., 2007). These recordings are called, respectively, Dataset 5 and Dataset 6. The monkey's arm rested on cushioned arm troughs secured to links of a two-joint exoskeletal robotic arm (KINARM system; BKIN Technologies, Kingston, Ontario, Canada) underneath a projection surface. The shoulder and elbow joint angles were sampled at 500 Hz by the motor encoders of the robotic arm, and the *x* and *y* positions of the hand were computed using the forward kinematic equations. The center-out task involved movements from a center target to one of eight peripherally positioned targets (5 to 7 cm away). Targets were radially defined, spanning a full 360 degree rotation about the central target in 45 degree increments. Each trial comprised two epochs: first, an instruction period lasting 1 to 1.5 s, during which the monkey held its hand over the center target to make the peripheral target appear; second, a "go" period, cued by blinking of the peripheral target, which indicated to the monkey that it could begin to move toward the target. Following the "go" cue, movement onset was 324 ± 106 ms (median ± interquartile range) for Monkey 4 in dataset 5, and 580 ± 482 ms for Monkey 5 in dataset 6. Total

movement duration was 516 ± 336 ms for Monkey 4 in dataset 5 and 736 ± 545 ms for Monkey 5 in dataset 6. Single- and multi-unit activity was recorded from each monkey during the course of a single session using a UEA implanted in the upper limb representation of contralateral M1. All surgical, behavioral, and experimental procedures conformed to the guidelines of the National Institutes of Health and were approved by the University of Chicago Institutional Animal Care and Use Committee.

Information about all grasping and reaching datasets and their associated analyses is provided in Table 1 of Online materials.

3.5.3 Differences between reach and grasp and their potential implications for population dynamics

In this section, we discuss differences between the reach and grasp tasks that might have had an impact on the neuronal dynamics.

First, movements were cued differently in the two tasks. For reaching, targets blinked to cue movement. For grasping, there was no explicit movement cue; rather, the animals could begin preshaping their hand as soon as the robot began to move, though they had to wait for the object to reach the hand to complete their grasp and obtain a reward. Nonetheless, we found that the delay between the beginning of the robot's approach and hand movement onset (median ± interquartile range: Monkey 1 – 271 ± 100 ms; Monkey 2 – 419 ± 101 ms; numbers not available for Monkey 3) was similar to the delay in the reaching task between the go cue and start of movement. Note, moreover, that the nature of the "delay" period should have little effect on neuronal dynamics. Indeed, self-initiated reaches and those that are executed rapidly with little to no preparation are nonetheless associated with rotational M1 dynamics (Lara et al., 2018).

Second, the kinematics of reaching and grasping are quite different, and differences in the respective ranges of motion or speeds could mediate the observed differences in neuronal dynamics. However, the ranges of motion and distribution of speeds were similar for reach and grasp (Online materials Figure 1 supplement 1C-D,G), suggesting that the observed differences in neuronal dynamics are not trivial consequences of differences in the kinematics. On a related note, grasping movements with no reach (lasting roughly 700 ms) were generally slower than those reported in in the context of reach (lasting roughly 300 ms) (Bonini et al., 2014; Chen et al., 2009; Lehmann & Scherberger, 2013; Rouse & Schieber, 2018; Roy et al., 2000; Theverapperuma et al., 2006), as the animals had to wait for the robot to transport the object to their hand. Note, however, that similar constraints on movement duration and speed during reaching do not affect the presence or nature of M1 rotational dynamics during those movements (Churchland et al., 2012). As such, speed differences should not lead to qualitatively different M1 population dynamics.

Third, we considered whether grasping without reaching might simply be too "unnatural" to be controlled by stereotyped M1 dynamics. However, we observed the presence of two hallmarks of grasping behavior: a clearly-defined maximum aperture phase and the presence of hand pre-shaping (Jeannerod, 1984, 1981; Santello et al., 2002; Santello and Soechting, 1998). The latter is evidenced by a gradual improvement in our ability to classify objects based on the kinematics they evoke as the trial proceeded (Online materials Figure 1 – supplement 1E): Upon start of movement, the hand is in a generic configuration that is independent of the presented object. However, as the trial proceeds, hand kinematics become increasingly object-specific, culminating in a high classification performance just before object contact. Furthermore, grasping kinematics have been previously shown to be robust to different types of reaches (Wang and Stelmach, 1998).

3.5.4 Data Analysis

3.5.4.1 Data pre-processing

For both reach and grasp, neuronal responses were aligned to the start of movement, resampled at 100 Hz so that they would be at the same temporal resolution, averaged across trials, then smoothed by convolution with a Gaussian (25 ms S.D.). For jPCA, we then followed the data pre-processing steps described in Churchland et al. 2012: normalization of individual neuronal firing rates, subtraction of the cross-condition mean peri-event time histogram (PETH) from each neuron's response in each condition, and applying principal component analysis (PCA) to reduce the dimensionality of the population response. For LFADS and the tangling analyses, only the normalization of neurons' firing rates was performed. Although the condition-invariant response varies in a meaningful way (Kaufman et al., 2016), its inclusion obstructs our ability to use jPCA to visualize neural trajectories whose initial conditions vary, and thus our ability to use jPCA to evaluate claims of dynamical structure. Even when this component is especially large, dynamical structure in the remaining condition-dependent neural activity has been observed (Rouse and Schieber, 2018), thus subtraction of even a large condition-independent response should permit the inference of neural dynamics. We used 10 dimensions instead of six (cf. Churchland et al. 2012) as a compromise between the lower-dimensional reach data and the higher-dimensional grasp data.

3.5.4.2 jPCA

We applied to the population data (reduced to 10 dimensions by PCA) a published dimensionality reduction method, jPCA (Churchland et al., 2012), which finds orthonormal basis projections that capture rotational structure in the data. We used a similar number of dimensions for both reach and grasp, as PCA revealed no stark differences in the effective dimensionality of the neural

population between the two tasks (Online materials Figure 1 – supplement 1F). With jPCA, the neural state is compared with its derivative, and the strictly rotational dynamical system that explains the largest fraction of variance in that derivative is identified. The delay periods between the presentation/go-cue for each monkey varied, along with the reaction times, so we selected a single time interval (averaging 700 ms) that maximized rotational variance across all of them. For the reach data, data were aligned to the start of movement and the analysis window was centered on this event, whereas for the grasp data, data were aligned to maximum hand aperture, and we analyzed the interval centered on this event. In some cases, the center of this 700-ms window was shifted between -350 ms to +350 ms relative to the alignment event to obtain an estimate of how rotational dynamics change over the course of the trial (e.g., Online materials Figure 1 - supplement 2). These events were chosen for alignment as they were associated with both the largest peak firing rates and the strongest rotational dynamics. Other alignment events were also tested, to test robustness (Online materials Figure 1 – supplement 2B).

3.5.4.3 Object clustering

Each of the 35 objects was presented 10 times per session, which yields a smaller number of trials per condition than were used to assess jPCA during reaching (at least 40). To permit pooling across a larger number of trials when visualizing and quantifying population dynamics with jPCA (Figure 1), objects in the grasp task were grouped into eight object clusters on the basis of the trial-averaged similarity of hand posture across all 30 joint degrees of freedom 10 ms prior to grasp (i.e., object contact). Objects were hierarchically clustered into 8 clusters on the basis of the Ward linkage function (MATLAB clusterdata). Eight clusters were chosen to match the number of conditions in the reaching task. Cluster sizes were not uniform; the smallest comprised 2 and the largest 9 different objects, with the median cluster comprising 4 objects.

As the clustering method just described yielded different cluster sizes, we assessed an alternative clustering procedure (Online materials Figure 1 -supplement 2F) that guaranteed objects were divided into 7 equally-sized clusters (5 objects per cluster). Rather than determining cluster membership on the basis of a linkage threshold, cluster linkages were instead used to sort the objects on the basis of their dendrogram placements (MATLAB dendrogram). Clusters were obtained by grouping the first five objects in this sorted list into a common cluster, then the next five, and so on. This resulted in slightly poorer performance of jPCA (see *Quantification*).

For completeness, we also assessed jPCA without clustering (Online materials Figure 1 – supplement 2E) which also resulted in slightly poorer performance of jPCA and was considerably more difficult to visualize given the large number of conditions.

3.5.4.4 Quantification

In a linear dynamical system, the derivative of the state is a linear function of the state. We wished to assess whether a linear dynamical system could account for the neural activity. To this end, we first produced a de-noised low-dimensional neural state (X) by reducing the dimensionality of the neuronal responses to 10 using PCA. Second, we numerically differentiated X to estimate the derivative, $\dot{X}$. Next, we used regression to fit a linear model, predicting the derivative of the neuronal state from the current state: $\dot{X} = MX$. Finally, we computed the fraction of variance explained (FVE) by this model:

$$FVE = 1 - \left\|\dot{X} - MX\right\|_{fro}^2 / \left\|\dot{X} - \langle\dot{X}\rangle\right\|_{fro}^2 \qquad 3.1$$

M was constrained to be skew-symmetric (M_{skew}) unless otherwise specified; $\langle\cdot\rangle$ indicates the mean of a matrix across samples, but not across dimensions; and $\|\cdot\|_{fro}$ indicates the Frobenius

norm of a matrix. Unless otherwise specified, analysis of reaching data from each monkey was 4-fold cross-validated, whereas analysis of grasp data was 5-fold cross-validated.

3.5.4.5 Control comparisons between arm and hand data

We performed several controls comparing arm and hand data to ensure that our results were not an artifact of trivial differences in the data or pre-processing steps.

First, we considered whether alignment of the data to different events might impact results. For the arm data, we aligned each trial to target onset and movement onset (Online materials Figure 1 - supplement 2A). For the hand data, we aligned each trial to presentation of the object, movement onset, and the time at which the hand reached maximum aperture during grasp (Online materials Figure 1 – supplement 2B). Linear dynamics were strongest (though still very weak) when neuronal responses were aligned to maximum aperture, so this alignment is reported throughout the main text.

Second, we assessed whether rotations might be obscured due to differences in firing rates in the hand vs. arm responses. To this end, we compared peak firing rates for trial-averaged data from the arm and hand after pre-processing (excluding normalization) to directly contrast the inputs to the jPCA analysis given the two effectors/tasks (Online materials Figure 1 – supplement 2C). Peak firing rates were actually higher for the hand than the arm, eliminating the possibility that our failure to observe dynamics during grasp was a consequence of weak responses. We also verified that differences in dynamics could not be attributed to differences in the degree to which neurons were modulated in the two tasks. To this end, we computed the modulation range (90^{th} percentile firing – 10^{th} percentile firing) and found that modulation was similar in reach and grasp (Online materials Figure 1 – supplement 2D).

Third, we assessed whether differences in the sample size might contribute to differences in variance explained (Online materials Figure 1 – supplement 2E). To this end, we took five random samples of 55 neurons from the reaching data set – chosen to match the minimum number of neurons in the grasping data – and computed the cross-validated fraction of variance explained by the rotational dynamics. The smaller samples yielded identical fits as the full sample.

Fourth, we assessed whether the low variance explained by linear dynamics in the hand might be due to poor sampling of the joint motion space (Online materials Figure 1 – supplement 2G). To this end, we computed FVE for only rightward reaches, and found that the variance explained for all directions versus only rightward reaches were comparable. Therefore, we expect that our sampling of hand motions would not affect our ability to observe linear dynamics.

Fifth, we considered whether our smoothing kernel might impact results (Online materials Figure 1 – supplement 2H). We compared the FVE for the optimal linear dynamical system across various smooth kernels – from 5 to 40 ms – and found that the difference between hand and arm dynamics remains substantial regardless of kernel width.

Finally, since our analyses involve averaging across trials, we assessed whether trial-to-trial variability was different for reach and grasp. To this end, we computed for each neuron the coefficient of variation (CV) of spike counts over 100-ms bins around movement onset. We found the trial-to-trial variability to be stable over the trial and similar for reach and grasp (Online materials Figure 1 – supplement 2I).

3.5.4.6 Decoding

Preprocessing

For decoding, we preprocessed the neural data using one of two methods: smoothing with a Gaussian kernel ($\sigma = 20$ ms) or latent factor analysis via dynamical systems (LFADS) (Pandarinath

et al., 2018). LFADS is a generative model that assumes that observed spiking responses arise from an underlying dynamical system and estimates that system using deep learning. We used the same number of neurons in the reaching and grasping analyses to train the LFADS models and fixed the number of factors in all models to 30, at which performance of both reach and grasp models had levelled off (Online materials Figure 2 – supplement 1A). We allowed two continuous controllers while training the model, which could potentially capture the influence of external inputs on dynamics (Pandarinath et al., 2018), since these had significant positive influence on decoding performance (Online materials Figure 2 – supplement 1B). Hyper-parameter tuning was performed as previously described (Keshtkaran and Pandarinath, 2019).

Neural reconstruction

To compare our ability to reconstruct single-trial responses using Gaussian smoothing and LFADS, we first computed peri-event time histograms (PETHs) within condition using all training trials (excluding one test trial). We then computed the correlation between the firing rates of each test trial (smoothed with a Gaussian kernel or reconstructed with LFADS) with the PETH of the corresponding condition averaged across the training trails (Online materials Figure 2 – Supplement 1A). We repeated this procedure with a different trial left out for each condition. We report the difference in correlation coefficient obtained after LFADS processing and Gaussian smoothing (Online materials Figure 2 – Supplement 1B).

Kalman Filter

To predict hand and arm kinematics, we applied the Kalman filter (Kalman, 1960), commonly used for kinematic decoding (Menz et al., 2015; Okorokova et al., 2020; Wu et al., 2004). In this approach, kinematic dynamics can be described by a linear relationship between past and future states:

$$x_t = Ax_{t-1} + v_t \quad 3.1$$

where x_t is a vector of joint angles at time t, A is a state transition matrix, and v_t is a vector of random numbers drawn from a Gaussian distribution with zero mean and covariance matrix V. The kinematics x_t can be also explained in terms of the observed neural activity $z_{t-\Delta}$:

$$x_t = Bz_{t-\Delta} + w_t \quad 3.2$$

Here, $z_{t-\Delta}$ is a vector of instantaneous firing rates across a population of M1 neurons at time $t - \Delta$, preprocessed either with Gaussian kernel or LFADS, B is an observation model matrix, and w_t is a random vector drawn from a Gaussian distribution with zero mean and covariance matrix W. We tested multiple values of the latency, Δ, and report decoders using the latency that maximized decoder accuracy (150 ms).

We estimated the matrices A, B, V, W using linear regression on each training set, and then used those estimates in the Kalman filter update algorithm to infer the kinematics of each corresponding test set (see [50,51] for details). Briefly, at each time t, kinematics were first predicted using the state transition equation (3.1), then updated with observation information from equation (3.2). Update of the kinematic prediction was achieved by a weighted average of the two estimates from (3.1) and (3.2): the weight of each estimate was inversely proportional to its uncertainty (determined in part by V and W for the estimates based on x_{t-1} and $z_{t-\Delta}$, respectively), which changed as a function of time and was thus recomputed for every time step.

To assess decoding performance, we performed 10-fold cross-validation in which we trained the parameters of the filter on a randomly selected 90% of the trials and tested the model using the remaining 10% of trials. Importantly, we trained separate Kalman filters for the two types of neural preprocessing techniques (Gaussian smoothing and LFADS) and then compared their performance

on the same trials. Performance was quantified using the coefficient of determination (R^2) for the held-out trials across test sets.

3.5.4.7 Tangling

We computed tangling of the neural population data (reduced to 20 dimensions by PCA) using a published method (Russo et al., 2018). In brief, the tangling metric estimates the extent to which neural population trajectories are inconsistent with what would be expected if they were governed by an autonomous dynamical system, with smaller values indicating consistency with such dynamical structure. Specifically, tangling measures the degree to which similar neural states, either during different movements or at different times for the same movement, are associated with different derivatives. This is done by finding, for each neural state (indexed by t), the maximum value of the tangling metric $Q(t)$ across all other neural states (indexed by t'):

$$Q(t) = \max_{t'} \frac{\|\dot{x}_t - \dot{x}_{t'}\|^2}{\|x_t - x_{t'}\|^2 + \varepsilon} \quad 3.3$$

Here, x_t is the neural state at time *t* (a 20-dimensional vector containing the neural responses at that time), $\dot{x}_t$ is the temporal derivative of the neural state (estimated numerically), and $\|\cdot\|$ is the Euclidean norm, while ε is a small constant added for robustness to noise (Russo et al., 2018). This analysis is not constrained to work solely for neural data; indeed, we also apply this same analysis to trajectories of joint angular kinematics to compare their tangling to that of neural trajectories.

The neural data were pre-processed using the same alignment, trial averaging, smoothing, and normalization methods described above. Joint angles were collected for both hand and arm data. For this analysis, joint angle velocity and acceleration were computed (six total dimensions for arm, 90 dimensions for hand). For reaching, we analyzed the epoch from 200 ms before to 100 ms after movement onset. For grasping, we analyzed the epoch starting 200 ms before to 100 ms after

maximum aperture. Neuronal responses were binned in 10 ms bins to match the sampling rate of the kinematics.

The tangling metric is partially dependent on the dimensionality of the underlying data. To eliminate the possibility that our results were a trivial consequence of selecting a particular number of principal components, we tested tangling at different dimensionalities and selected the dimensionality at which Q had largely leveled off for both the population neural activity and kinematics (Online materials Figure 3 – supplement 1). Namely, we report results using 6 principal components (the maximum) for reach kinematics and their associated neural responses, and using 20 for kinematics and neuronal responses during grasp.

3.5.4.8 Dimensionality of the neuronal response

One possibility is that our failure to observe autonomous dynamics during grasp stems from a failure to properly characterize the neural manifold, which in principle could be much higher dimensional for grasp than it is for reach. However, the first D dimensions of a manifold can be reliably estimated from fewer than 2*D projections if two conditions hold: the eigenvalue spectrum is not flat, and the samples approximate random projections of the underlying manifold (Halko et al., 2011). The scree plot shows that the first condition is met (Online materials Figure 1 – supplement 1F). To evaluate the second condition and determine whether neurons are random projections of the low-dimensional manifold, we applied a Gine-Ajne test (Prentice, 1978) to the first 5, 10, and 20 PCs. We found that the null hypothesis of spherical uniformity was not rejected ($p>0.5$ for all dimensionalities and data sets). While we cannot rule out that the possibility that there exists a small, unrecorded fraction of neurons that span a disjoint manifold subspace from that we measured, the failure to reject spherical uniformity provides evidence that these neurons approximate random projections. To further examine the possibility that dynamics occupy a space

that we were unable to resolve with our neuronal sample, we implemented LFADS with a different number of latent factors. We found that, to the extent that decoding performance improved with additional latent factors, it levelled off at ~10 factors (Online materials Figure 2 – supplement 1). If the dynamics were distributed over a high-dimensional manifold, we might expect that performance would increase slowly with the number of latent factors over the entire range afforded by the sample size. This was not the case.

Yet another possibility we considered is that the neuronal manifold beyond the first few dimensions reflects noise, which would preclude the identification of dynamics embedded in higher order dimensions. To examine this possibility, we assessed our ability to relate the monkeys' behavior during the grasp task to the neural data over subsets of dimensions. First, we found that the ability to classify objects based on the population response projected on progressively smaller subspaces – removing high-variance principal components first – remained above chance even after dozens of PCs were removed. This suggests that behaviorally relevant neuronal activity was distributed over many dimensions, and that this signal clearly rose above the noise (Online materials Figure 3 - supplement 2A). For this analysis, we used multiclass linear discriminant analysis based on population responses evoked over a 150-ms window before object contact. Second, we found that the ability to decode kinematics based on the population response projected on progressively smaller subspaces remained above chance after removal of many PCs, consistent with the classification analysis (Online materials Figure 3 – supplement 2B). For this analysis, we used population responses over an 800-ms window centered on maximum aperture for reaching and movement onset for grasping. Thus, high-order PCs do not simply reflect noise but rather comprise behaviorally relevant signals.

In summary, then, our sample size is sufficient, in principle, to recover dynamics embedded in a high-dimensional manifold. The weak dynamics in the grasping response that we did recover occupy a low-dimensional manifold, and we were able to resolve the population response for the grasping behavior across a large number of dimensions (40+ principal components).

3.5.4.9 Statistics

For most of analyses, sample sizes were large and data were distributed approximately normally so we used two-sided t-test. However, for some analyses, the data were right-skewed and the sample size was small, so we used non-parametric tests, either the Wilcoxon signed rank test or the Mann-Whitney-Wilcoxon test depending on whether the samples were matched (for example, comparison of same kinematic DoFs reconstructed with either Gaussian smoothing or LFADS) or not (for example, comparison of kinematic DoFs reconstruction from different datasets).

3.6 Data availability

The data that support the findings of this study have been deposited in Dryad, accessible at https://doi.org/10.5061/dryad.xsj3tx9cm .

3.7 References

Anderson, F. C., & Pandy, M. G. (1999). A Dynamic Optimization Solution for Vertical Jumping in Three Dimensions. *Computer Methods in Biomechanics and Biomedical Engineering*, *2*(3), 201–231. https://doi.org/10.1080/10255849908907988

Anderson, F. C., & Pandy, M. G. (2001). Dynamic Optimization of Human Walking. *Journal of Biomechanical Engineering*, *123*(5), 381–390. https://doi.org/10.1115/1.1392310

Bonini, L., Maranesi, M., Livi, A., Fogassi, L., & Rizzolatti, G. (2014). Space-Dependent Representation of Objects and Other's Action in Monkey Ventral Premotor Grasping Neurons. *Journal of Neuroscience*, *34*(11), 4108–4119. https://doi.org/10.1523/JNEUROSCI.4187-13.2014

Chen, J., Reitzen, S. D., Kohlenstein, J. B., & Gardner, E. P. (2009). Neural Representation of Hand Kinematics During Prehension in Posterior Parietal Cortex of the Macaque Monkey. *Journal of Neurophysiology*, *102*(6), 3310–3328. https://doi.org/10.1152/jn.90942.2008

Churchland, M. M., Cunningham, J. P., Kaufman, M. T., Foster, J. D., Nuyujukian, P., Ryu, S. I., & Shenoy, K. V. (2012). Neural population dynamics during reaching. *Nature*, *487*(7405), 51–56. https://doi.org/10.1038/nature11129

de Leva, P. (1996). Adjustments to Zatsiorsky-Seluyanov's segment inertia parameters. *Journal of Biomechanics*, *29*(9), 1223–1230. https://doi.org/10.1016/0021-9290(95)00178-6

Delp, S. L., Anderson, F. C., Arnold, A. S., Loan, P., Habib, A., John, C. T., Guendelman, E., & Thelen, D. G. (2007). OpenSim: Open-source software to create and analyze dynamic simulations of movement. *IEEE Transactions on Bio-Medical Engineering*, *54*(11), 1940–1950. https://doi.org/10.1109/TBME.2007.901024

Delp, S. L., Loan, J. P., Hoy, M. G., Zajac, F. E., Topp, E. L., & Rosen, J. M. (1990). An interactive graphics-based model of the lower extremity to study orthopaedic surgical procedures. *IEEE Transactions on Biomedical Engineering*, *37*(8), 757–767. https://doi.org/10.1109/10.102791

Dempster, W. T., & Gaughran, G. R. L. (1967). Properties of body segments based on size and weight. *American Journal of Anatomy*, *120*(1), 33–54. https://doi.org/10.1002/aja.1001200104

Dotson, N. M., Hoffman, S. J., Goodell, B., & Gray, C. M. (2017). A Large-Scale Semi-Chronic Microdrive Recording System for Non-Human Primates. *Neuron*, *96*(4), 769-782.e2. https://doi.org/10.1016/j.neuron.2017.09.050

Goodman, J. M., Tabot, G. A., Lee, A. S., Suresh, A. K., Rajan, A. T., Hatsopoulos, N. G., & Bensmaia, S. (2019). Postural Representations of the Hand in the Primate Sensorimotor Cortex. *Neuron*, *104*(5), 1000-1009.e7. https://doi.org/10.1016/j.neuron.2019.09.004

Hatsopoulos, N. G., Xu, Q., & Amit, Y. (2007). Encoding of movement fragments in the motor cortex. *The Journal of Neuroscience: The Official Journal of the Society for Neuroscience*, *27*(19), 5105–5114. https://doi.org/10.1523/JNEUROSCI.3570-06.2007

Holzbaur, K. R. S., Murray, W. M., & Delp, S. L. (2005). A Model of the Upper Extremity for Simulating Musculoskeletal Surgery and Analyzing Neuromuscular Control. *Annals of Biomedical Engineering*, *33*(6), 829–840. https://doi.org/10.1007/s10439-005-3320-7

Ingram, J. N., Körding, K. P., Howard, I. S., & Wolpert, D. M. (2008). The statistics of natural hand movements. *Experimental Brain Research*, *188*(2), 223–236. https://doi.org/10.1007/s00221-008-1355-3

Lara, A. H., Elsayed, G. F., Zimnik, A. J., Cunningham, J. P., & Churchland, M. M. (2018). Conservation of preparatory neural events in monkey motor cortex regardless of how movement is initiated. *ELife*, *7*, e31826. https://doi.org/10.7554/eLife.31826

Lehmann, S. J., & Scherberger, H. (2013). Reach and Gaze Representations in Macaque Parietal and Premotor Grasp Areas. *Journal of Neuroscience*, *33*(16), 7038–7049. https://doi.org/10.1523/JNEUROSCI.5568-12.2013

Michaels, J. A., Dann, B., Intveld, R. W., & Scherberger, H. (2018). Neural Dynamics of Variable Grasp-Movement Preparation in the Macaque Frontoparietal Network. *The Journal of Neuroscience: The Official Journal of the Society for Neuroscience*, *38*(25), 5759–5773. https://doi.org/10.1523/JNEUROSCI.2557-17.2018

Overduin, S. A., d'Avella, A., Roh, J., Carmena, J. M., & Bizzi, E. (2015). Representation of Muscle Synergies in the Primate Brain. *The Journal of Neuroscience: The Official Journal of the Society for Neuroscience*, *35*(37), 12615–12624. https://doi.org/10.1523/JNEUROSCI.4302-14.2015

Pandarinath, C., O'Shea, D. J., Collins, J., Jozefowicz, R., Stavisky, S. D., Kao, J. C., Trautmann, E. M., Kaufman, M. T., Ryu, S. I., Hochberg, L. R., Henderson, J. M., Shenoy, K. V., Abbott, L. F., & Sussillo, D. (2018). Inferring single-trial neural population dynamics using

sequential auto-encoders. *Nature Methods*, *15*(10), 805–815. https://doi.org/10.1038/s41592-018-0109-9

Rathelot, J.-A., & Strick, P. L. (2009). Subdivisions of primary motor cortex based on cortico-motoneuronal cells. *Proceedings of the National Academy of Sciences*, *106*(3), 918–923. https://doi.org/10.1073/pnas.0808362106

Rouse, A. G., & Schieber, M. H. (2018). Condition-Dependent Neural Dimensions Progressively Shift during Reach to Grasp. *Cell Reports*, *25*(11), 3158-3168.e3. https://doi.org/10.1016/j.celrep.2018.11.057

Roy, A. C., Paulignan, Y., Farnè, A., Jouffrais, C., & Boussaoud, D. (2000). Hand kinematics during reaching and grasping in the macaque monkey. *Behavioural Brain Research*, *117*(1), 75–82. https://doi.org/10.1016/S0166-4328(00)00284-9

Russo, A. A., Bittner, S. R., Perkins, S. M., Seely, J. S., London, B. M., Lara, A. H., Miri, A., Marshall, N. J., Kohn, A., Jessell, T. M., Abbott, L. F., Cunningham, J. P., & Churchland, M. M. (2018). Motor Cortex Embeds Muscle-like Commands in an Untangled Population Response. *Neuron*, *97*(4), 953-966.e8. https://doi.org/10.1016/j.neuron.2018.01.004

Santello, M., Flanders, M., & Soechting, J. F. (1998). Postural hand synergies for tool use. *The Journal of Neuroscience: The Official Journal of the Society for Neuroscience*, *18*(23), 10105–10115. https://doi.org/10.1523/JNEUROSCI.18-23-10105.1998

Sauerbrei, B. A., Guo, J.-Z., Cohen, J. D., Mischiati, M., Guo, W., Kabra, M., Verma, N., Mensh, B., Branson, K., & Hantman, A. W. (2020). Cortical pattern generation during dexterous movement is input-driven. *Nature*, *577*(7790), 386–391. https://doi.org/10.1038/s41586-019-1869-9

Shenoy, K. V., Sahani, M., & Churchland, M. M. (2013). Cortical control of arm movements: A dynamical systems perspective. *Annual Review of Neuroscience*, *36*, 337–359. https://doi.org/10.1146/annurev-neuro-062111-150509

Suminski, A. J., Tkach, D. C., Fagg, A. H., & Hatsopoulos, N. G. (2010). Incorporating Feedback from Multiple Sensory Modalities Enhances Brain–Machine Interface Control. *The Journal of Neuroscience*, *30*(50), 16777. https://doi.org/10.1523/JNEUROSCI.3967-10.2010

Theverapperuma, L. S., Hendrix, C. M., Mason, C. R., & Ebner, T. J. (2006). Finger movements during reach-to-grasp in the monkey: Amplitude scaling of a temporal synergy. *Experimental Brain Research*, *169*(4), 433–448. https://doi.org/10.1007/s00221-005-0167-y

Tresch, M. C., & Jarc, A. (2009). The case for and against muscle synergies. *Current Opinion in Neurobiology*, *19*(6), 601–607. https://doi.org/10.1016/j.conb.2009.09.002

Yamaguchi, G. T., & Zajac, F. E. (1989). A planar model of the knee joint to characterize the knee extensor mechanism. *Journal of Biomechanics*, *22*(1), 1–10. https://doi.org/10.1016/0021-9290(89)90179-6

Chapter 4 | Kinematic and kinetic representations in the motor cortex of macaques

4.1 Abstract

From prehension to pianism, object interactions require precise control of both the movement of the hand and the forces it exerts on objects. The time-varying posture of the hand has been shown to be encoded in the activity of populations of neurons in the primary motor cortex (M1) before contact with an object. Less is known about kinematic representation in M1 post contact, or representation of manual forces that inevitably come into play to maintain contact with the object and manipulate it. One hypothesis is that force and kinematic representations are independent, while an alternative assumes joint coding for force and kinematics by the same neural populations. To study this question, we trained non-human primates to grasp sensorized objects with an instructed amount of force. We monitored both their time-varying hand movements and manual forces, as we recorded neural activity from M1. We then characterized the responses of individual units and identified subpopulations that encode kinematics, forces or both. We found that force signals in M1 are much weaker than their kinematic counterparts and can only be harnessed using decoders that exploit non-linear neural dynamics.

4.2 Introduction

The hand is a highly versatile organ, capable of executing a wide range of movements, from the mundane – like grasping – to the highly skilled – like playing a musical instrument. Manual behavior relies heavily on the primary motor cortex (M1, Broadman's area 4) (Lemon, 2008; Sobinov & Bensmaia, 2021), as evidenced by the severe deficits that result from lesions to M1 (Isa, 2019; Rouiller et al., 1998). The majority of studies investigating limb movement

representations in M1 have focused on the proximal joints (shoulder and elbow) (Georgopoulos et al., 1992; Paninski et al., 2004) while the distal joints (wrist and hand) have received less attention due to the challenges of tracking manual behavior (Schaffelhofer & Scherberger, 2012). The few studies of hand representations in M1 focused on kinematic representations before contact with the object is established. In these studies, M1 neurons were shown to encode time-varying hand posture (Goodman et al., 2019; Menz et al., 2015; E. V. Okorokova et al., 2020). A hallmark of manual behavior, however, is that it involves interactions with objects and requires the precise regulation of forces exerted on them (Sobinov & Bensmaia, 2021). While the presence of a signal related to manual force has been identified in M1 (Evarts, 1968; Gardner et al., 2007; Georgopoulos et al., 1992; Hendrix et al., 2009; Hepp-Reymond et al., 1999; Intveld et al., 2018; Kalaska et al., 1989; Maier et al., 1993; Wannier et al., 1991), the relationship between M1 responses and force remains to be elucidated due in large part to experimental limitations. Indeed, to disentangle the dependence of M1 responses on kinematics and interaction forces requires detailed and heretofore unavailable access to all of these behavioral variables.

To overcome these technical challenges, we constructed an experimental apparatus that allows us to track hand kinematics and interaction forces with unprecedented precision while monkeys perform a prehensile task. We then recorded neural activity from a population of M1 neurons while animals performed this task and assessed the degree to which individual neurons encode hand kinematics and forces. We found that M1 activity carries information about both kinematics and force but that force signals are much weaker than their kinematic counterparts. We then built decoders of kinematics and force to investigate the population-level representation of these movement variables. We found that linear decoders of force perform poorly compared to their kinematic counterparts. However, decoders that can exploit neural dynamics can reliably extract

force information from M1 responses. These results suggest that M1 encodes kinematics and forces differently, which has implications for the development of brain-controlled bionic hands (Downey et al., 2018; Rastogi et al., 2021).

4.3 Results

4.3.1 Grasp force task

Two rhesus macaques (M and P) each performed a grasping task requiring them to exert a visually cued amount of force on a manipulandum that consists of two thin metal plates mounted on motorized stages that allow to change the distance between plates and their rotation (Figure 4.1A). These manipulations were designed to mimic changes in the size and orientation of a grasped object and to elicit different hand postures. The plate surfaces were equipped with high-resolution sensor sheets (Tekscan) that enabled real-time monitoring of grasp force (Figure 4.1B). Each trial was initiated when the target force level was indicated on an LED display. When the monkey made contact with the object, another LED display tracked the total force exerted on the plates (the summed output of all the sensors on the object). Monkeys received a juice reward for maintaining the target force

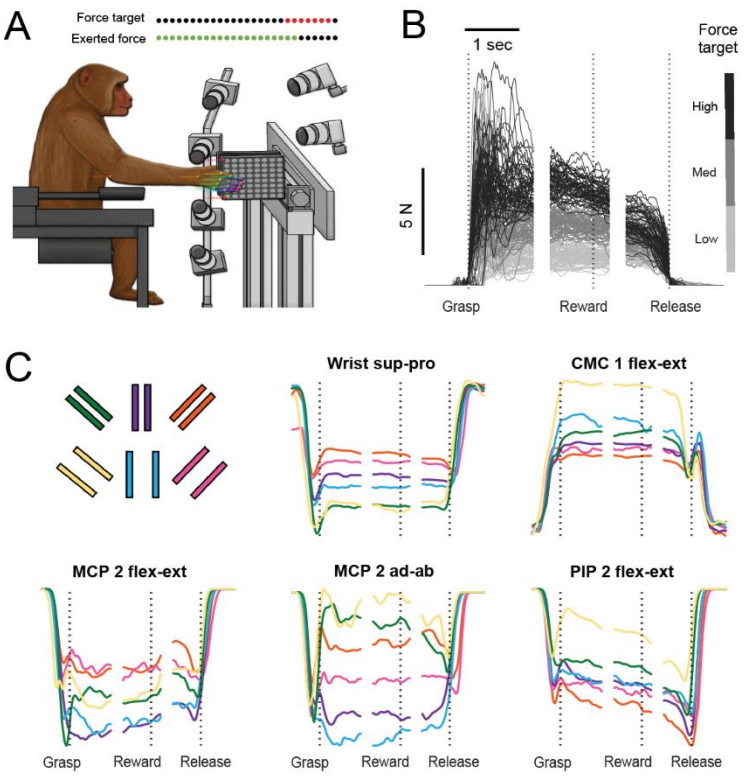

Figure 4.1 - (A) Task setup. Two monkeys were trained to reach for and grasp an object with instructed amount of force. Hand positions were tracked using 8 cameras. (B) Single trial force profiles color-coded by force target. (C) Five example joint angles inferred from the task, averaged within condition. The lines are color-coded according to the object (see top left inset for the legend).

for a specified duration (0.8-1 second). The object size took on one of three values (ranging from 5 to 20 mm, tailored to the monkey's hand), as did its orientation (ranging from -35 to +35º). Each object was grasped with one of three target forces (ranging from 2 to 10 N), and the animal received a water reward if it remained within 10-20% of the target force over the required hold duration. The monkeys completed a minimum of eight repetitions of each object-force condition.

The total contact force was computed from the sum of the output of the sensors on both sides of the object. Monkeys exerted a variety of force profiles for each target condition (Figure 4.1B). Hand kinematics – including the 28 joint angles – were reconstructed from the output of eight cameras placed around the workspace using computer vision (Figure 4.1C). Neural activity was

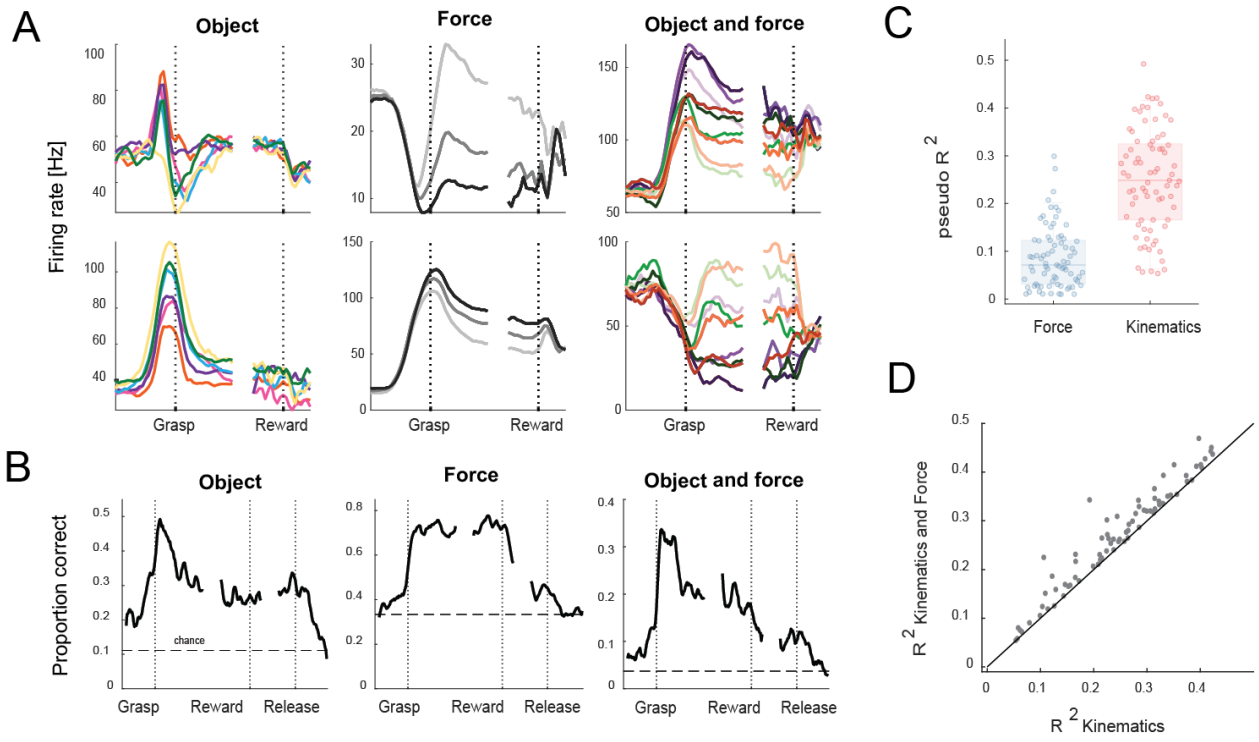

Figure 4.2 - Neural tunning. (A) Example PSTHs of recorded units in M1. Leftmost column: two units, tuned to object identity, color-coded using the same scheme as in Figure 4.1. (C). Middle column: two units, tuned to grasp force level, color-coded like Figure 4.1. (B). Rightmost column: two units tunned to both object and force. Here only three example objects are shown. Color intensity is proportional to target force. (B) Classification results as a function of time for object, force and both. Dashed lines show chance classification performance. (C) GLM results for models with only force inputs and only kinematic inputs. Each dot is a single neuron pseudo-R squared value. (D) By neuron comparison of GLM performance with only kinematic inputs vs kinematic and force inputs.

monitored with Utah electrode arrays (Blackrock Neurotech) in the hand and arm representation of M1.

4.3.2 Motor cortical neurons are tuned to object and force

First, we investigated the degree to which M1 units were modulated in a task-dependent way. We found that some neurons exhibited responses that were strongly dependent on object size and orientation (Figure 4.2A, left), suggesting that these were primarily encoding hand kinematics. Other neurons were strongly dependent on the target force and relatively insensitive to differences in the object (Figure 4.2A, middle). However, most neurons were modulated by both posture and force (Figure 4.2, right). To gauge object and force signals in the population response, we built classifiers of object identity and force level and found that classification performance was above chance, even before contact with the object was initiated (Figure 4.2B).

Having established that the M1 population response is dependent on task variables, we sought to estimate the relative strengths of the object and force signals. To this end, we used demixed principal component analysis (dPCA, Kobak, et al., 2016) to compute the amount of variance explained by object, force, and their interaction. We found that most neural variance (~80%) was condition independent, reflecting the structure of the reach that was common to all object and force conditions (Supplementary Figure 4.1). The object-dependent signal – presumably reflecting the object-specific grasp kinematics – was far weaker, accounting for 7.8% of the variance in the population response. The force-dependent signal was the weakest, capturing only 3.5% of the neural variance. Object-force interaction accounted for 5.8% of the variance which points to mixed coding for kinematics and force in the population (Supplementary Figure 4.1B). We conclude that M1 neurons are systematically modulated by the task, that most encode both the kinematics and forces, and that the force signal is weak at the single neuron and population levels.

4.3.3 Single neurons encode kinematics and force

Having established that M1 responses were modulated by task variables, we next investigated the relationship between time-varying kinematics and force and the responses of individual neurons. To this end, we trained generalized linear regression models to capture the responses of M1 neurons based on kinematic or force variables. We found that joint angles could account for neural responses better than force (mean R^2 = 0.1 vs. 0.25 for kinematics and force, respectively). Note, however, that there were 28 joint angles and only 1 force input so the kinematic models benefit from many more degrees of freedom. When restricting the dimensionality of the kinematics to one principal component (PC), the performance of the kinematic and kinetic models was statistically indistinguishable (Supplementary Figure 4.2). Next, we assessed whether the neural predictions were improved with both force and kinematics included in the GLM. We found that, for the majority of neurons, performance was slightly but significantly improved with the hybrid models (kinematics and force) (Figure 4.2D), relative to the kinematics-only models. We conclude that most M1 neurons encode a combination of force and kinematic variables.

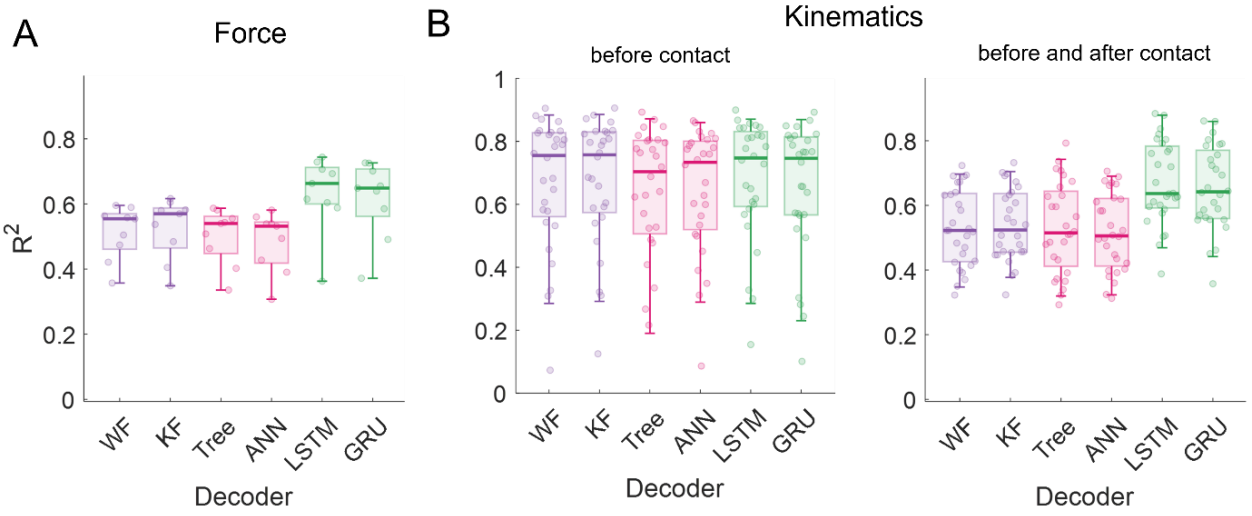

Figure 4.3 - Decoding kinematics and force. (A) Comparison of force decoder performance for the three class of models: linear (purple), static non-linear (pink) and recurrent non-linear (green). WF – Wiener Filter, KF – Kalman Filter, Tree – ensemble regression tree, ANN – feedforward neural network, GRU – gated recurrent unit network, LSTM – long short-term memory network. Each point is one session. Sessions are pooled from two monkeys. (B) Same decoding models for kinematics before contact (left) and throughout the entire trial (right). Each point is one kinematic degree of freedom.

4.3.4 Kinematics and force can be decoded from neural population responses

Examination of the mean population response and that of individual neurons suggests that the kinematics signal is strong in M1, while its force counterpart is weak. With this in mind, we gauged the degree to which we could decode the kinematics and force from the population response on individual trials using a decoding analysis. To this end, we implemented three classes of decoders of increasing complexity. The first was linear models (Wiener Filter or Kalman Filter, Figure 4.3, purple), which assume an instantaneous linear relationship between neural response and kinematics. The second class was non-linear decoders with static non-linearity (ANN - artificial neural network, or ensemble regression tree, Figure 4.3 pink), which assume an instantaneous relationship between neural response but can accommodate a non-linearity. The third class was non-linear decoders with recurrence (LSTM - long short-term memory model, or GRU – gated recurrent unit, Figure 4.3 green) that could exploit non-linear dynamics in the neural response.

Replicating previous studies, we found that even the simple linear decoder could accurately reconstruct kinematics before contact with the object was established and that the more complex decoders did not improve the reconstructions Figure 4.3B), consistent with previous findings on similar datasets (Glaser et al., 2020; E. V. Okorokova et al., 2020). However, when decoders were applied to the entire trial, before and after contact, the non-linear dynamic decoders (LSTM or GRU) outperformed all other decoders Figure 4.3B). In other words, while the relationship between kinematics and neuronal response is linear before contact, it becomes non-linear and dynamic after contact.

Next, we applied the same decoders to force. We found that linear decoder could capture coarse force fluctuations, but often failed to account for force adjustments throughout the hold period (Figure 4.3A, purple). Decoder performance did not improve with the addition of static

nonlinearity (ANN or Tree, Figure 4.3A, pink), suggesting that static non-linearity is not enough to explain force fluctuations. The second hypothesis was that force is linearly encoded in dynamical patterns of activity. To test this hypothesis, we implemented a linear decoder with a history term (Kalman Filter), which could thus exploit neural dynamics that were linearly related to force. We found that the decoding performance of the linear dynamic models was similar to static linear or static non-linear decoders. However, the decoders which can accommodate non-linear dynamics (LSTM, GRU) substantially outperformed all other decoders (Figure 4.3A, green). Our results are consistent with the hypothesis that force signals are encoded in non-linear dynamics in the motor cortex and can only be harnessed by decoders that can exploit those dynamics.

4.4 Discussion

This study aims to investigate the kinematic and force representations in the motor cortex using encoding and decoding modes. We find that motor neurons encode both kinematics and force and that the force-related signal is weaker than its kinematic counterpart. Furthermore, we observed that decoding continuous force requires models that can capture non-linear dynamics in the neural signal, such as recurrent neural networks.

4.4.1 Force representation in M1

Studies in non-human primates have shown that M1 responses are modulated by force (Evarts, 1968; Gardner et al., 2007; Georgopoulos et al., 1992; Hendrix et al., 2009; Hepp-Reymond et al., 1999; Intveld et al., 2018; Kalaska et al., 1989; Maier et al., 1993; Wannier et al., 1991). However, in these early studies, the response modulation by force was not systematically quantified nor was it disentangled from the modulation by kinematics. Later studies found that force signals in M1 are generally weak compared to their kinematic counterparts (Intveld et al., 2018; Rastogi et al., 2021). Consistent with these later studies, we found that force-related signals account for almost

three times less variance in the population response than do kinematic ones. The dominance of kinematic signals is surprising given that grasp force, which can reach 550 N in humans (Sobinov & Bensmaia, 2021), is associated with substantially greater muscle activations than hand movements (Zajac, 1989). One possibility is that force control is not mediated by the rostral region of M1, the target of the present study. Indeed, force signals are stronger in AIP and F5 than in M1 in the context of a similar task (Intveld et al., 2018). Another candidate for force control is caudal M1, which has a higher proportion of monosynaptic motor units (Rathelot & Strick, 2009) and thus more direct access to the muscles (Lemon, 2008). Nonetheless, the force signal in M1 is sufficiently robust to allow for decoding the intended force, as described below.

4.4.2 Force and kinematic interactions in M1

We found that M1 neurons encode hand posture, as evidenced by the fact that the inclusion of kinematic parameters in the Generalized Linear Model improves the neural prediction. In a small subset of neurons, the addition of force further improved the neural prediction. Thus, kinematic and force signals are intermixed in the responses of individual neurons, as might be expected to the extent that M1 neurons drive muscular activity, and muscular activity drives both kinematics and forces. At the population level, kinematic and force signals interact in M1, as evidenced by a significant object x force interaction term in the demixed principal components analysis (Supplementary Figure 4.1). The interaction term accounted for as much variance in the M1 activity as did the force main effect term, suggesting that the neural signature of force is strongly dependent upon posture. This dependence is unsurprising given that both kinematics and forces are mediated by muscular activity and the muscular activity to generate a given force is highly posture-dependent. The observed interaction between force and posture is consistent with previous findings (Hendrix et al., 2009; Intveld et al., 2018). Indeed, while the interaction term in these

previous studies accounted for little variance in the M1 response, so did the force main effect term, consistent with our findings (Intveld et al., 2018; Rastogi et al., 2021). We conclude that force and kinematic signals are carried by overlapping populations of M1 neurons. The interplay between kinematic and kinetic signals in M1 is also evinced by poor post-contact kinematic decoding. Indeed, decoders of posture built on data obtained before contact generalized poorly to post-contact and vice versa, as expected if kinematic and kinetic signals are intermixed.

4.4.3 The mapping between M1 response and force is dynamic

While kinematics can be linearly decoded from the M1 response (Carmena et al., 2003; Intveld et al., 2018; Rastogi et al., 2021), forces can not. Indeed, force signals in M1 peak around grasp onset, and then decay rapidly, with a second burst at grasp offset. The mapping between the M1 response and force is thus highly dynamic throughout the grasp and thus cannot be captured with a linear model. While non-linear models that assume a static non-linearity can account for the non-linear relationship between time-averaged M1 responses and force (Hepp-Reymond et al., 1999), these models cannot capture the dynamics in the relationship between response and force. We show that RNNs, which are capable of accommodating a dynamical mapping, can be used to accurately infer the intended force from the M1 response.

4.5 Future directions

Having investigated the neural basis of whole hand force, we will investigate the neural mechanisms that mediate individual digit forces. Indeed, we can command graded amounts of force for individual digits and combinations of digits. To examine the neural underpinnings of this ability, we will apply inverse dynamics to the data we have collected and characterize the relationship between M1 activity and the estimated joint torques. We anticipate that encoding models that take as input the joint torques, rather than whole hand forces, will provide far better

predictions of neuronal activity. To the extent that we can estimate joint torques in the absence of object contact (driven entirely by the mass of the joints), this representation of the hand may unify kinematics and force into a single, joint-based framework. Joint torques can be used as a proxy for muscle activations, which are indirectly driven by M1 activity. Ultimately, however, the objective of this line of work is to express hand kinematics and kinetics as patterns of muscular activity, which will further unify the different behavioral parameters and express these in terms of the effectors to which M1 has access.

4.6 Methods

4.6.1 Animals and surgery

Neural recordings were collected from two male rhesus macaques (ages 11 and 9 years at the time of surgery). They were each chronically implanted with a single Utah electrode array in the right primary motor cortex (Brodmann area 4, M1). The electrode lengths were 1.5mm, with uniform spacing of 400um aligned on a 10 by 10 grid. Arrays were placed in the arm and hand representation of the motor cortex, as confirmed by electrically stimulating the cortex during surgery with surface electrodes and observing corresponding twitches before array implantation. Surgical procedures consisted of the implantation of a head-fixing post onto the skull, craniotomy, intraoperative electrical stimulation of the brain surface, and implantation of the array. All procedures were performed under aseptic conditions and anesthesia induced with ketamine HCl (20 mg kg–1, IM) and maintained with isoflurane (10–25 mg kg–1 per hour, inhaled). Handling of animals was performed in accordance with the rules and regulations of the University of Chicago Animal Care and Use Committee. Monkeys received care from a full-time husbandry staff, and a full-time veterinary staff monitored the animals' health.

4.6.2 Experimental apparatus

We have designed an experimental apparatus that allows us to present to the animal "objects" that vary in size and orientation. Specifically, two parallel plates are mounted on motorized stages such that the distance between them can be varied systematically, thereby generating objects of varying sizes. Furthermore, the plates are mounted on a rotating platform such that the orientation of the plates can also be varied. Varying the separation between the plates and their orientation compels the animal to adopt different hand postures to grasp the object. Additionally, we instrumented the surface of the plates with dense sensor sheets (Tekscan, Boston, MA) that allow us to track the forces exerted on the object at each point of contact with high sensitivity (error < 5%) and temporal resolution (300 Hz). Two LED displays were mounted just above the object to indicate the target and current force levels exerted by the animal.

4.6.3 Behavioral task

We trained monkeys to perform a visually guided grasping task, in which they were required to grasp an object with a visually cued amount of force to achieve a reward. Each trial was initiated when an LED display came on to indicate the target force level to the animal. The animal then reached for the plates and, upon contact, another LED display tracked the total forces exerted on the plates in real-time. Monkeys received a juice reward when the target force was maintained for 0.8-1 consecutive seconds. Monkeys grasped up to 9 different objects with apertures ranging from 5 to 20 mm and rotations ranging from -35 to 35 degrees. Each object was grasped with one of three force targets that varied from 2 to 10N. Monkeys performed at least 8 repetitions of each object-force condition.

4.6.4 Forces

Grasp force was monitored continuously using two dense sensor sheets mounted on the outer surface of the "object". Each sensor sheet (Tekscan, Sensor 5101, Tekscan, Boston, MA) consists of 1,936 'sensels' arranged in a square grid of size $(111.8mm)^2$. We recorded force values from each 'sensel' on the two sensor sheets at 300Hz. We used total force, computed as a sum of all sensel values from both plates for continuous feedback to the monkey throughout the experiment. For offline analyses, we first denoised each sensel value by first subtracting its baseline activity (no touch condition). We then summed all 'sensel' values to get total force. Finally, we low-pass filtered the total force with 3^{rd} order Butterworth filter with a cutoff of 10Hz.

4.6.5 Kinematics

The grasping behavior of the animals was recorded using 8 synchronized cameras (FLIR BFS-U3-16S2C-CS) at 50 frames per second. We used a machine vision algorithm (DeepLabCut, (Mathis et al., 2018)) to automatically label a set of 34 body landmarks based on a set of manually labeled frames. We triangulated the two-dimensional positions of those landmarks to obtain their three-dimensional locations using the relative postures of the cameras. These 3D body markers together with a scaled skeletal model of the animal were used as an input to an inverse kinematics algorithm (SimTK OpenSim, Delp, et al., 2007) to obtain time-varying joint angles for 28 anatomical degrees of freedom. The code used for processing is available online (Greenspon & Sobinov, https://github.com/CMGreenspon/NCams).

4.6.6 Electrophysiology and neural data preprocessing

Neural data was collected with CerePlex Direct data acquisition system coupled with CerePlex E digital headstage (Blackrock Microsystems). For each channel, we bandpass filtered neural signals from 250Hz to 3kHz and extracted threshold crossing events at a -4.5 RMS value. We then used

offline spike sorting (Offline Sorter, Plexon, Dallas, TX) to remove non-spike threshold crossings and isolate individual units. Spikes were smoothed with a Gaussian filter with a standard deviation of 20ms unless otherwise specified.

4.6.7 Alignment and PSTHs

Since trial duration varied significantly, we used multiple alignment events when averaging data for illustration purposes. We used three alignment events labeled as 'grasp', 'reward', and 'release'. 'Grasp' and 'release' were defined based on the total force profile as the first and last time point when total force exceeded 0.5N, respectively. 'Reward' is the time point when the monkey received a juice reward for maintaining the force for the instructed amount of time.

For PSTH, we found trials that belong to the same group (force, object type, or object-force combination) and took median-smoothed neural responses around the three alignment events.

4.6.8 Classification

To assess whether there is information about object, force, or object-force in the neural responses, we used linear discriminant analysis (LDA) to classify object identity (9 conditions), force target (3 conditions), or object and force (27 conditions). We used a leave-one-out cross-validation procedure, in which for every trial, we trained a classifier on all other trials and tested it on the held-out trial. We used a sliding window of 100ms with a step of 20ms to assess classification performance (proportion of trials that we classified correctly) in time.

4.6.9 dPCA

Standard principal component analysis (PCA) is not very informative when it comes to understanding the influence of specific task parameters on neural variance, as individual units can exhibit mixed selectivity for different parameters. To separate the influence of each task parameter,

we implemented a methodology called demixed principal component analysis (dPCA)(Kobak et al., 2016), and found the components that explain the most variance within each task parameter, namely object and force target. dPCA also allows to find condition independent components that are consistent across all task conditions and an interaction component (force-object) that captures the interaction effect of force and object variations.

4.6.10 Generalized Linear Models

One of the main goals of the present study was to establish which aspects of prehensile behavior (kinematics or force) drove the responses of individual motor neurons. To this end, we used Generalized Linear Models (GLMs) with logarithmic non-linearity to predict the neuronal responses over the epochs of interest. We used an epoch from 500ms before object contact through 100ms after object release. Kinematics and forces were aligned with neural responses with a latency in the range of +-150ms that was optimized for each neuron. We fit three types of models: force, kinematic, and combined. We used a 5-fold cross-validation procedure and assessed the performance of our models using adjusted R^2 corrected for the number of inputs.

4.6.11 Decoding models

We used six models to decode continuous grasp force and kinematics, split into 3 general categories: linear, non-linear, and dynamic. We used two example models from each category to avoid conclusions based on the idiosyncratic behavior of a specific decoder. For linear methods we used Wiener filter and Kalman filter; for non-linear - regression tree ensemble (Tree) and Feedforward Artificial Neural Network (ANN); for dynamic - Gated Recurrent Unit (GRU) and Long Short-term Memory Network (LSTM).

Wiener filter was modeled as a linear regression, in which force signal is represented as a weighted sum of neural inputs. The coefficients of the model were inferred using Ordinary Least Squares

estimation. Kalman filter was fit similarly to that in Chapters 2 and 3 (E. V. Okorokova et al., 2020). The main difference between Wiener and Kalman filters is that the Kalman filter accounts for the dynamics in the modeled system (kinematics or force) by estimating an autoregressive model in addition to the neural regression model.

The regression tree ensemble involved boosting 100 regression trees using Least-squares boosting algorithm. ANN, GRU, and LSTM each contained up to 150 units arranged in one layer, followed by a dropout layer, and a regression layer. Hyperparameters, including the number of units, were optimized for each network to achieve the best cross-validation fit. Prior to fitting the networks, inputs and outputs were range normalized.

We used a 5-fold cross-validation procedure in which we split the observation data pseudo-randomly (keeping the number of trials in each condition balanced) into five testing sets. For each

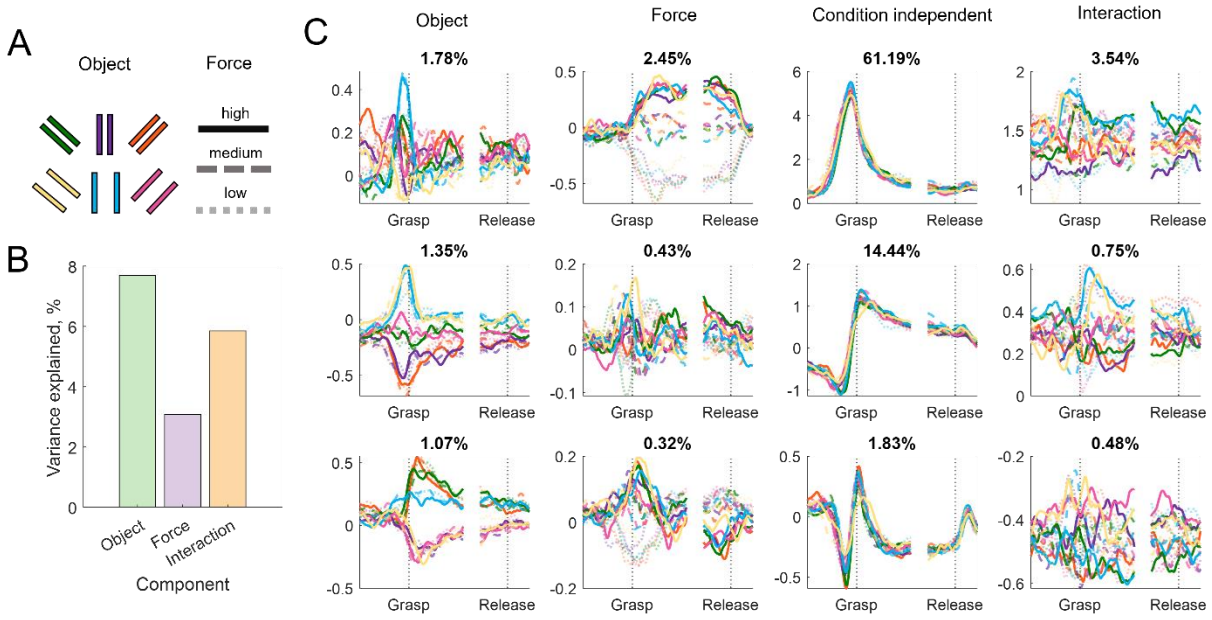

Supplementary Figure 4.1 - Demixed principal component analysis. A. color code for objects and force levels for C. B. Fraction of variance explained by object, force and object-force interaction. C. Time varying components for force, object, condition independent, and object-force interaction projections, color-coded by object shape. The shading of the lines indicated target force level.

test set, we trained the model on the remaining data 80% of the data. We used the coefficient of determination (R^2) and root mean squared error (RMSE) to assess decoder performance.

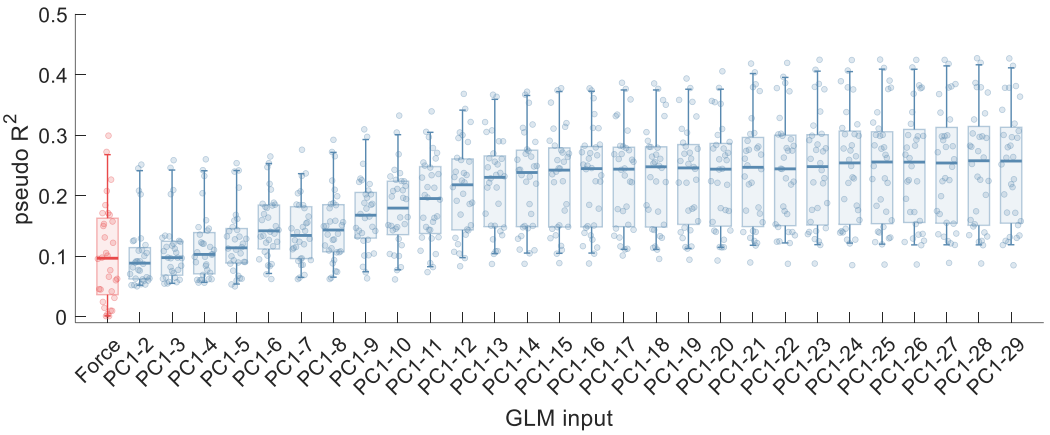

Supplementary Figure 4.2 – Performance of GLM models fit with either force (red) or kinematic PCs (from 1st to Nth). Each point is one neuron.

4.7 References

Carmena, J. M., Lebedev, M. A., Crist, R. E., O'Doherty, J. E., Santucci, D. M., Dimitrov, D. F., Patil, P. G., Henriquez, C. S., & Nicolelis, M. A. L. (2003). Learning to Control a Brain–Machine Interface for Reaching and Grasping by Primates. *PLOS Biology*, *1*(2), e42. https://doi.org/10.1371/journal.pbio.0000042

Delp, S. L., Anderson, F. C., Arnold, A. S., Loan, P., Habib, A., John, C. T., Guendelman, E., & Thelen, D. G. (2007). OpenSim: Open-source software to create and analyze dynamic simulations of movement. *IEEE Transactions on Bio-Medical Engineering*, *54*(11), 1940–1950. https://doi.org/10.1109/TBME.2007.901024

Downey, J. E., Weiss, J. M., Flesher, S. N., Thumser, Z. C., Marasco, P. D., Boninger, M. L., Gaunt, R. A., & Collinger, J. L. (2018). Implicit Grasp Force Representation in Human Motor Cortical Recordings. *Frontiers in Neuroscience*, *12*. https://www.frontiersin.org/articles/10.3389/fnins.2018.00801

Evarts, E. V. (1968). Relation of pyramidal tract activity to force exerted during voluntary movement. *Journal of Neurophysiology*, *31*(1), 14–27. https://doi.org/10.1152/jn.1968.31.1.14

Gardner, E. P., Ro, J. Y., Babu, K. S., & Ghosh, S. (2007). Neurophysiology of Prehension. II. Response Diversity in Primary Somatosensory (S-I) and Motor (M-I) Cortices. *Journal of Neurophysiology*, *97*(2), 1656–1670. https://doi.org/10.1152/jn.01031.2006

Georgopoulos, A. P., Ashe, J., Smyrnis, N., & Taira, M. (1992). The Motor Cortex and the Coding of Force. *Science*, *256*(5064), 1692–1695. https://doi.org/10.1126/science.256.5064.1692

Glaser, J. I., Benjamin, A. S., Chowdhury, R. H., Perich, M. G., Miller, L. E., & Kording, K. P. (2020). *Machine learning for neural decoding* (arXiv:1708.00909). arXiv. https://doi.org/10.48550/arXiv.1708.00909

Goodman, J. M., Tabot, G. A., Lee, A. S., Suresh, A. K., Rajan, A. T., Hatsopoulos, N. G., & Bensmaia, S. (2019). Postural Representations of the Hand in the Primate Sensorimotor Cortex. *Neuron*, *104*(5), 1000-1009.e7. https://doi.org/10.1016/j.neuron.2019.09.004

Greenspon, C. M., & Sobinov, A. R. (n.d.). *NCams*. https://github.com/CMGreenspon/NCams

Hendrix, C. M., Mason, C. R., & Ebner, T. J. (2009). Signaling of Grasp Dimension and Grasp Force in Dorsal Premotor Cortex and Primary Motor Cortex Neurons During Reach to Grasp in the Monkey. *Journal of Neurophysiology*, *102*(1), 132–145. https://doi.org/10.1152/jn.00016.2009

Hepp-Reymond, M.-C., Kirkpatrick-Tanner, M., Gabernet, L., Qi, H.-X., & Weber, B. (1999). Context-dependent force coding in motor and premotor cortical areas. *Experimental Brain Research*, *128*(1), 123–133. https://doi.org/10.1007/s002210050827

Intveld, R. W., Dann, B., Michaels, J. A., & Scherberger, H. (2018). Neural coding of intended and executed grasp force in macaque areas AIP, F5, and M1. *Scientific Reports*, *8*(1), Article 1. https://doi.org/10.1038/s41598-018-35488-z

Isa, T. (2019). Dexterous Hand Movements and Their Recovery After Central Nervous System Injury. *Annual Review of Neuroscience*, *42*(1), 315–335. https://doi.org/10.1146/annurev-neuro-070918-050436

Kalaska, J. F., Cohen, D. A., Hyde, M. L., & Prud'homme, M. (1989). A comparison of movement direction-related versus load direction-related activity in primate motor cortex, using a two-dimensional reaching task. *The Journal of Neuroscience: The Official Journal of the Society for Neuroscience*, *9*(6), 2080–2102. https://doi.org/10.1523/JNEUROSCI.09-06-02080.1989

Kobak, D., Brendel, W., Constantinidis, C., Feierstein, C. E., Kepecs, A., Mainen, Z. F., Qi, X.-L., Romo, R., Uchida, N., & Machens, C. K. (2016). Demixed principal component analysis of neural population data. *ELife*, *5*, e10989. https://doi.org/10.7554/eLife.10989

Lemon, R. N. (2008). Descending pathways in motor control. *Annual Review of Neuroscience*, *31*, 195–218. https://doi.org/10.1146/annurev.neuro.31.060407.125547

Maier, M. A., Bennett, K. M., Hepp-Reymond, M. C., & Lemon, R. N. (1993). Contribution of the monkey corticomotoneuronal system to the control of force in precision grip. *Journal of Neurophysiology*, *69*(3), 772–785. https://doi.org/10.1152/jn.1993.69.3.772

Mathis, A., Mamidanna, P., Cury, K. M., Abe, T., Murthy, V. N., Mathis, M. W., & Bethge, M. (2018). DeepLabCut: Markerless pose estimation of user-defined body parts with deep learning. *Nature Neuroscience*, *21*(9), 1281–1289. https://doi.org/10.1038/s41593-018-0209-y

Menz, V. K., Schaffelhofer, S., & Scherberger, H. (2015). Representation of continuous hand and arm movements in macaque areas M1, F5, and AIP: A comparative decoding study. *Journal of Neural Engineering*, *12*(5), 056016. https://doi.org/10.1088/1741-2560/12/5/056016

Okorokova, E. V., Goodman, J. M., Hatsopoulos, N. G., & Bensmaia, S. J. (2020). Decoding hand kinematics from population responses in sensorimotor cortex during grasping. *Journal of Neural Engineering*, *17*(4), 046035. https://doi.org/10.1088/1741-2552/ab95ea

Paninski, L., Fellows, M. R., Hatsopoulos, N. G., & Donoghue, J. P. (2004). Spatiotemporal Tuning of Motor Cortical Neurons for Hand Position and Velocity. *Journal of Neurophysiology*, *91*(1), 515–532. https://doi.org/10.1152/jn.00587.2002

Rastogi, A., Willett, F. R., Abreu, J., Crowder, D. C., Murphy, B. A., Memberg, W. D., Vargas-Irwin, C. E., Miller, J. P., Sweet, J., Walter, B. L., Rezaii, P. G., Stavisky, S. D., Hochberg, L. R., Shenoy, K. V., Henderson, J. M., Kirsch, R. F., & Ajiboye, A. B. (2021). The Neural Representation of Force across Grasp Types in Motor Cortex of Humans with Tetraplegia. *ENeuro*, *8*(1), ENEURO.0231-20.2020. https://doi.org/10.1523/ENEURO.0231-20.2020

Rathelot, J.-A., & Strick, P. L. (2009). Subdivisions of primary motor cortex based on cortico-motoneuronal cells. *Proceedings of the National Academy of Sciences*, *106*(3), 918–923. https://doi.org/10.1073/pnas.0808362106

Rouiller, E. m., Yu, X. h., Moret, V., Tempini, A., Wiesendanger, M., & Liang, F. (1998). Dexterity in adult monkeys following early lesion of the motor cortical hand area: The role of cortex adjacent to the lesion. *European Journal of Neuroscience*, *10*(2), 729–740. https://doi.org/10.1046/j.1460-9568.1998.00075.x

Schaffelhofer, S., & Scherberger, H. (2012). A new method of accurate hand- and arm-tracking for small primates. *Journal of Neural Engineering*, *9*(2), 026025. https://doi.org/10.1088/1741-2560/9/2/026025

Sobinov, A. R., & Bensmaia, S. J. (2021). The neural mechanisms of manual dexterity. *Nature Reviews. Neuroscience*, *22*(12), 741–757. https://doi.org/10.1038/s41583-021-00528-7

Wannier, T. M., Maier, M. A., & Hepp-Reymond, M. C. (1991). Contrasting properties of monkey somatosensory and motor cortex neurons activated during the control of force in precision grip. *Journal of Neurophysiology*, *65*(3), 572–589. https://doi.org/10.1152/jn.1991.65.3.572

Zajac, F. E. (1989). Muscle and tendon: Properties, models, scaling, and application to biomechanics and motor control. *Critical Reviews in Biomedical Engineering*, *17*(4), 359–411.

Chapter 5 | Grasp force decoding for brain-computer interfaces

5.1 Abstract

Intracortical brain-computer interfaces (iBCIs) have achieved remarkable progress in restoring arm and hand movement by inferring motor intent from neural signals in the primary motor cortex (M1) and realizing the intended movements in a bionic limb. However, the majority of the work has focused on limb kinematics, enabling users to adopt desired limb postures. However, manual interactions with objects require the precise application of forces, which implies a different mode of limb control that has been largely overlooked. One of the major obstacles to incorporating force control is the lack of understanding of how manual forces are encoded in M1. To fill this gap, we recorded M1 activity from three individuals with tetraplegia using chronically implanted Utah electrode arrays as they attempted to grasp virtual objects with varying force. We found that information about force in the motor cortex is weak but significant and most prominent around the onset of grasp. With this in mind, we developed real-time continuous decoders that harness force signals in M1 to enable the virtual hand to exert force. We demonstrated that recurrent neural networks, which can exploit the non-linear dynamics of the M1 response, significantly outperform standard linear or non-linear decoders. Our findings pave the way for the development of brain-controlled bionic hands that can not only precisely shape the hand but also allow for well-controlled force application.

5.2 Introduction

Intracortical brain-computer interfaces (iBCI) show great promise for restoring hand function in patients with tetraplegia through the use of bionic hands (Ajiboye et al., 2017; Blabe et al., 2015; Collinger et al., 2013; Hochberg et al., 2012b; Wodlinger et al., 2014). However, current approaches to restoring hand and arm function are restricted to kinematic control, enabling users

to control the position or speed of the arm and hand (Collinger et al., 2013; Hochberg et al., 2012b; Wodlinger et al., 2014). However, manual interactions with objects require the ability to modulate the forces exerted on them, a capability that kinematic decoders cannot support (Downey et al., 2018; Rastogi et al., 2021). A major challenge in incorporating force control into brain-controlled bionic hands has been that the neural basis of this control mode is poorly understood. Indeed, while M1 activity related to force has been identified in studies with non-human primates (Evarts, 1968; Gardner et al., 2007; Georgopoulos et al., 1992; Hendrix et al., 2009; Hepp-Reymond et al., 1999; Intveld et al., 2018; Kalaska et al., 1989; Maier et al., 1993; Wannier et al., 1991) and humans (Branco, de Boer, et al., 2019; Branco, Geukes, et al., 2019; Downey et al., 2018; Rastogi et al., 2021), the relationship between neuronal activity and force is poorly understood. Accordingly, harnessing these signals to decode grasp force in a BCI setting has proven challenging. To date, M1 signals were used to decode one or a few discrete force levels (Carmena et al., 2003; Dekleva et al., 2021; Downey et al., 2018; Rastogi et al., 2021), excluding the online control of graded forces, critical for achieving seamless object manipulation.

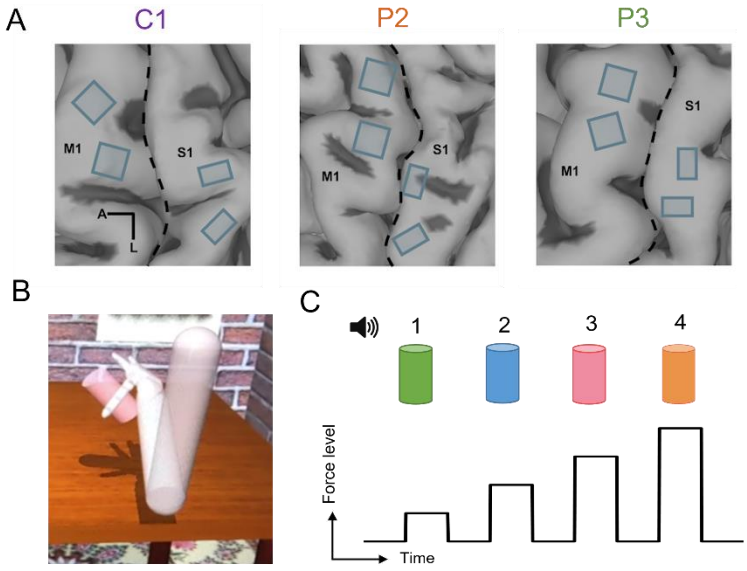

Figure 5.1 – (A) Array placement in participants C1, P2 and P3. M1 – arrays in motor cortex, S1 – arrays in somatosensory cortex. (B) Mujoco virtual environment. The participant controlled their avatar limb that grasped a virtual cylindrical object. (C) Example of force command sequence with 4 force levels. Force target was indicated by a verbal cue and a color of an object.

To fill this gap, we recorded M1 activity in 3 individuals with tetraplegia while they performed a grasp force task in a virtual environment. We found that signals in M1 carry information about the target force level, particularly just before the onset

of grasp. We then implemented various continuous decoders of force and found that only those that harnessed nonlinear dynamics in the M1 population response could achieve seamless force control. These results pave the way for improved intracortical brain-computer interfaces that enable users to not only control hand posture but also manual interaction forces.

5.3 Results

5.3.1 iBCI grasp force task

The study involved three human participants (C1, P1, and P2) whose hands were paralyzed as a result of a spinal cord injury. Each participant was implanted with two Utah electrode arrays (Blackrock Neurotech) in the hand representation of the motor cortex (M1). The participants controlled a limb avatar in a physics engine platform (Mujoco, Figure 3A), which they experienced through a virtual reality headset (Valve Index). They used the virtual limb to grasp virtual objects at different force levels (varying from 2 to 8 depending on the session and participant), cued by the color of the object and verbal instruction (Figure 3B). Initially, virtual limb movements and force feedback were under computer control and participants observed and attempted to perform the actions of the virtual limb. The neural activity during this observation phase was used to construct decoders of hand closing velocity and grasp force. The participants then performed the task in virtual reality under full brain control.

5.3.2 Motor cortex contains weak but significant force signal

First, we assessed the degree to which M1 signals in the human motor cortex were modulated by the task. To this end, we compared each neuron's firing rate before and after cue onset, at which time responses often increased. We found that 55, 36, and 35% of recorded channels were significantly modulated by the task for subjects C1, P2, and P3, respectively (Wilcoxon sign rank test, $p<0.01$). Most M1 channels exhibited a strong transient at the onset of grasp (Figure 5.1A,

left plot) and a weaker transient upon object release. A few channels were also visibly modulated by force, exhibiting either increases (Figure 5.1A middle plot) or decreases in response at higher forces (Figure 5.1A right plot). Out of all the M1 channels that were modulated by the task, 45,

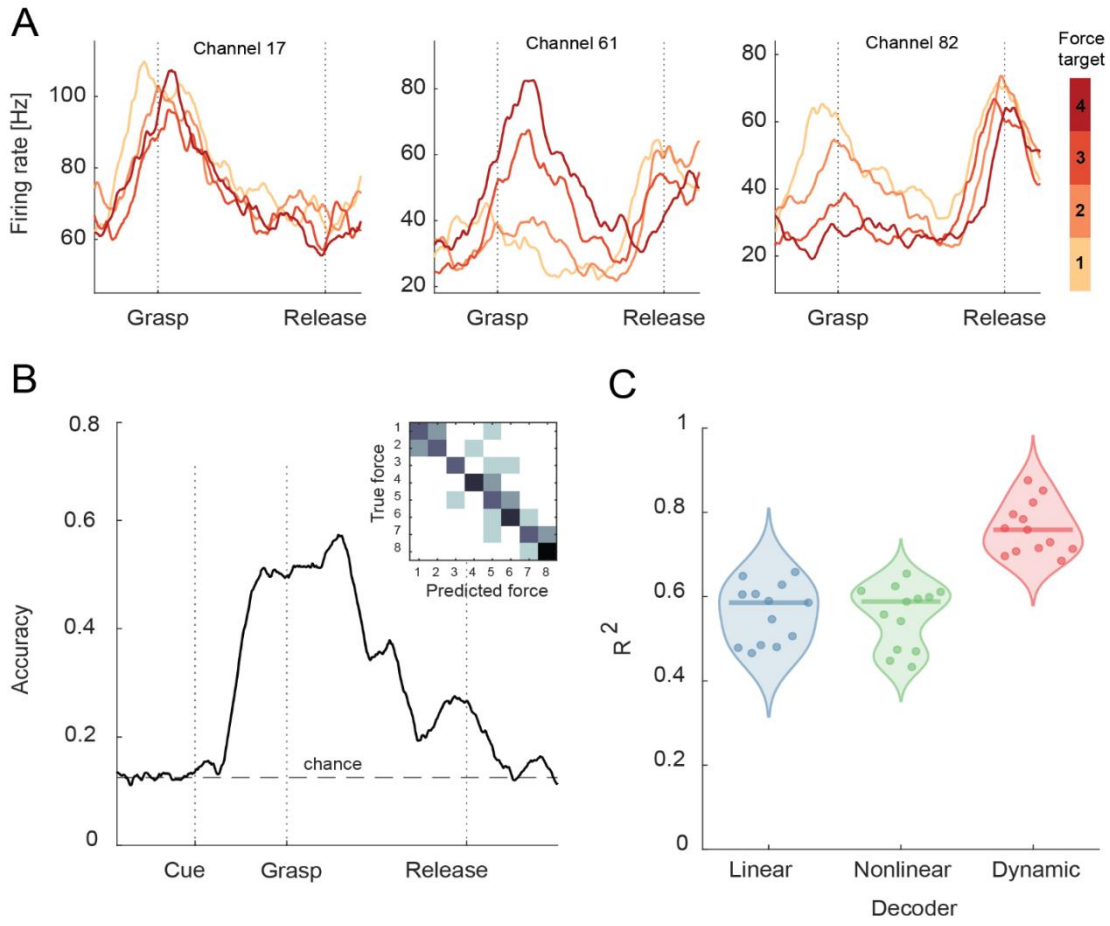

Figure 5.2 - (A) Mean response profiles (peristimulus time histograms) to 4 levels of grasp force on three motor channels from participant C1. Different colors denote different force levels. The responses are aligned to contact (of the virtual hand with the object). (B) Classification accuracy as a function of time for 8 levels of grasp force. Inset: confusion matrix for the 8 decoded force levels at onset of grasp. (C) Coefficient of determination for three types of decoders of continuous force: linear, non-linear, and dynamic. Points represent sessions pooled from all three subjects. Horizontal lines show median performance level across all sessions.

33, and 24% produced responses that were significantly modulated by force for participants C1, P2, and P3, respectively (ANOVA, $p < 0.01$). Thus, force signals are weak in human M1, as is the case in monkeys.

5.3.3 Most information about force is contained around grasp onset

Next, we examined the time course over which the force signal evolves in M1. To this end, we tested whether we could classify force level, using a linear discriminant analysis, based on responses of all recorded channels over a 100-ms window slid over the entire trial. We found classification performance improved beyond chance soon after cue onset, then began to decline, dropping back to chance shortly after object release (Figure 5.2B, Supplementary Figure 5.1). Overall classification performance was relatively poor, even at its peak, reflecting the weakness of the force-related signal in M1. More importantly, force information was unstable, exhibiting a phasic peak near grasp onset, then decreasing substantially over the hold period.

5.3.4 Dynamic non-linear decoders can capture continuous force fluctuations

Having established that the force signal was largely phasic and decreased throughout each trial, we gauged the degree to which force could be decoded continuously from M1 responses. We tested three types of decoders: standard linear decoder often used for real-time prosthetic control (Wiener filter), non-linear decoder with static non-linearity (feedforward artificial neural network), and dynamic decoder with built-in non-linear temporal dependence (recurrent neural network with long short-term memory layers) (see Methods). We found that for all subjects and sessions, the dynamic decoder significantly outperformed both linear and non-linear methods (Figure 5.2D), suggesting that there is a non-linear dynamic relationship between target force and neural responses in motor cortex, consistent with the observed instability of the force signal observed in the classification analysis.

5.3.5 Dynamic decoder allows accurate force decoding online

While the dynamic decoder outperforms other decoders offline, good offline performance does not always translate into improved online performance (Glaser et al., 2020; Pandarinath & Bensmaia,

2022). With this in mind, we assessed the participants' ability to perform the force task with our dynamic decoder. As in the offline case, the participants were cued to exert one of several levels of force – ranging from 2 to 8, depending on the session – on the virtual object. Both the hand closure and the level of force were decoded from M1 signals with a dynamic decoder, trained on the observation data as described above. We found that the decoder enabled outstanding performance on the task, yielding a performance of 88, 75, and 81% correct for participants C1, P2, and P3, respectively. In addition, we trained three decoders – linear, non-linear, and dynamic – in a single session and had participant C1 perform the force task with each decoder in separate experimental blocks. We found that the dynamic decoder yielded consistently better accuracy than the other two decoders, as was found with offline decoding (Figure 5.3). We further challenged the decoders with a more complex task, which required adjusting the force three times throughout each trial: once upon initial contact, and then twice more after that (Supplementary Figure 5.2A). Force levels were, again, cued on a computer monitor. The participant performed the online task either with a standard linear decoder or with the dynamic

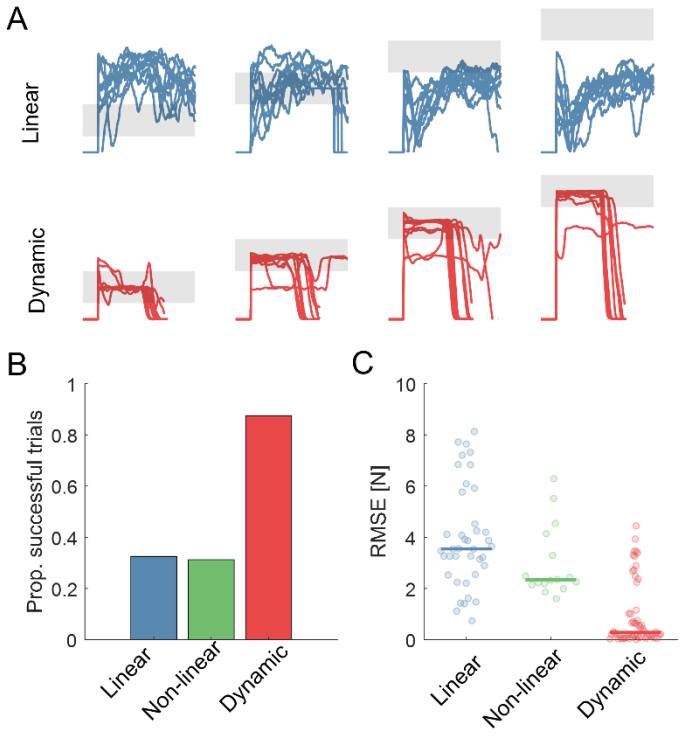

Figure 5.3 – (A) Example reconstructed force traces with Linear (top, blue) and Dynamic (bottom, red) decoders. Shaded grey areas indicate target force interval. Several trials are superimposed and aligned to first contact. (B) Proportion of successful trials performed by subject C1 using Linear, Non-linear or Dynamic decoders online. (C) Online decoding RMSE for the three decoders in subject C1. Each point is a trial. Horizontal bar is median RMSE across all trials.

decoder (each trained on the standard observation task). We found that the task could not be accomplished with the linear decoder (0%), but the dynamic decoder yielded a mean performance of 68.8% (Supplementary Figure 5.2B). Thus, a recurrent neural network is well suited to extract force signals from the M1 population response, presumably because it can accommodate the dynamic representation of force in M1, while the other decoder types cannot.

5.4 Discussion

We find that M1 activity carries information about attempted force, in three tetraplegic subjects. Accordingly, force cannot be reliably decoded from M1 activity using standard linear and non-linear decoders. However, decoders that can exploit non-linear dynamics can be used to reconstruct forces offline and to continuously infer intended force online.

5.4.1 Force signals in the human motor cortex are weak

As mentioned in the previous chapter, studies with non-human primates have demonstrated that M1 responses are influenced by force, albeit to a lesser degree than by kinematics (Evarts, 1968; Gardner et al., 2007; Georgopoulos et al., 1992; Hendrix et al., 2009; Hepp-Reymond et al., 1999; Intveld et al., 2018; Kalaska et al., 1989; Maier et al., 1993; Wannier et al., 1991; Intveld et al., 2018). The same phenomenon has been observed in previous studies in humans with tetraplegia during attempted grasp. In these studies, participants were instructed to attempt to grasp a virtual object with different levels of force (Downey et al., 2018; Rastogi et al., 2021). M1 neurons were only weakly modulated by force: the strongest force signal occurred around object contact and declined rapidly thereafter. The force condition could be inferred from the M1 response using a linear classifier but performance was far from perfect (below 80%) despite the small number of conditions.

Our classification results generally match previous ones with more grasp force levels (up to 8). Indeed, the force signal was poor, peaking at the onset of the grasp (Figure 5.2A, B)(cf. Dekleva et al., 2021), and supported poor force classification performance using linear classifiers. We extended these previous findings by building and testing continuous decoders of grasp force, which is challenging (Dekleva et al., 2021; Downey et al., 2018). While the standard linear and non-linear decoders yielded poor force decoding, a recurrent neural network was able to accurately recover the force information despite the underlying instability of the force signals in M1. We hypothesize that force information is encoded in dynamical patterns of M1 activity, more so than its kinematics counterpart (Carmena et al., 2003; Glaser et al., 2020; E. V. Okorokova et al., 2020), consistent with our results in monkeys (see Chapter 4). In one study, continuous decoder of force tracked the time course of the force exertion (Carmena et al., 2003). In this experiment, the monkeys were exerting force at regular intervals, and the linear decoder was able to capture this periodicity. However, the decoder failed to match the measured force level, as did our linear force decoders (Figure 5.3A, blue trace). Our dynamic decoder is thus the first continuous decoder of force that can accommodate different levels of force.

5.4.2 Dynamic non-linearity in neural responses

Previous studies report non-linearities between M1 responses and grasp force (Hepp-Reymond et al., 1999). To investigate this systematically, we implemented non-linear decoders with static or dynamic non-linearities. We found that decoders with static non-linearities did not provide a reliable mapping between the M1 population response and time-varying force. On the other hand, a decoder that incorporated a dynamic non-linearity, which could then accommodate dynamic non-linearities in the force signal, was able to capture grasp force reliably both offline and online.

One potential explanation for the success of the dynamic decoder is that it acted as a classifier, extracting information about intended force from the transient at the onset of grasp, when this information is most prominent, and then maintaining the level of force until it detected a release signal. The smoothness and stability of the reconstructed traces in the grasp and hold task are consistent with this hypothesis (Figure 5.3A, red). Two observations argue against this view. First, the dynamic decoder achieved equally good performance with an increased number of force targets (up to 8), a close approximation to a continuous task. Second, the decoder was able to accommodate a modified version of the task, in which the participant (C1) adjusted grasp force twice throughout the trial. Indeed, the dynamic decoder enabled these adjustments even when it was only trained on the simple grasp task, without adjustments (Supplementary Figure 5.2).

5.4.3 Limitations

There is increasing evidence for context-dependent coding in motor cortex, including encoding of force (Dekleva et al., 2023; Hepp-Reymond et al., 1999; Shelchkova et al., 2022). While recurrent neural networks excel at learning dependencies in the observed data, they often fail to generalize to new patterns of activity (Deo et al., 2023). Therefore, our approach might not be suited for more complex tasks, for example, grasp and transfer of objects, or force control of individual digits.

Another aspect of grasp force that has not been investigated in the current study is the contribution of tactile feedback associated with producing varying amounts of force on the grasped objects. Indeed, without tactile feedback proper object manipulation and grasp force control is challenging. Incorporation of tactile feedback in BCI control is currently possible via intracortical microstimulation (ICMS) of somatosensory cortex (S1)(Bensmaia & Miller, 2014; Flesher et al., 2016). While ICMS has shown to be functionally effective in some motor tasks (Flesher et al., 2021), it was also shown to alter motor cortical activity through intracortical connections between

S1 and M1, which could significantly affect decoder performance (Shelchkova et al., 2022). Whether our dynamic decoders could work efficiently with perceived tactile sensations and ICMS-induced perturbations remains to be tested.

5.5 Methods

5.5.1 Participants

The study involved three participants who provided informed consent as part of a multi-site clinical trial (NCT01894802). Participant C1 was a 57-year-old male at the time of the implant who had a C4-level ASIA D spinal cord injury (SCI) 35 years prior. He had no control over the intrinsic or extrinsic muscles of his right hand but could move his arm with some weakness in upper limb muscles. Participant P2 was a 28-year-old male with a C5 motor/C6 sensory ASIA B SCI that occurred 10 years prior. He had no control over the intrinsic or extrinsic muscles of his right hand but had limited control of wrist flexion and extension. Proximal limb control at the shoulder was intact, as was elbow flexion, but he could not voluntarily extend his elbow. Participant P3 was also a 28-year-old male with a C6 ASIA B SCI that occurred 12 years prior. He had no functional control of the intrinsic or extrinsic muscles of his right hand but could move his arm with weakness in upper limb muscles.

5.5.2 Array implantation

We surgically implanted four Neuroport microelectrode arrays (Blackrock Neurotech, Salt Lake City, UT, USA) in the left hemisphere of each participant. In somatosensory cortex (S1), two arrays, measuring 2.4 mm x 4 mm, each had sixty 1.5-mm electrode shanks wired in a checkerboard pattern, allowing for 32 electrodes to be stimulated. In motor cortex (M1), the other two arrays measured 4 mm x 4 mm and had one hundred 1.5-mm electrode shanks, with 96 (participants C1 and P3) or 88 (participant P2) wired (active), and four inactive shanks located at

the corners of all arrays (with an additional 8 for participant P2). In participant P2, the motor cortex arrays were metalized with platinum, while the somatosensory arrays were coated in sputtered iridium oxide. In participants C1 and P3, all electrodes were coated with sputtered iridium oxide. Each participant had two percutaneous connectors placed on their skull, with each connected to one sensory and one motor array. We used functional neuroimaging of the participants attempting to make movements of the hand and arm, and imagining feeling sensations on their fingertips during surgery, to target array placement within the constraints of anatomical features such as blood vessels and cortical topography. Array locations, shown in Figure 5.1A on structural MRI models of each participant's brain, were confirmed using intraoperative photographs after insertion.

5.5.3 Neural recordings

Only data from M1 arrays were analyzed in this study. Neural signals were recorded at 30 kHz using the NeuroPort system (Blackrock Neurotech, Salt Lake City, UT, USA). The data were high-pass filtered with a 3rd order Butterworth filter above 350Hz. Whenever the signal crossed a threshold (-4.25 RMS, set at the start of each recording session), a spiking event was recorded, and a snippet of the waveform was saved. Spikes were binned in 20-ms bins for offline analyses and decoding. Only channels with firing rate above 0.5Hz were used.

5.5.4 Virtual environment task

We used a physics engine platform (Mujoco, DeepMind Technologies, London, UK) to simulate a virtual environment with an avatar hand and a rigid cylindrical object. The participants observed a virtual room through a VR headset (Valve Index). Each trial began with the hand in a neutral open position next to a gray-colored cylindrical object. A verbal command was given to the participants indicating a number from 1 to K (maximum number of force levels for a particular

session), which corresponded to a specific amount of force to be applied when grasping the object. The color of the object changed based on the given target force. Participants then attempted to grasp the object with the instructed amount of force as they observed the virtual hand closing around the object. They were required to maintain contact with the object for a variable amount of time, ranging from 0.5 to 2 seconds, before releasing it upon another verbal command. Force targets were randomized. The number of target force levels (K) differed for the three participants. Subject C1 underwent five sessions with three force levels, four sessions with four levels, and one session with eight levels. Subject P2 had one session with two levels and another with four levels, while subject P3 had one session with two levels.

The experiment was conducted in two stages: observation (O) and full brain control (FBC). During the observation stage, the physics engine controlled the movement of the hand and the force exerted on the object. Participants were required to attempt the task as they watched it being performed. In the control stage, an online decoder, trained on data collected during the observation stage, was employed to direct the hand's movement and the force applied to the object. In each session, participants performed 40-80 trials of observation, followed by 20-60 trials of full-brain control.

5.5.5 Data alignment and neural modulation

Spikes in each motor channel were binned in 20ms bins and smoothed with a 100ms moving average filter. We evaluated task modulation in each channel by computing a paired sample Wilcoxon signed rank test on the mean neural responses 2 seconds prior to cue presentation and 4 seconds after cue presentation. We assumed the channel was task modulated if p-value of the test was below 0.01. For all task-modulated channels we also selected force-modulated channels using

ANOVA grouped by target force. Channels with a p-value below 0.01 were deemed force-dependent.

For peristimulus time histogram (PSTH) plots, the binned spikes from each trial of observation dataset were aligned to force target cue and then averaged for each grasp condition, resulting in four time-varying signals, representing each force level.

5.5.6 Classification

To assess whether there is information about force in the neural responses, we used linear discriminant analysis (LDA) to classify force target (2-8 conditions, depending on the subject and session). We used a leave-one-out cross-validation procedure, in which for every trial, we trained a classifier on all other trials and tested it on the held-out trial. We used a sliding window of 100ms with a step of 20ms to assess classification performance (proportion of trials that we classified correctly) in time.

5.5.7 Offline force decoding

We used three models to decode continuous grasp force offline: linear regression (referred to as Linear model), feedforward artificial neural network (Non-linear model), and recurrent neural network (Dynamic model). All decoders were restricted to be causal to accommodate the online regime, in which we only used neural data no later than 20ms prior to the current time stamp, and Gaussian spike filter was replaced with exponential smoothing.

Linear model assumes that a force signal can be represented as a weighted sum of neural inputs. The coefficients of the model were inferred using Ordinary least squares estimation. The non-linear model was constructed as a feedforward neural network with one fully connected layer of

150 units. The dynamic model consisted of a layer of 150 LSTM nodes. Hyperparameters of both networks were optimized to achieve the best cross-validation fit.

We used a 5-fold cross-validation procedure in which we split the observation data pseudo-randomly (keeping the number of trials in each condition balanced) into five testing sets. For each test set, we trained the model on the remaining data 80% of the data. We used the coefficient of determination (R^2) and root mean squared error (RMSE) to assess decoder performance.

5.5.8 Online force decoding

We implemented Linear, Non-linear, and Dynamic decoders online in subject C1 and Dynamic decoders only in subjects P2 and P3. For each session, we first collected observation data, then trained the decoders. Finally, we applied the trained decoders to infer grasp force with incoming neural signals. If multiple decoders were tested, we used the same observation data to train them, and tested them online in random order, keeping the subject blinded to the type of decoder he was using. The trial was considered successful if the subject could maintain grasp force within the target zone for 1 second. No visual, auditory, or tactile feedback was given to the subject.

A control adjustable force experiment was conducted only in subject C1. For this experiment, the subject was required to adjust grasp force twice during the hold period. The sequence of grasp targets consisted of 4 possible force levels chosen randomly for each trial. The trial was deemed successful if the subject could maintain the force at all three targets for 0.5sec each without

dropping the object. Offline training time was under 5 minutes for all decoders. Real-time inference was under 10ms.

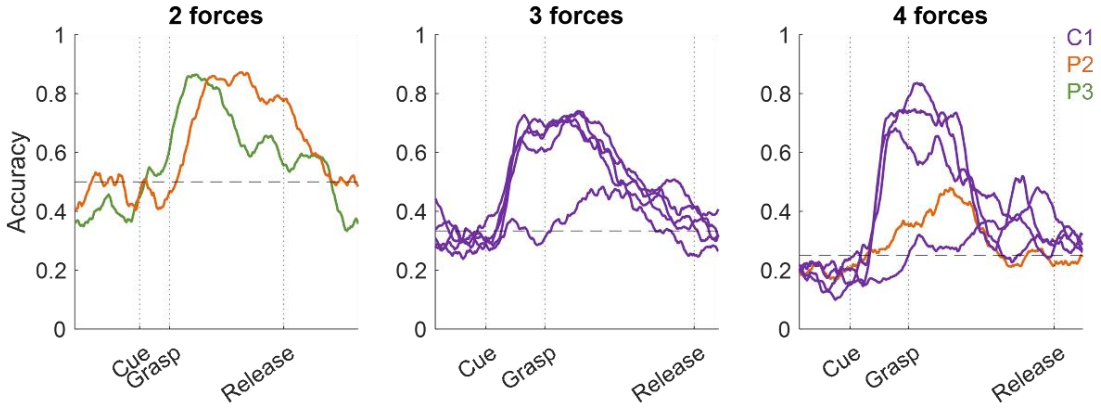

Supplementary Figure 5.1 - Force classification accuracy as a function of time for all sessions split by number of target force levels. Lines are color coded by subject.

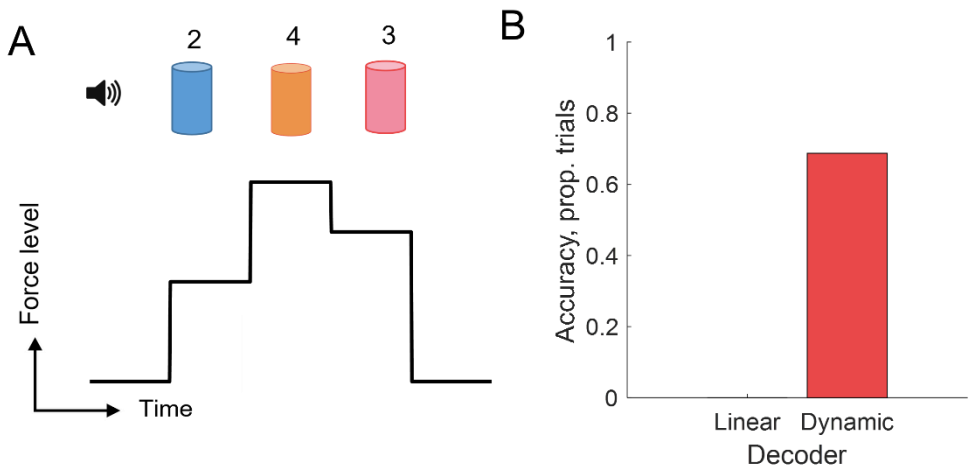

Supplementary Figure 5.2 - Adjustable force task. (A) Diagram of the task structure. The subject had to grasp the object with a cued amount of force and adjust force twice. The sequence of force levels was random each trial. (B) Linear and Dynamic decoder performance on the adjustable force task in subject C1.

5.6 References

Ajiboye, A. B., Willett, F. R., Young, D. R., Memberg, W. D., Murphy, B. A., Miller, J. P., Walter, B. L., Sweet, J. A., Hoyen, H. A., Keith, M. W., Peckham, P. H., Simeral, J. D., Donoghue, J. P., Hochberg, L. R., & Kirsch, R. F. (2017). Restoration of reaching and grasping movements through brain-controlled muscle stimulation in a person with tetraplegia: A proof-of-concept demonstration. *The Lancet*, *389*(10081), 1821–1830. https://doi.org/10.1016/S0140-6736(17)30601-3

Bensmaia, S. J., & Miller, L. E. (2014). Restoring sensorimotor function through intracortical interfaces: Progress and looming challenges. *Nature Reviews Neuroscience*, *15*(5), Article 5. https://doi.org/10.1038/nrn3724

Blabe, C. H., Gilja, V., Chestek, C. A., Shenoy, K. V., Anderson, K. D., & Henderson, J. M. (2015). Assessment of brain–machine interfaces from the perspective of people with paralysis. *Journal of Neural Engineering*, *12*(4), 043002. https://doi.org/10.1088/1741-2560/12/4/043002

Branco, M. P., de Boer, L. M., Ramsey, N. F., & Vansteensel, M. J. (2019). Encoding of kinetic and kinematic movement parameters in the sensorimotor cortex: A Brain-Computer Interface perspective. *European Journal of Neuroscience*, *50*(5), 2755–2772. https://doi.org/10.1111/ejn.14342

Branco, M. P., Geukes, S. H., Aarnoutse, E. J., Vansteensel, M. J., Freudenburg, Z. V., & Ramsey, N. F. (2019). High-frequency band temporal dynamics in response to a grasp force task. *Journal of Neural Engineering*, *16*(5), 056009. https://doi.org/10.1088/1741-2552/ab3189

Carmena, J. M., Lebedev, M. A., Crist, R. E., O'Doherty, J. E., Santucci, D. M., Dimitrov, D. F., Patil, P. G., Henriquez, C. S., & Nicolelis, M. A. L. (2003). Learning to Control a Brain–Machine Interface for Reaching and Grasping by Primates. *PLOS Biology*, *1*(2), e42. https://doi.org/10.1371/journal.pbio.0000042

Collinger, J. L., Wodlinger, B., Downey, J. E., Wang, W., Tyler-Kabara, E. C., Weber, D. J., McMorland, A. J., Velliste, M., Boninger, M. L., & Schwartz, A. B. (2013). High-performance neuroprosthetic control by an individual with tetraplegia. *The Lancet*, *381*(9866), 557–564. https://doi.org/10.1016/S0140-6736(12)61816-9

Dekleva, B. M., Chowdhury, R. H., Batista, A. P., Chase, S. M., Yu, B. M., Boninger, M. L., & Collinger, J. L. (2023). *Motor cortex retains and reorients neural dynamics during motor imagery* (p. 2023.01.17.524394). bioRxiv. https://doi.org/10.1101/2023.01.17.524394

Dekleva, B. M., Weiss, J. M., Boninger, M. L., & Collinger, J. L. (2021). Generalizable cursor click decoding using grasp-related neural transients. *Journal of Neural Engineering*, *18*(4), 0460e9. https://doi.org/10.1088/1741-2552/ac16b2

Deo, D. R., Willett, F. R., Avansino, D. T., Hochberg, L. R., Henderson, J. M., & Shenoy, K. V. (2023). *Translating deep learning to neuroprosthetic control* (p. 2023.04.21.537581). bioRxiv. https://doi.org/10.1101/2023.04.21.537581

Downey, J. E., Weiss, J. M., Flesher, S. N., Thumser, Z. C., Marasco, P. D., Boninger, M. L., Gaunt, R. A., & Collinger, J. L. (2018). Implicit Grasp Force Representation in Human Motor Cortical Recordings. *Frontiers in Neuroscience*, *12*. https://www.frontiersin.org/articles/10.3389/fnins.2018.00801

Evarts, E. V. (1968). Relation of pyramidal tract activity to force exerted during voluntary movement. *Journal of Neurophysiology*, *31*(1), 14–27. https://doi.org/10.1152/jn.1968.31.1.14

Flesher, S. N., Collinger, J. L., Foldes, S. T., Weiss, J. M., Downey, J. E., Tyler-Kabara, E. C., Bensmaia, S. J., Schwartz, A. B., Boninger, M. L., & Gaunt, R. A. (2016). Intracortical microstimulation of human somatosensory cortex. *Science Translational Medicine*, *8*(361), 361ra141-361ra141. https://doi.org/10.1126/scitranslmed.aaf8083

Flesher, S. N., Downey, J. E., Weiss, J. M., Hughes, C. L., Herrera, A. J., Tyler-Kabara, E. C., Boninger, M. L., Collinger, J. L., & Gaunt, R. A. (2021). A brain-computer interface that evokes tactile sensations improves robotic arm control. *Science (New York, N.Y.)*, *372*(6544), 831–836. https://doi.org/10.1126/science.abd0380

Gardner, E. P., Ro, J. Y., Babu, K. S., & Ghosh, S. (2007). Neurophysiology of Prehension. II. Response Diversity in Primary Somatosensory (S-I) and Motor (M-I) Cortices. *Journal of Neurophysiology*, *97*(2), 1656–1670. https://doi.org/10.1152/jn.01031.2006

Georgopoulos, A. P., Ashe, J., Smyrnis, N., & Taira, M. (1992). The Motor Cortex and the Coding of Force. *Science*, *256*(5064), 1692–1695. https://doi.org/10.1126/science.256.5064.1692

Glaser, J. I., Benjamin, A. S., Chowdhury, R. H., Perich, M. G., Miller, L. E., & Kording, K. P. (2020). *Machine learning for neural decoding* (arXiv:1708.00909). arXiv. https://doi.org/10.48550/arXiv.1708.00909

Hendrix, C. M., Mason, C. R., & Ebner, T. J. (2009). Signaling of Grasp Dimension and Grasp Force in Dorsal Premotor Cortex and Primary Motor Cortex Neurons During Reach to Grasp in the Monkey. *Journal of Neurophysiology*, *102*(1), 132–145. https://doi.org/10.1152/jn.00016.2009

Hepp-Reymond, M.-C., Kirkpatrick-Tanner, M., Gabernet, L., Qi, H.-X., & Weber, B. (1999). Context-dependent force coding in motor and premotor cortical areas. *Experimental Brain Research*, *128*(1), 123–133. https://doi.org/10.1007/s002210050827

Hochberg, L. R., Bacher, D., Jarosiewicz, B., Masse, N. Y., Simeral, J. D., Vogel, J., Haddadin, S., Liu, J., Cash, S. S., van der Smagt, P., & Donoghue, J. P. (2012). Reach and grasp by people with tetraplegia using a neurally controlled robotic arm. *Nature*, *485*(7398), Article 7398. https://doi.org/10.1038/nature11076

Intveld, R. W., Dann, B., Michaels, J. A., & Scherberger, H. (2018). Neural coding of intended and executed grasp force in macaque areas AIP, F5, and M1. *Scientific Reports*, *8*(1), Article 1. https://doi.org/10.1038/s41598-018-35488-z

Kalaska, J. F., Cohen, D. A., Hyde, M. L., & Prud'homme, M. (1989). A comparison of movement direction-related versus load direction-related activity in primate motor cortex, using a two-dimensional reaching task. *The Journal of Neuroscience: The Official Journal of the Society for Neuroscience*, *9*(6), 2080–2102. https://doi.org/10.1523/JNEUROSCI.09-06-02080.1989

Maier, M. A., Bennett, K. M., Hepp-Reymond, M. C., & Lemon, R. N. (1993). Contribution of the monkey corticomotoneuronal system to the control of force in precision grip. *Journal of Neurophysiology*, *69*(3), 772–785. https://doi.org/10.1152/jn.1993.69.3.772

Okorokova, E. V., Goodman, J. M., Hatsopoulos, N. G., & Bensmaia, S. J. (2020). Decoding hand kinematics from population responses in sensorimotor cortex during grasping. *Journal of Neural Engineering*, *17*(4), 046035. https://doi.org/10.1088/1741-2552/ab95ea

Pandarinath, C., & Bensmaia, S. J. (2022). The science and engineering behind sensitized brain-controlled bionic hands. *Physiological Reviews*, *102*(2), 551–604. https://doi.org/10.1152/physrev.00034.2020

Rastogi, A., Willett, F. R., Abreu, J., Crowder, D. C., Murphy, B. A., Memberg, W. D., Vargas-Irwin, C. E., Miller, J. P., Sweet, J., Walter, B. L., Rezaii, P. G., Stavisky, S. D., Hochberg, L. R., Shenoy, K. V., Henderson, J. M., Kirsch, R. F., & Ajiboye, A. B. (2021). The Neural Representation of Force across Grasp Types in Motor Cortex of Humans with Tetraplegia. *ENeuro*, *8*(1), ENEURO.0231-20.2020. https://doi.org/10.1523/ENEURO.0231-20.2020

Shelchkova, N., Downey, J., Greenspon, C., Okorokova, E., Sobinov, A., Verbaarschot, C., He, Q., Sponheim, C., Tortolani, A., Moore, D., Kaufman, M., Lee, R., Satzer, D., Gonzalez-Martinez, J., Warnke, P., Miller, L., Boninger, M., Gaunt, R., Collinger, J., … Bensmaia, S. (2022). *Microstimulation of human somatosensory cortex evokes task-dependent, spatially patterned responses in motor corte*. https://doi.org/10.1101/2022.08.10.503543

Wannier, T. M., Maier, M. A., & Hepp-Reymond, M. C. (1991). Contrasting properties of monkey somatosensory and motor cortex neurons activated during the control of force in precision grip. *Journal of Neurophysiology*, *65*(3), 572–589. https://doi.org/10.1152/jn.1991.65.3.572

Wodlinger, B., Downey, J. E., Tyler-Kabara, E. C., Schwartz, A. B., Boninger, M. L., & Collinger, J. L. (2014). Ten-dimensional anthropomorphic arm control in a human brain−machine interface: Difficulties, solutions, and limitations. *Journal of Neural Engineering*, *12*(1), 016011. https://doi.org/10.1088/1741-2560/12/1/016011

Chapter 6 | Biomimetic encoding model for restoring touch in bionic hands through a nerve interface[4]

6.1 Abstract

Background: Hand function can be restored in upper-limb amputees by equipping them with anthropomorphic prostheses controlled with signals from residual muscles. The dexterity of these bionic hands is severely limited in large part by the absence of tactile feedback about interactions with objects. We propose that, to the extent that artificial touch mimics its natural counterpart, these sensory signals will be more easily integrated into the motor plan for object manipulation. *Methods:* We describe an approach to convey tactile feedback through electrical stimulation of the residual somatosensory nerves that mimics the aggregate activity of tactile fibers that would be produced in the nerve of a native hand during object interactions. Specifically, we build a parsimonious model that maps the stimulus – described as time-varying indentation depth, indentation rate, and acceleration – into continuous estimates of the time-varying population firing rate and of the size of the recruited afferent population. *Results:* The simple model can reconstruct aggregate afferent responses to a wide range of stimuli, including those experienced during activities of daily living. *Conclusion:* We discuss how the proposed model can be implemented with a peripheral nerve interface and anticipate it will lead to improved dexterity for prosthetic hands.

[4] This chapter was published: Okorokova, E. V., He, Q., & Bensmaia, S. J. (2018). Biomimetic encoding model for restoring touch in bionic hands through a nerve interface. Journal of neural engineering, 15(6), 066033. Supplementary materials are available online.

6.2 Introduction

Manual interactions with objects involve not only precise control of the fingers and wrist but also a continuous barrage of somatosensory signals from the hand (Johansson & Flanagan, 2009). These signals convey information about hand movements and postures, about physical interactions with the object – contact location, contact timing, contact pressure, slip –, and about the object itself – its size, shape, and texture. Some of these signals, particularly those related to hand proprioception, are carried by nerve fibers that innervate the muscles and tendons. Others, those related to object contact in particular, are carried by thousands of tactile nerve fibers that innervate the palmar surface of the hand. The different classes of nerve fibers differ in their response properties: slowly adapting type 1 fibers (SA1) respond best to skin indentations, slowly adapting type 2 fibers (SA2) to skin stretch, rapidly adapting (RA) fibers and Pacinian corpuscle (PC) fibers to low and high frequency vibrations, respectively (Saal & Bensmaia, 2015). SA2 fibers are not included in TouchSim because these fibers absent in the glabrous skin of monkeys (from whose afferent responses TouchSim was developed). Without these tactile signals, dexterity is severely compromised (Augurelle, 2002; Witney, Wing, Thonnard, & Smith, 2004).

Much of what is known about neural coding in the peripheral nerve stems from recordings from individual nerve fibers in anesthetized monkeys or awake humans (Talbot & Mountcastle, 1968; Vallbo & Hagbarth, 1968). Attempts to reconstruct the responses of afferent populations based on single afferent recordings typically involve estimating time averaged firing rates across afferent populations. The prevailing conclusion from this body of work is that individual tactile fibers carry ambiguous information about a contacted object and that tactile information is distributed over populations of fibers (Johnson, 2001; Muniak, Ray, Hsiao, Dammann, & Bensmaia, 2007; Saal & Bensmaia, 2014).

We have recently developed a computational model – dubbed TouchSim – that simulates the responses of all tactile fibers to any spatiotemporal deformation of the skin of the hand (Saal, Delhaye, Rayhaun, & Bensmaia, 2017). With this model, we can characterize with unprecedented spatial and temporal precision how tactile information is distributed across afferent populations. In addition to its potential to address basic questions about sensory coding in the somatosensory nerves, this newfound capability can inform precisely how to restore the sense of touch in bionic hands through electrical activation of tactile nerve fibers (Delhaye, Saal, & Bensmaia, 2016; S. S. Kim et al., 2009; Saal & Bensmaia, 2015).

Indeed, given the importance of touch to dexterity, to construct an agile bionic hand requires not only the ability to move the hand precisely but also the means to receive tactile signals about the consequences of these movements, particularly as they pertain to object interactions (Bensmaia & Miller, 2014; Saal & Bensmaia, 2015). In principle, TouchSim provides us with a precise blueprint of tactile restoration as it describes how each tactile nerve fiber will respond to object contact. However, manual interactions with objects evoke responses that differ across fibers depending on their type, their location with respect to the stimulus, and even idiosyncratic differences across nerve fibers of a given type (Roland S Johansson & Flanagan, 2009; Johnson, 2001; Vallbo & Hagbarth, 1968; (Dong et al., 2013)). Accordingly, to restore natural touch would require stimulating each fiber independently with its own idiosyncratic stimulation pattern, a feat that current technologies are nowhere near ready to accomplish. Indeed, state-of-the-art electrical interfaces with the nerve comprise tens or hundreds of channels, not the twelve or so thousand that would be required for fully biomimetic restoration of touch on the palmar surface of the hand. Furthermore, at typical stimulation levels, each channel activates tens or hundreds of fibers and evokes highly unnatural synchronous responses in these fibers. Until much denser and more

selective neural interfaces become available, then, attempts to mimic nerve responses will have to settle for mimicking aggregate neural responses (Delhaye et al., 2016; Saal & Bensmaia, 2015).

TouchSim can be used to simulate the aggregate behavior of hundreds or thousands of fibers by pooling simulated responses across small afferent populations. From the perspective of engineering a bionic hand, however, simulating tens of thousands of fibers to then collapse them into a small number of unidimensional signals is highly inefficient.

With this in mind, we have developed a new, intuitive, computationally inexpensive encoding algorithm, one that comprises only a handful of parameters but that reconstructs with high accuracy the aggregate response of the nerve to time-varying pressure applied to the fingertip. We examine the properties of this population signal and demonstrate that it far outperforms more traditional sensory encoding algorithms in reconstructing the nerve activity evoked during activities of daily living (Clark et al., 2014; Gurpreet Singh Dhillon & Horch, 2005; Graczyk et al., 2016; Stanisa Raspopovic, 2014; Schiefer, Tan, Sidek, & Tyler, 2016; Daniel W. Tan et al., 2014). We propose that this simple model is precisely what is needed to convert the output of force or pressure sensors on bionic hands into biologically realistic patterns of electrical stimulation of the nerve. Bionic hands endowed with this algorithm will provide more realistic tactile feedback to the user thereby supporting dexterous interactions with objects. More naturalistic feedback may also improve the embodiment of bionic hands and the confidence of users in using them (Marasco, Kim, Colgate, Peshkin, & Kuiken, 2011; Schiefer et al., 2016).

6.3 Results

The proposed strategy to restore touch consists of converting the output of sensors on the prosthetic hand into patterns of electrical stimulation to evoke naturalistic patterns of aggregate activity in the residual nerve (Figure 6.1). To this end, we simulate, using TouchSim (Saal et al., 2017), the

spiking responses of a population of nerve fibers when a tactile stimulus is applied to a localized patch of skin. We then pool all the simulated responses to obtain the time-varying population firing rate (FR_t). We also evaluate the time-varying surface of afferent activation by inscribing all active afferent locations in a polygon and computing its area (A_t). This latter quantity represents the size of the activated population, which is related to but not identical with the population firing rate. Indeed, increasing stimulus intensity results not only in an increase in the firing rate of activated tactile fibers but also in the recruitment of additional fibers with receptive fields away from the point of contact (Johnson, 1974; Muniak et al., 2007). As discussed below, these two aspects of the response – firing rate and activated area – are required to map neural response onto parameters of electrical stimulation. Next, we develop a simple mapping between the stimulus – decomposed into its time varying indentation, indentation rate, and acceleration – and the aggregate response representations (firing rate, area of activation) to obviate the need for the computationally demanding and excessively detailed simulation of the entire nerve. Finally, we compare the resulting biomimetic encoding model to a more conventional encoding model that signals instantaneous pressure.

6.4 Biomimetic encoding model

First, we simulated the responses to mechanical noise whose frequency composition matched that of natural interactions with objects and of indentations of varying durations and amplitudes as the latter are overrepresented during manual interactions with objects (during maintained grasp, for example). Stimulus amplitudes spanned the range experienced during activities of daily living (0 to 3 mm). The training set was thus selected to yield a model that is well suited for common manual tasks (see below). Having simulated the aggregate response, we then regressed the time-varying firing rate (FR_t) and time-varying area of activation (A_t) onto the indentation depth, rate, and

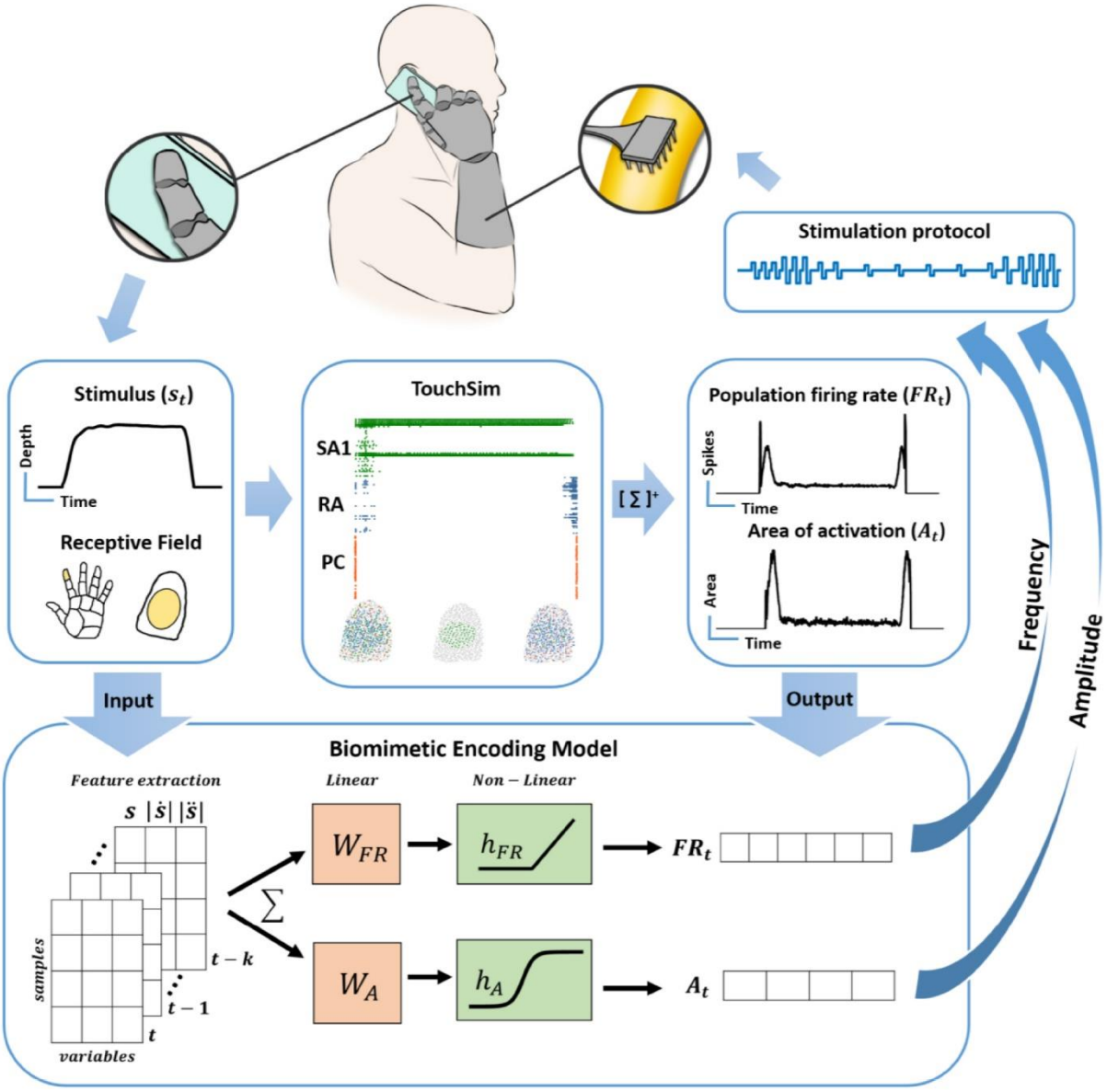

Figure 6.1 - Biomimetic tactile feedback in a bionic hand. Top flow: contact with an object produces temporal patterns of pressure on a sensor at the fingertip of the prosthetic hand. In principle, the sensor output could be used as input to TouchSim, which would simulate the responses of each afferent innervating the glabrous skin. Spikes could then be pooled across all afferents and binned to yield the firing rate of the whole nerve (FR_t), as well as the recruitment of nerve fibers (A_t). These two metrics indicate how to modulate frequency and pulse charge to produce a biomimetic pattern of nerve activation. Bottom flow: the computationally demanding simulation of TouchSim can be replaced with a simpler model that comprises only a handful of parameters to predict aggregate nerve activity. To this end, we find a mapping between stimulus (pressure) and population activity (firing rate and recruitment) using a combination of linear and nonlinear filters.

accelerations of the stimulus. For area, this linear regression was the input to a sigmoidal function to capture the leveling-off of activated area at high amplitudes (Figure 6.1 and Supplementary Figure 1C). Both models included several time points for all three variables to capture stimulus

dynamics (5 time points, spanning a total of 10 ms for each variable in firing rate model, 2 lags spanning a total of 20 ms for each variable in area model, see Methods). The resulting models thus mapped the time-varying response onto the time-varying stimulus with up to 15 stimulus-related

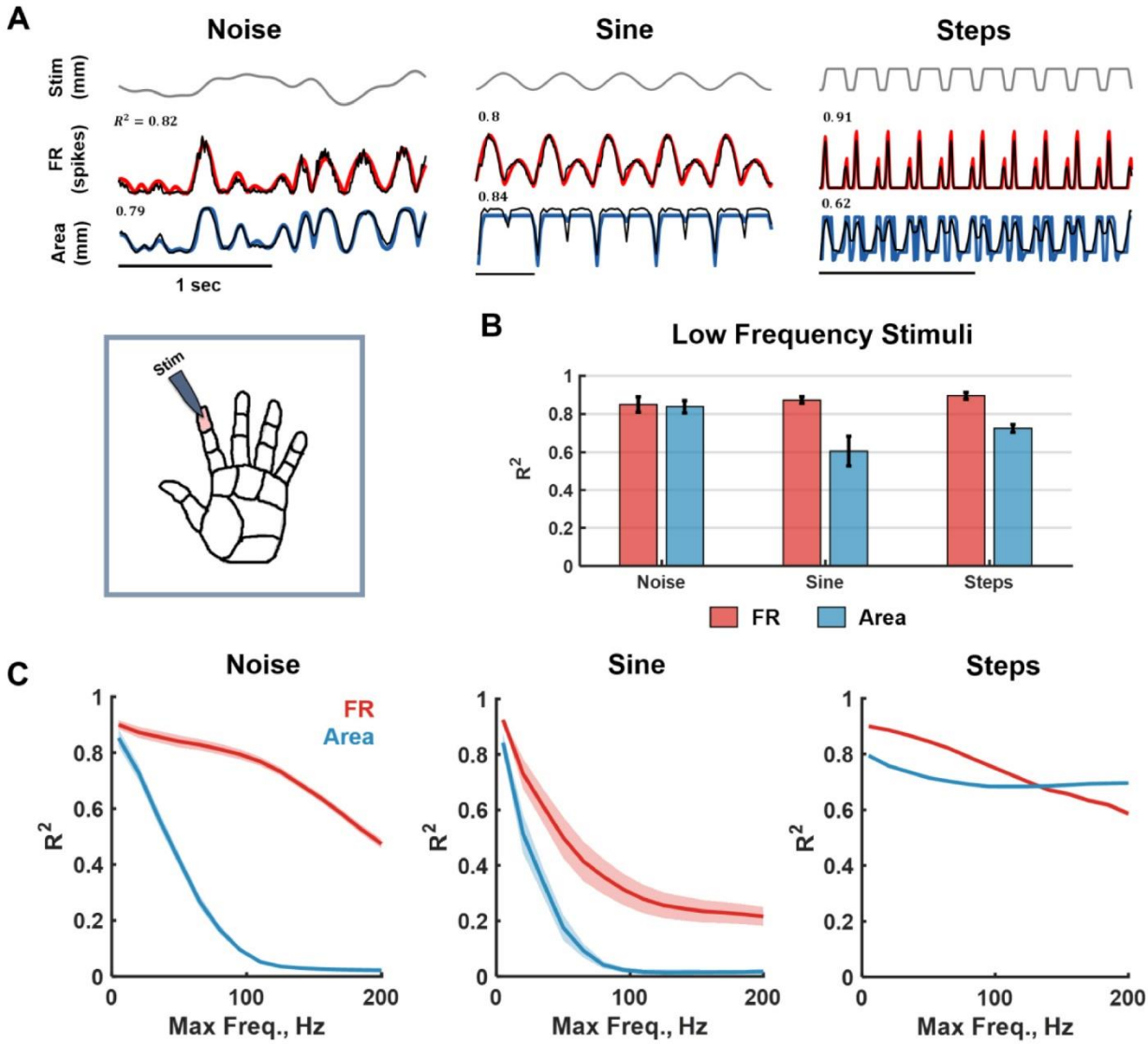

Figure 6.2 - Model validation with parametric stimuli. (A) Inset: the index finger pad was stimulated with a set of tactile stimuli—noise, sinusoids and sustained indentations (steps). Main: examples of model fits. Top: time-varying stimulus trace. Middle: population firing rate $(F{{R}_{t}})$ computed using the full afferent model (TouchSim, black) and using the simplified biomimetic model (red). Bottom: time varying area of activation computed using TouchSim (black) and using the biomimetic model (blue). R2 denotes the match between TouchSim and the simple model predictions for that trace. (B) Mean goodness-of-fit for the firing rate and area models trained to reconstruct low-frequency stimuli (up to 10 Hz). The test sample consisted of noise filtered below 10 Hz (different seed), steps (of random amplitudes and durations), and sinusoids (from 1 to 10 Hz). The simple model captures most of the variance in both the aggregate firing rate and activated area over this range of frequencies. (C) Mean goodness-of-fit of firing rate (red) and area (blue) predictions as a function of the low-pass cut-off frequency of the stimuli for noise, sinusoids, aand steps. Forty models were trained with varying cut-off frequencies (5 Hz–200 Hz) and tested on sinusoids and noise (comprising components with frequencies at or below the training cut-off) and steps of random amplitudes and duration. At high frequencies, the aggregate response becomes tonic rather than oscillatory so performance plummets for sinusoids and noise (see detailed fits in supplementary figure 2).

parameters and an intercept (with three additional parameters for the area computation to capture saturation).

6.5 Model performance

6.5.1 Noise, sinusoids, and steps

First, we examined the ability of the model to account for responses to parametric stimuli including sinusoids over a range of frequencies, pink noise with different band-passes, and sustained indentations varying in duration and amplitude (Figure 6.2A). We found that model performance was high for these stimuli, accounting for the bulk of the variance in the simulated aggregate firing rate (R^2 = 0.85, 0.87, 0.9 for noise, sinusoids and steps, respectively; Figure 6.2B- red) and area of activation (R^2 = 0.83, 0.61, and 0.71; Figure 6.2B - blue). Note that the model precisely captured the hallmark response of the nerve to indentations, which is dominated by onset and offset transients and is very weak during static indentation. This property of the nerve response is overlooked in standard encoding models that track time-varying pressure (Clark et al., 2014; Gurpreet Singh Dhillon & Horch, 2005; Graczyk et al., 2016; Stanisa Raspopovic, 2014; Schiefer et al., 2016; Daniel W. Tan et al., 2014). Testing the model across a wider range of frequencies, we found that performance deteriorated for high-frequency stimuli, especially for sinusoidal stimuli (> 60 Hz) (Figure 6.2C and Supplementary Figure 2), a phenomenon that can be attributed to two causes. First, the nerve is differentially sensitive at different frequencies and the model does not comprise a term that explicitly incorporates this frequency dependence (Supplementary Figure 1C). Second, although individual afferents – particularly RA and PC fibers – produce phase-locked responses to high-frequency vibrations (Mackevicius, Best, Saal, & Bensmaia, 2012; Talbot & Mountcastle, 1968), which in principle the model could follow, this signal vanishes when

responses are pooled because different fibers spike at different phases within each cycle (Manfredi et al., 2012).

6.5.2 Natural stimuli

Next, we tested the model's ability to account for responses evoked during manual interactions

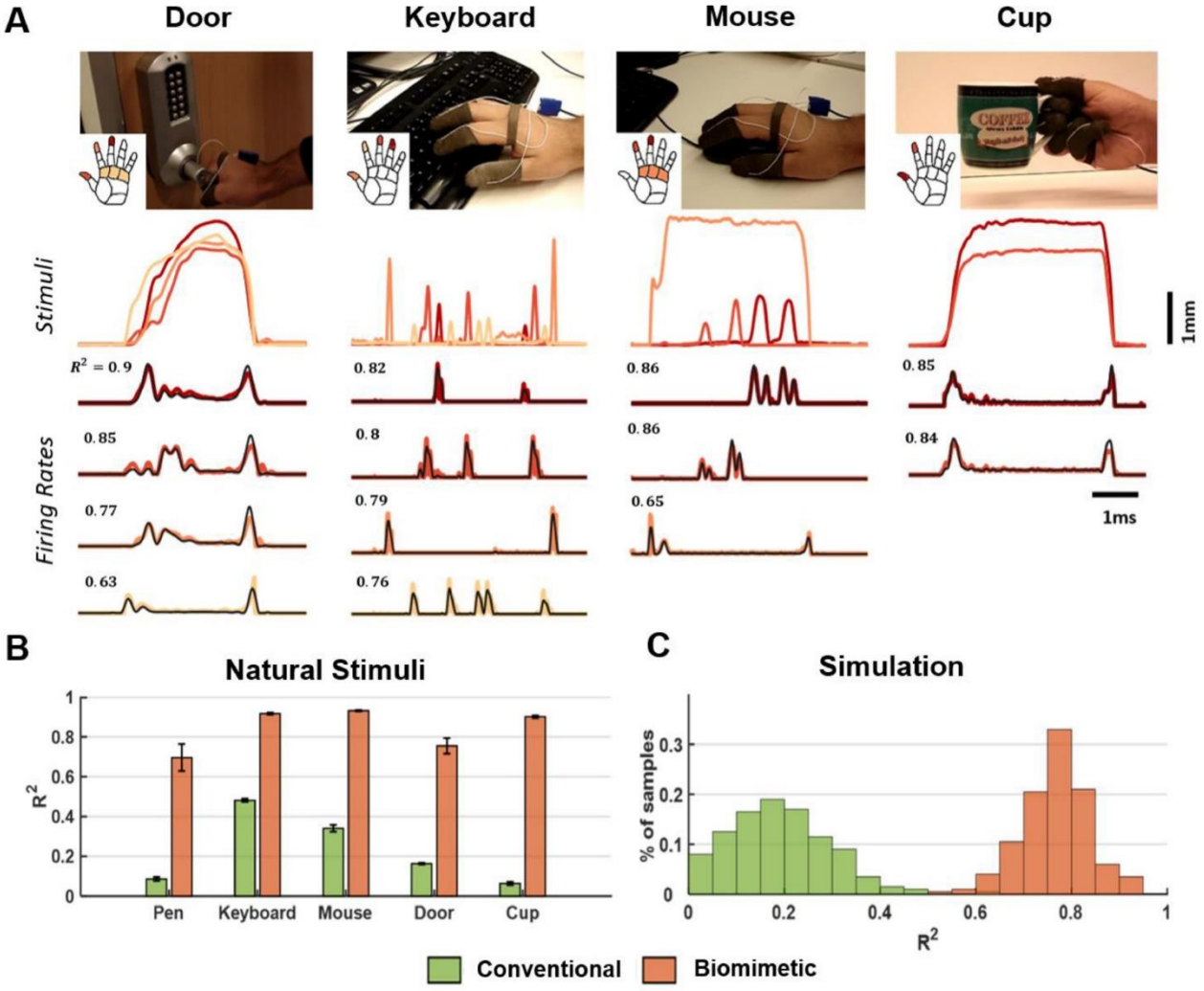

Figure 6.3 - Model validation with natural stimuli. (A) Sample traces from pressure sensors on the fingertips and the palm along with the firing rate FR_t estimated using TouchSim or the biomimetic model for four activities of daily living: opening a door, typing on a keyboard, using a mouse, and picking up a cup. Top: each trace denotes the stimulus, color coded by location (see inset). Bottom traces: population firing rate (black) versus predicted firing rate computed for each task and each projection field (same color as the corresponding stimulus). R2 denotes match between TouchSim and simple model predictions for that trace. (B) Model performance, averaged across all sessions and hand locations with significant sensor output. The green and orange bars denote the performance of the conventional and biomimetic encoding models, respectively. Error bars show standard errors in each sample. (C) Performance of the two models for simulated tactile stimuli mimicking natural stimuli (n = 200).

with objects. Specifically, we measured the time-varying pressure at the fingertips and palm as a

subject performed a series of activities of daily living (ADL), including grasping a cup, writing with a pen, typing, using a computer mouse, and opening a door. The pressure traces evoked during ADLs are dominated by low frequencies and informed the selection of training stimuli to fit the model. Time-varying skin deformations at each skin location were estimated from the pressure output of the sensor and were used as input to the model. We then compared model predictions to aggregate responses simulated using TouchSim and found that the linear model accounted for a large proportion of the variance in the ADL-evoked responses (Figure 6.3A-B, R^2=0.84).

Next, we compared the performance of the biomimetic encoding model to that of the standard encoding model, which simply tracks pressure. We found that the biomimetic model massively outperformed the standard model on the ADL-evoked responses (ΔR^2 = 0.6, paired t-test: $t(15)$ = 17.86, p = 1.6e-11). As a further test of the model, we simulated the responses to 200 stimuli designed to mimic ADLs (see Methods) and found that the biomimetic model far outperformed the standard algorithm for these stimuli as well (ΔR^2 = 0.57, paired t-test: $t(199)$ = 159, p = 9.8e-212, Figure 6.3C). The biomimetic encoding model outperforms the standard one primarily because it takes into account the fact that the nerve is much more responsive to contact transients – by including velocity and acceleration terms – and responds only weakly to sustained pressure (Figure 6.2A and Figure 6.3A).

6.6 Discussion

6.6.1 Stimulation strategy

The proposed biomimetic model provides a faithful estimate of the response that one would wish to elicit in populations of tactile fibers. The overall firing rate (FR_t) evoked in the nerve, given the spatially restricted stimulus, is likely confined to a single fascicle. The firing rate is determined by the activation charge rate, essentially the amount of suprathreshold current delivered to the

fascicle (Graczyk et al., 2016). However, standard electrical pulse trains comprise two parameters – pulse charge and frequency – and population firing rate can be controlled by modulating either parameter. In contrast, area of activation is a proxy for the cross-section of the fascicle that is activated at any given time, a quantity that can be controlled by modulating pulse charge. The ratio of firing rate to area constitutes an estimate of the mean firing rate of activated neurons, a quantity that can be controlled by modulating pulse frequency. We find that the ratio (of population firing rate to number of activated fibers) estimated using our model accurately reproduces the ratio derived from simulated responses with TouchSim (Supplementary Figure 3). The simple model proposed here can then be used to specify the values of these two parameters of electrical stimulation as a function of time to produce naturalistic patterns of nerve activation based on the time-varying output of pressure sensors on a prosthetic hand.

The accuracy of our modeling approach places greater emphasis on understanding precisely how stimulation regime – pulse charge, pulse frequency, and pulse waveform – maps onto evoked afferent activation. To predict the neuronal response evoked by a pattern of electrical stimulation requires a realistic biophysical model of somatosensory nerves. Recently, single-cell- and population-level models have been developed to describe the response of the nerve to different patterns of injected current (O'Brien, 2016). These models, however, are specific to the neural interface used for stimulation. Indeed, intrafascicular and extrafascicular interfaces imply different tissue conductivities and electric field distributions and, thus, different patterns of afferent recruitment with the changes in injected current (Grinberg, Schiefer, Tyler, & Gustafson, 2008; Veltink, van AlstÉ, & Boom, 1988). Intraneural interfaces consist of electrodes that penetrate the epineurium and make direct contact with nerve fibers (LIFE - Boretius et al., 2010; TIME - Gurpreet S. Dhillon, Lawrence, Hutchinson, & Horch, 2004; USEA - Ledbetter et al., 2013). For

these interfaces, modeling electrically evoked spiking activity typically involves the implementation of a model of spike generation at the Nodes of Ranvier, a model of myelinated internodes, and a description of the extracellular space (O'Brien, 2016). For extrafascicular interfaces (FINE - Leventhal & Durand, 2004; Tyler & Durand, 2002), however, the stimulating electrodes do not directly contact their neuronal targets and neuronal activation also depends on spatial factors, such as electrode configuration (Miller, Abbas, Nourski, Hu, & Robinson, 2003), pulse polarity (Rattay, 1989), electrode-fiber distance (Mino, Rubinstein, Miller, & Abbas, 2004), and nerve fiber geometry (Woo, Miller, & Abbas, 2010). In many cases, spatial factors are idiosyncratic and must be assessed on a subject by subject basis, for example the distribution of nerve fascicles at the current injection site and the geometry of the channel relative to the nerve fibers (N. A. Brill & Tyler, 2017; N. Brill & Tyler, 2011; Gustafson et al., 2009). Furthermore, stimulation regimes must be evaluated for their potential to cause damage to the neural tissue with chronic deployment (Briaire & Frijns, 2006). While a detailed discussion of how to design a precise and accurate mapping between electrical stimulation and neuronal activation falls outside the scope of the present paper, the proposed encoding model establishes a need for such a mapping, which would make possible the elicitation of neuronal patterns of activation whose naturalism is limited only by the capabilities of the neural interface.

6.6.2 Submodality-specific models

Some evidence suggests that tactile nerve fibers are clustered according to their modalities (Hallin et al., 1991; Niu et al., 2013). That is, handfuls of fibers of a single class (SA1, RA, PC) are grouped together, and these bundles are interleaved seemingly randomly throughout the fascicle. However, the spatial scale over which this clustering occurs is too small and its distribution over the fascicle too idiosyncratic to be reliably exploited by a neural interface. Nevertheless, once spatial

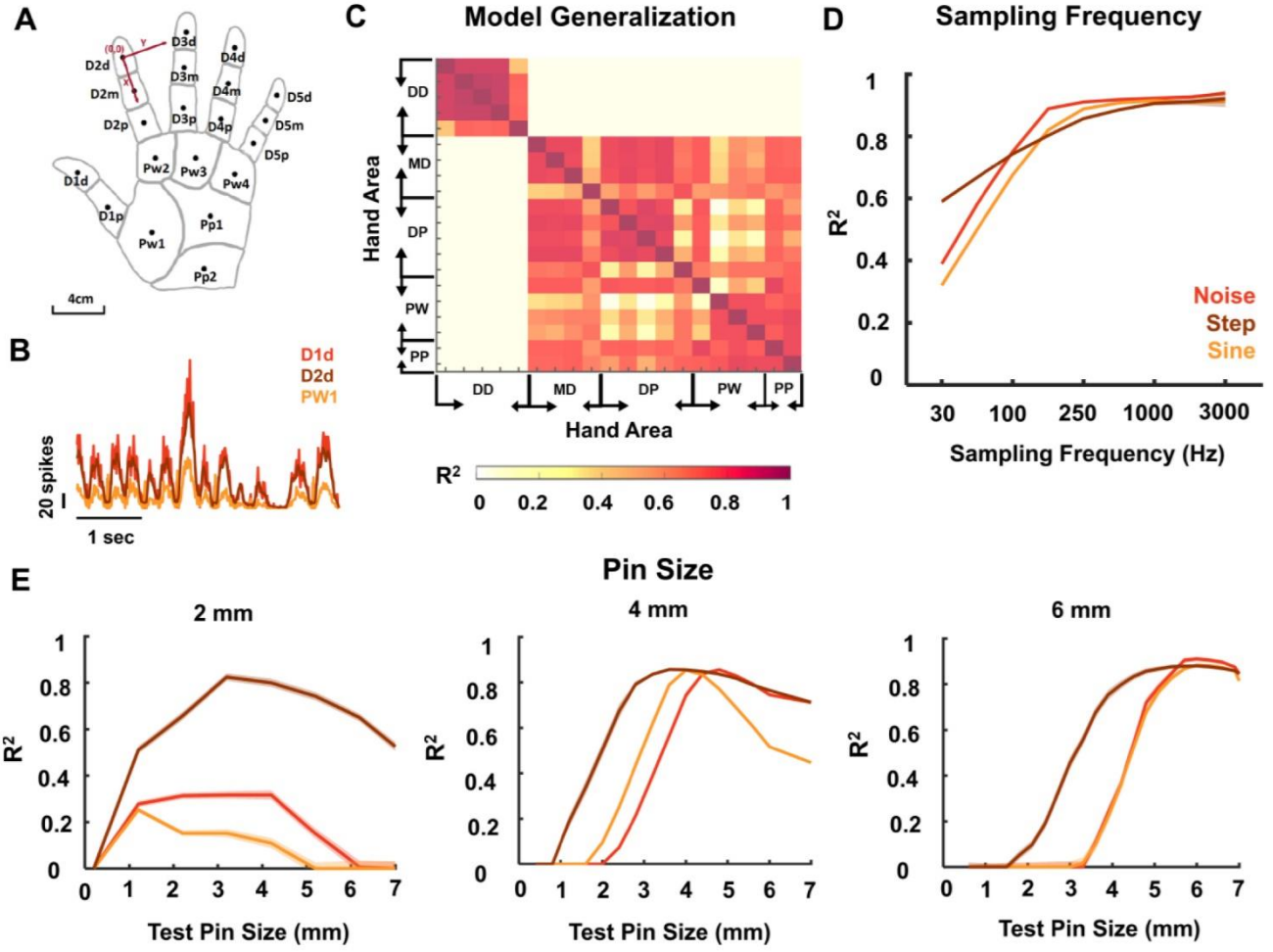

Figure 6.4 - Model implementation details. Firing rate model performance depends on the location of the projection field, the sampling rate of the sensor, and the size of the contact area (corresponding to the size of the projection field). (A) Schematic of the hand used in the model with abbreviations of hand areas and locations of the centers of projection fields used for each area (black dots). (B) Firing rate traces FRt computed for three locations of the hand using the same time-varying noise stimulus. Responses from the distal digits (D1d and D2d) are similar to each other, but differ from responses from the palm (PW1). (C) R2 between FRt traces derived for different locations of the hand. (D) Mean performance as a function of sampling frequency. Model performance improves as temporal resolution of the sensor input improves. (E) Mean performance as a function of contact area size (diameter of the pin). The model was trained with a contact area of diameter of 2, 4, and 6 mm, respectively, then was tested with different smaller/larger contact areas with diameters ranging from 0.1 to 7 mm. For all analyses, the model was trained using sustained indentations and pink noise filtered below 5 Hz. Test set consisted of steps of varying length and amplitude, noise of random seed and sinusoids of varying frequencies (<5 Hz). Model must be tailored to the size of the projection field.

selectivity of stimulation is improved, the present model can be used to stimulate each tactile submodality appropriately (Supplementary Figure 4). For low-frequency stimuli, the submodality-specific models are accurate for SA1 and RA responses (Supplementary Figure 4C). As might be expected, however, the reconstruction of PC responses is poor because this class of fibers responds poorly at low frequencies (Supplementary Figure 4A-B).

6.6.3 Implementation notes

The sampling rate of sensors on the bionic hand is a key design specification for the proposed biomimetic model. Indeed, afferent responses cannot be accurately estimated if the temporal resolution of the input is too coarse (less than 10ms, Figure 6.4D). If a sufficient resolution cannot be achieved, model performance can be rescued to an extent by resampling the sensor values through interpolation.

Another important consideration relates to the size and location of the projection field as the model parameters depend on the size of the estimated afferent population and the location of their receptive fields. Indeed, the number of tactile fibers and the relative proportions of afferents of each type depend on both of these factors. We designed the model for a contact area with a diameter of 6 mm on the fingertip, thus corresponding to a projection field of equivalent size. However, this specific model breaks down when the contact area is much smaller or much bigger (see Figure 6.4E), because of the concomitant changes in the sizes and composition of the activated nerve fibers. In light of this, successful deployment of the model requires that the projection field of each electrode be mapped precisely, for example by having the subject report the location and spatial extent of electrically evoked sensations (see Clark et al., 2014; Tan et al., 2014). The idea is to design the model for each electrode such that the contact area matches the spatial extent of the projection field. As a result, stimulation will produce a sensation whose spatial extent is

commensurate with that of a stimulus of equivalent contact area. Otherwise, a mismatch between the size of the projection field and the resulting sensations might occur. Regarding location, models designed for one digit can be applied to other digits. However, the distal fingertips and the rest of the hand yield different models given the pronounced differences in innervation densities of the three classes of tactile nerve fibers across these skin locations (see Figure 6.4A-C). Be that as it may, the model for each electrode can readily be designed for the location and spatial extent of its projection field to optimize naturalness.

6.6.4 Limitations of the approach

As discussed above, the ideal somatosensory prosthesis would stimulate each nerve fiber independently with a pulse train designed to mimic that fiber's idiosyncratic response. However, given the limitations of current neural interfaces, we developed a linear model to describe the relationship between the time-varying stimulus and the pooled responses of nerve fibers that are liable to be activated by a given stimulating electrode. While the relationship between pooled firing rates and indentation depth is approximately linear at low frequencies, which dominate during activities of daily living, this linearity breaks down at high frequencies (Supplementary Figure 1C). Another source of lack of fit, described above, is the frequency-dependence of the afferent response, particularly at high frequencies, which is not explicitly taken into consideration in the model. These non-linearities result in a reduction in the prediction accuracy of the model, which is based on a linear mapping, particularly at the higher frequencies. Even at the low frequencies, the proposed model does not capture all of the variance in the neuronal response, as might be expected given the complex non-linearities between the stimulus and the responses of individual afferents. However, in the frequency range relevant for daily interactions with objects, model

predictions of aggregate afferent activity are substantially more faithful to the natural neural response than are predictions from the standard model.

The critical bottleneck for the proposed approach, however, is not the failure of the linear modeling approach to capture the fine spatio-temporal structure of the neural response but rather the limited selectivity of current stimulation technologies. Indeed, synchronous stimulation of many afferents limits the spatial resolution of the sensory feedback, obscuring spatial patterning in the stimulus that falls within the aggregate receptive field of the stimulated afferents. Furthermore, while the aggregate response of the stimulated afferents will be approximately biomimetic, the response of individual afferents will not, a feature that is likely to compromise the naturalness of the resulting percept. However, the model provides a close approximation of the response at the level that can be manipulated with existing technologies, so paves the way for the most biomimetic response that can be achieved given technological limitations. To the extent that the spatio-temporal dynamics of the aggregate nerve response matter, and given that afferent signals converge as they ascend the somatosensory neuraxis, the proposed sensory encoding algorithm is likely to improve the intuitiveness and utility of the resulting sensory feedback.

6.7 Methods

6.7.1 Computing population firing rate and activated area from TouchSim simulations

TouchSim simulates afferent responses in two steps. First, the stresses resulting from a stimulus applied at the surface of the skin are estimated as two distinct components, one quasi-static, the other dynamic. The quasi-static component confers to tactile fibers response properties resulting from contact mechanics, such as edge enhancement and surround suppression. The dynamic component propagates through the skin surface as a wave and confers to afferents the ability to respond to vibration at a distance from contact. Second, TouchSim computes the spiking responses

of nerve fibers – which tile the hand at their known densities (Johansson & Westling, 1984) – based on these two stress components using an integrate-and-fire mechanism. Responses simulated by TouchSim have been shown to match their measured counterparts closely – with single-digit millisecond precision – across a wide range of experimental conditions (Saal et al., 2017).

Simulated responses of all afferents with receptive fields on the palmar surface of the hand were pooled to obtain the time-varying population firing rate of the nerve (FR_t) in time increments of 2 ms (Figure 6.1 and Supplementary Figure 2B).

To estimate area of activation, we pooled the coordinates of all the SA1 and RA fibers that were activated within each 10-ms bin and inscribed them in a polygon of minimum area, A_t (Figure 6.1 and Supplementary Figure 1B). We excluded PC fibers in this computation because their receptive fields are so large as to span most of the hand, and a given PC fiber is activated by touch almost anywhere on the hand.

6.7.2 Training stimulus

The firing rate of populations of afferents has been shown to be approximately linear (Muniak et al., 2007) (Supplementary Figure 1C), but the slope of this function is dependent on stimulus frequency. To keep the model simple, we did not incorporate any frequency-dependent terms. As a result, the parameters of the model were dependent on the (training) stimulus used to obtain them. Indeed, the frequency composition of the training stimulus will determine the degree to which different frequency components are weighted in the determination of these parameters. Second, sustained indentations of the skin are common during natural interactions with objects – during maintained grasp for instance – but absent in a stimulus consisting entirely of noise. With this in mind, we designed a training stimulus that comprises both aspects observed in natural scenes. The stimulus comprised a mechanical noise component with power spectrum that

decreases with frequency proportional to $1/f$ (pink noise)$^{-}$. The noise was low-pass filtered to truncate high frequency components (see Results section on performance dependence on cut-off frequency) and the resulting stimulus was scaled to a maximum indentation amplitude of 3 mm (Supplementary Figure 1A). The training stimulus also contained skin indentations of varying duration – ranging from 1 to 5 seconds – and varying amplitude – ranging from 0 to 3 mm. We verified that the indentation rates of the resulting stimulus fell within a physiologically plausible range and did not exceed 80-90 cm/sec, the maximum indentation rate observed during object interactions (Säfström & Edin, 2008). A stimulus as short as 100 seconds was sufficient to train both the firing rate and the area models.

6.7.3 Biomimetic encoding model

We estimate time-varying firing rate ($\widehat{FR}_t$) and dynamic area of activation($\hat{A}_t$) using the following models (see Figure 6.1):

$$\begin{cases} \widehat{FR}_t = h_{FR}(W_{FR}S_t) \\ \hat{A}_t = h_A(b, W_A S_t) \end{cases}$$

$S_t = [1 \ s_t, s_{t-1}, \dots, s_{t-k}, |\dot{s}_t|, |\dot{s}_{t-1}|, \dots, |\dot{s}_{t-k}|, |\ddot{s}_t|, |\ddot{s}_{t-1}|, \dots, |\ddot{s}_{t-k}|]$ is a vector of stimulus features including indentation depth (s), rate ($\dot{s}$), and acceleration ($\ddot{s}$), with k lags denoting the number of time lags.

$h_{FR}(.)$ is a nonlinearity of the form $h_{FR}(x) = \begin{cases} x, x > 0 \\ 0, x \leq 0 \end{cases}$ to guarantee that firing rate is always nonnegative;

$h_A(.)$ is a nonlinearity defined by a sigmoid function to capture the observed saturation of activated area at high amplitudes:

$$h_A(x, b) = \frac{b_0}{1 + e^{-b1(x - b_2)}}$$

We estimate parameters of the firing rate model (W_{FR}) using least squares regression and parameters of the area model (W_A, b) using nonlinear optimization with the Levenberg–Marquardt algorithm. We optimized the number of lags k_{1-3} to achieve stable cross-validation performance across all test stimuli with both models (k = 5 for firing rate and k = 2 for activation area).

6.7.4 Conventional Encoding Model

In the majority of sensory feedback algorithms implemented to date in experiments with human amputees (see Clark et al., 2014; Dhillon & Horch, 2005; Graczyk et al., 2016; Stanisa Raspopovic, 2014; Schiefer, Tan, Sidek, & Tyler, 2016; Daniel W. Tan et al., 2014), the firing rate of the nerve $\widehat{FR}_t$ linearly tracks the time-varying stimulus s_t, such that

$$\widehat{FR}_t \propto s_t$$

We used this model as a baseline, linearly scaling it to best fit the simulated response.

6.7.5 Model validation

To test the model, we first assessed the degree to which it could reproduce the time-varying firing rate and activated area of afferent population simulated with TouchSim using a set of parametric stimuli. Specifically, we computed the output of the model to sinusoids varying in frequency and amplitude, noise stimuli with the same spectral profile used to obtain the parameters but with a different random seed, and step indentations varying in duration and amplitude. We then compared this output with the aggregate firing rate computed using TouchSim. The coefficient of determination (R^2) was used to gauge model fit.

Next, we assessed the model performance on stimuli that reproduce those experienced during every day interactions with objects. To this end, we instrumented an adult male participant with a sensorized glove (FingerTPS, PPS, Inc., Los Angeles, CA) with six pressure sensors – one on each fingertip and one on the palm – and had him perform five standard manual tasks: grasping a cup, writing with a pen, typing, clicking a computer mouse and opening a door (for detailed description of the data collection, see Kim, Mihalas, Russell, Dong, & Bensmaia, 2011). The output of each sensor was converted to indentation depth by scaling it to a maximum of 3 mm. We resampled the pressure output from 64Hz to 512 Hz using spline interpolation and filtered the resulting trace with a low-pass cut-off of 5Hz to eliminate high-frequency noise. The resulting trace was used as input to TouchSim and to the biomimetic encoding model. Models were tailored to the location of the projection field, with different sets of coefficients for different sensor locations.

To further test the biomimetic model, we generated a set of synthetic stimuli designed to mimic ADLs in terms of their spectral profile. Specifically, we pooled all ADL samples (n=23) with indentation depths greater than 1 mm and estimated their power spectrum using Multi-taper Power Spectral Density estimate (Chronux, Matlab). We then generated 200 white noise samples, each 10 seconds long, converted them to the frequency domain, adjusted their power spectrum to match that of ADLs, then converted the resulting spectra back to time domain. The code for computing parameters of the biomimetic model is available at http://bensmaialab.org/code/touchmime/.

6.8 References

Augurelle, A.-S. (2002). Importance of Cutaneous Feedback in Maintaining a Secure Grip During Manipulation of Hand-Held Objects. *Journal of Neurophysiology*, *89*(2), 665–671. http://doi.org/10.1152/jn.00249.2002

Bensmaia, S. J., & Hollins, M. (2003). The vibrations of texture. *Somatosensory and Motor Research*, *20*(1). http://doi.org/10.1080/0899022031000083825

Bensmaia, S. J., & Miller, L. E. (2014). Restoring sensorimotor function through intracortical

interfaces: progress and looming challenges. *Nature Reviews Neuroscience*, *15*(5), 313–325. http://doi.org/10.1038/nrn3724

Boretius, T., Badia, J., Pascual-Font, A., Schuettler, M., Navarro, X., Yoshida, K., & Stieglitz, T. (2010). A transverse intrafascicular multichannel electrode (TIME) to interface with the peripheral nerve. *Biosensors and Bioelectronics*, *26*(1), 62–69. http://doi.org/10.1016/j.bios.2010.05.010

Briaire, J. J., & Frijns, J. H. M. (2006). The consequences of neural degeneration regarding optimal cochlear implant position in scala tympani: A model approach. *Hearing Research*, *214*(1–2), 17–27. http://doi.org/10.1016/j.heares.2006.01.015

Brill, N. A., & Tyler, D. J. (2017). Quantification of human upper extremity nerves and fascicular anatomy. *Muscle and Nerve*, *56*(3), 463–471. http://doi.org/10.1002/mus.25534

Brill, N., & Tyler, D. (2011). Optimizing nerve cuff stimulation of targeted regions through use of genetic algorithms. *Proceedings of the Annual International Conference of the IEEE Engineering in Medicine and Biology Society, EMBS*, (Table 1), 5811–5814. http://doi.org/10.1109/IEMBS.2011.6091438

Clark, G. A., Wendelken, S., Page, D. M., Davis, T., Wark, H. A. C., Richard, A., … Hutchinson, D. T. (2014). Using Multiple High-Count Electrode Arrays in Human Median and Ulnar Nerves to Restore Sensorimotor Function after Previous Transradial Amputation of the Hand. *EMBC*, 1977–1980.

Delhaye, B. P. B. P., Saal, H. P. H. P., & Bensmaia, S. J. S. J. (2016). Key considerations in designing a somatosensory neuroprosthesis, *110*(4), 1–7. http://doi.org/10.1016/j.jphysparis.2016.11.001

Dhillon, G. S., & Horch, K. W. (2005). Direct neural sensory feedback and control of a prosthetic arm. *IEEE Transactions on Neural Systems and Rehabilitation Engineering*, *13*(4), 468–472. http://doi.org/10.1109/TNSRE.2005.856072

Dhillon, G. S., Lawrence, S. M., Hutchinson, D. T., & Horch, K. W. (2004). Residual function in peripheral nerve stumps of amputees: Implications for neural control of artificial limbs. *Journal of Hand Surgery*, *29*(4), 605–615. http://doi.org/10.1016/j.jhsa.2004.02.006

Graczyk, E. L., Schiefer, M. A., Saal, H. P., Delhaye, B. P., Bensmaia, S. J., Tyler, D. J., … Tyler, D. J. (2016). The neural basis of perceived intensity in natural and artificial touch, *142*, 1–11. http://doi.org/10.1126/scitranslmed.aaf5187

Grinberg, Y., Schiefer, M. A., Tyler, D. J., & Gustafson, K. J. (2008). Fascicular perineurium thickness, size, and position affect model predictions of neural excitation. *IEEE Transactions on Neural Systems and Rehabilitation Engineering*, *16*(6), 572–581. http://doi.org/10.1109/TNSRE.2008.2010348

Gustafson, K. J., Pinault, G. C. J., Neville, J. J., Syed, I., Jr, J. a D., Jean-claude, J., & Triolo, R. J. (2009). Fascicular anatomy of human femoral nerve: Implications for neural prostheses using nerve cuff electrodes, *46*(7), 973–984. http://doi.org/10.1682/JRRD.2008.08.0097

Johansson, R. S., & Flanagan, J. R. (2009). Coding and use of tactile signals from the fingertips in object manipulation tasks. *Nat Rev Neurosci*, *10*(5), 345–359. http://doi.org/10.1038/nrn2621

Johansson, R. S., & Westling, G. (1984). Roles of glabrous skin receptors and sensorimotor memory in automatic control of precision grip when lifting rougher or more slippery objects. *Experimental Brain Research*, *56*, 550–564.

Johnson, K. O. (2001). The roles and functions of cutaneous mechanoreceptors. *Current Opinion in Neurobiology*, *11*(4), 455–461. http://doi.org/10.1016/S0959-4388(00)00234-8

Kim, S. S., Mihalas, S., Russell, A., Dong, Y., & Bensmaia, S. J. S. J. (2011). Does afferent heterogeneity matter in conveying tactile feedback through peripheral nerve stimulation? *IEEE Trans Neural Syst Rehabil Eng*, *19*(5), 514–520. http://doi.org/10.1109/TNSRE.2011.2160560

Kim, S. S., Sripati, A. P., Vogelstein, R. J., Armiger, R. S., Russell, A. F., & Bensmaia, S. J. (2009). Conveying tactile feedback in sensorized hand neuroprostheses using a biofidelic model of mechanotransduction. *IEEE Transactions on Biomedical Circuits and Systems*, *3*(6). http://doi.org/10.1109/TBCAS.2009.2032396

Ledbetter, N. M., Ethier, C., Oby, E. R., Hiatt, S. D., Wilder, A. M., Ko, J. H., … Clark, G. A. (2013). Intrafascicular stimulation of monkey arm nerves evokes coordinated grasp and sensory responses. *Journal of Neurophysiology*, *109*(2), 580–590. http://doi.org/10.1152/jn.00688.2011

Leventhal, D. K., & Durand, D. M. (2004). Chronic measurement of the stimulation selectivity of the flat interface nerve electrode. *IEEE Transactions on Biomedical Engineering*, *51*(9), 1649–1658. http://doi.org/10.1109/TBME.2004.827535

Mackevicius, E. L., Best, M. D., Saal, H. P., & Bensmaia, S. J. (2012). Millisecond precision spike timing shapes tactile perception. *Journal of Neuroscience*, *32*(44), 15309–15317.

Manfredi, L. R., Baker, A. T., Elias, D. O., Dammann, J. F., Zielinski, M. C., Polashock, V. S., & Bensmaia, S. J. (2012). The effect of surface wave propagation on neural responses to vibration in primate glabrous skin. *PloS One*, *7*(2), e31203. http://doi.org/10.1371/journal.pone.0031203

Marasco, P. D., Kim, K., Colgate, J. E., Peshkin, M. A., & Kuiken, T. A. (2011). Robotic touch shifts perception of embodiment to a prosthesis in targeted reinnervation amputees. *Brain*, *134*(3), 747–758. http://doi.org/10.1093/brain/awq361

Miller, C. A., Abbas, P. J., Nourski, K. V., Hu, N., & Robinson, B. K. (2003). Electrode configuration influences action potential initiation site and ensemble stochastic response properties. *Hearing Research*, *175*(SUPPL.), 200–214. http://doi.org/10.1016/S0378-5955(02)00739-6

Mino, H., Rubinstein, J. T., Miller, C. A., & Abbas, P. J. (2004). Effects of Electrode-to-Fiber Distance on Temporal Neural Response with Electrical Stimulation. *IEEE Transactions on Biomedical Engineering*, *51*(1), 13–20. http://doi.org/10.1109/TBME.2003.820383

Muniak, M. A., Ray, S., Hsiao, S. S., Dammann, J. F., & Bensmaia, S. J. (2007). The neural coding of stimulus intensity: Linking the population response of mechanoreceptive afferents with psychophysical behavior. *Journal of Neuroscience*, *27*(43). http://doi.org/10.1523/JNEUROSCI.1486-07.2007

O'Brien, G. (2016). Biophysical Population Models of the Auditory Nerve.

Raspopovic, S. (2014). Restoring natural sensory feedback in real-time bidirectional hand prostheses. *Science Translational Medicine*, *6*(222), 1–10. http://doi.org/10.1126/scitranslmed.3006820

Raspopovic, S., Capogrosso, M., Petrini, F. M., Bonizzato, M., Rigosa, J., Di Pino, G., … Micera, S. (2014). Restoring Natural Sensory Feedback in Real-Time Bidirectional Hand Prostheses. *Science Translational Medicine*, *6*(222), 222ra19-222ra19. http://doi.org/10.1126/scitranslmed.3006820

Rattay, F. (1989). Analysis of Models for Extracellular Fiber Stimulation. *IEEE Transactions on Biomedical Engineering*, *36*(7), 676–682. http://doi.org/10.1109/10.32099

Saal, H. P. H. P., & Bensmaia, S. J. S. J. (2014). Touch is a team effort: interplay of submodalities in cutaneous sensibility. *Trends in Neurosciences*, *37*(12), 689–697. http://doi.org/10.1016/j.tins.2014.08.012

Saal, H. P. H. P., & Bensmaia, S. J. S. J. (2015). Biomimetic approaches to bionic touch through a peripheral nerve interface. *Neuropsychologia*, *79*(Pt B), 344–353. http://doi.org/10.1016/j.neuropsychologia.2015.06.010

Saal, H. P. H. P., Delhaye, B. P. B. P., Rayhaun, B. C. B. C. B. C. B. C., & Bensmaia, S. J. S. J. (2017). Simulating tactile signals from the whole hand with millisecond precision. *Proceedings of the National Academy of Sciences of the United States of America*, *114*(28), 201704856. http://doi.org/10.1073/pnas.1704856114/-/DCSupplemental

Säfström, D., & Edin, B. B. (2008). Prediction of object contact during grasping. *Experimental Brain Research*, *190*(3), 265–277. http://doi.org/10.1007/s00221-008-1469-7

Schiefer, M. A., Tan, D., Sidek, S. M., & Tyler, D. J. (2016). Sensory feedback by peripheral nerve stimulation improves task performance in individuals with upper limb loss using a myoelectric prosthesis. *Journal of Neural Engineering*, *13*(1). http://doi.org/10.1088/1741-2560/13/1/016001

Talbot, W. H., & Mountcastle, B. (1968). The Sense of Flutter-Vibration : the Human the Monkey of Mechanoreceptive Comparison of Capacity With Response Patterns Aff erents From. *Journal of Neurophysiology*, *31*(2), 301–334.

Tan, D. W., Schiefer, M. A., Keith, M. W., Anderson, J. R., Tyler, J., & Tyler, D. J. (2014). A neural interface provides long-term stable natural touch perception. *Science Translational Medicine*, *6*(257), 257ra138-257ra138. http://doi.org/10.1126/scitranslmed.3008669

Tyler, D. J., & Durand, D. M. (2002). Functionally selective peripheral nerve stimulation with a flat interface nerve electrode. *IEEE Transactions on Neural Systems and Rehabilitation Engineering*, *10*(4), 294–303. http://doi.org/10.1109/TNSRE.2002.806840

Vallbo, A. B., & Hagbarth, K.-E. (1968). Activity from skin mechanoreceptors recorded percutaneously in awake human subjects. *Experimental Neurology*, *21*(3), 270–289. http://doi.org/10.1016/0014-4886(68)90041-1

Veltink, P. H., van AlstÉ, J. A., & Boom, H. B. K. (1988). Simulation of Intrafascicular and

Extraneural Nerve Stimulation. *IEEE Transactions on Biomedical Engineering*, *35*(1), 69–75. http://doi.org/10.1109/10.1338

Weber, A. I., Saal, H. P. H. P., Lieber, J. D. J. D., Cheng, J. W., Manfredi, L. R. L. R., Dammann III, J. F. F., … Bensmaia, S. J. S. J. (2013). Spatial and temporal codes mediate the tactile perception of natural textures. *Proceedings of the National Academy of Sciences of the United States of America*, *110*(42), 17107–17112. http://doi.org/10.1073/pnas.1305509110

Witney, A. G., Wing, A., Thonnard, J.-L., & Smith, A. M. (2004). The cutaneous contribution to adaptive precision grip. *Trends Neurosci*, *27*(10), 637–643. http://doi.org/10.1016/j.tins.2004.08.006

Woo, J., Miller, C. A., & Abbas, P. J. (2010). The dependence of auditory nerve rate adaptation on electric stimulus parameters, electrode position, and fiber diameter: A computer model study. *JARO - Journal of the Association for Research in Otolaryngology*, *11*(2), 283–296. http://doi.org/10.1007/s10162-009-0199-2

Chapter 7 | Conclusions

7.1 Summary of results

The hand is a highly sophisticated and adaptable mechanism that endows humans with an extraordinary ability for interacting with objects in a versatile and effortless manner. This ability stems from the intricate anatomy of the hand and the associated neural circuitry, which allows for precise and coordinated movements. The delicate and intricate finger movements of a pianist while playing a piece, the skilled manipulations of a surgeon during surgery, or the deft movements of a sculptor molding clay, are all testament to the versatility and complexity of the hand as an effector. The objective of this dissertation is to probe the neural mechanisms that mediate hand dexterity through studies of motor (M1) and somatosensory (S1) cortices of non-human primates and then to use these findings to improve brain-computer interfaces for individuals whose manual dexterity was compromised. We focused our attention on grasping behavior (before and after contact with an object) which is one of the fundamental functions of the primate hand.

First, in Chapter 2, we looked at hand preshaping and associated neural responses in the sensorimotor cortex as non-human primates grasped objects of various shapes and sizes. We show that we can accurately decode kinematics pre-contact with a variety of decoding methods from both M1 and S1 even with a small number of neural signals and that different cortical fields carry different amounts of information about hand kinematics. In particular, area 3a contained more information about hand kinematics than areas 1 and 2 of somatosensory cortex before contact with an object was established, which hints at its importance for proprioceptive coding of the hand (Lutz & Bensmaia, 2021; E. V. Okorokova et al., 2020).

Second, in Chapter 3, we investigated whether neural population activity is similar during reaching and grasping, the two behaviors that involve fundamentally different patterns of kinematics and muscle activations. Previously, low-dimensional linear dynamics were observed in neuronal populations of motor cortex when monkeys perform reaching movements (Churchland et al., 2012; Shenoy et al., 2013). Using a variety of analytical approaches, we showed that M1 does not exhibit such dynamics during grasping movements. Rather, the grasp-related neuronal dynamics in M1 are similar to their counterparts in somatosensory cortex, whose activity is driven primarily by afferent inputs rather than by intrinsic dynamics (Suresh et al., 2020).

The first two chapters focused on understanding hand encoding before contact with an object is established. However, most manual behaviors involve interaction with objects, which introduces another variable into play, namely manual forces. To study force and kinematic representations systematically during prehension, we developed a new experimental apparatus that allows us to track both hand movement and contact forces as the monkey grasps objects of various configurations. In Chapter 4, we show weaker force representation in the motor cortex compared to kinematic representation. Nonetheless, decoders that can leverage neural dynamics can reliably extract force information from M1 responses. These findings suggest that M1 encodes kinematics and forces differently.

Drawing inspiration from these findings, we examined the representation of grasp force in individuals with tetraplegia in Chapter 5. Our study revealed a similarly weak force signal in the human motor cortex, but we were able to reliably decode attempted force using a virtual environment grasp task. Like in the monkey study, we found that decoders that utilize non-linear dynamics in neural responses achieved the best offline and online performance. These results demonstrate a similar mechanism of force coding in the motor cortex of monkeys and humans.

The use of our decoder may pave the way for more advanced brain-computer interfaces that can control not only kinematics but also the precise application of forces on the grasped objects.

In Chapter 6, we shift our focus to somatosensory feedback, which is necessary for the smooth control of both biological and prosthetic hands. We explore the possibility of creating nerve stimulation algorithms that mimic biological processes to elicit natural sensations in users of peripheral neuroprosthetics. To achieve this, we implemented a simple model based on a realistic simulation of the nerve (E. V. Okorokova et al., 2020; Saal et al., 2017) to simulate typical manual behaviors, and we tested it on a subject with upper limb amputation (George et al., 2019). Our results indicate that the biomimetic stimulation paradigm enables better hand control than classic stimulation approaches.

The results of this dissertation help us understand neural mechanisms of prehension in monkeys and humans and pave the way to more naturalistic brain-computer interfaces.

7.2 Future directions

There remain a lot of questions outside of the scope of this dissertation. Here we outline some of the main directions that are important to investigate within the context of our experimental setups.

7.2.1 Basic scientific questions

In Chapter 4, we explored the representation of overall force in the motor cortex. However, when we grasp objects, forces are distributed across multiple contacts and may vary based on the hand configuration during grasp. The neural encoding of contact forces of hand segments and their interaction with the kinematics of the same hand segment is yet to be understood.

Our prehension apparatus provides an opportunity to study other areas involved in manual behaviors, particularly the primary somatosensory cortex, which is the main focus of the lab. The

subfields of S1 (areas 3a, 3b, 1, and 2) are responsible for processing information from peripheral tactile and proprioceptive receptors in the hand, making them crucial in understanding the sensorimotor loop involved in prehensile behaviors. By comparing the kinematics and kinetic representations in these areas, we can identify the encoding properties of somatosensory neurons during active touch. Moreover, we can look at communication between motor and somatosensory areas and uncover their functional dependence.

Another intriguing concept that we can explore is our ability to perceive a three-dimensional structure of an object, also known as stereognosis. Stereognosis is believed to rely on the integration of information from proprioception and touch (Delhaye et al., 2018; Goodman & Bensmaia, 2018; Hsiao, 2008; S. S. Kim et al., 2015). Using our setup, we can analyze the influence of kinematic and kinetic variables on the neural responses to identify where and when this convergence arises.

7.2.2 Brain-computer interfaces

In Chapter 5, we focused on grasp force decoding in a task that involved only two degrees of freedom - hand aperture and force. Our next step is to incorporate more degrees of control, such as hand transport and wrist rotation, to make our interface more naturalistic for BCI users. Additionally, we plan to explore individual finger movement and forces, which have not been systematically studied within the BCI setting.

Although our BCI task was performed without any sensory feedback, the control of grasp force in biological hands heavily relies on somatosensory feedback. Therefore, incorporating tactile feedback through intracortical stimulation is one of our next goals. However, we still need to uncover suitable parameters to achieve naturalistic force feedback and determine how to implement electrical stimulation without harming decoder performance.

7.3 References

Churchland, M. M., Cunningham, J. P., Kaufman, M. T., Foster, J. D., Nuyujukian, P., Ryu, S. I., & Shenoy, K. V. (2012). Neural population dynamics during reaching. *Nature*, *487*(7405), 51–56. https://doi.org/10.1038/nature11129

Delhaye, B. P., Long, K. H., & Bensmaia, S. J. (2018). Neural Basis of Touch and Proprioception in Primate Cortex. *Comprehensive Physiology*, *8*(4), 1575–1602. https://doi.org/10.1002/cphy.c170033

George, J. A., Kluger, D. T., Davis, T. S., Wendelken, S. M., Okorokova, E. V., He, Q., Duncan, C. C., Hutchinson, D. T., Thumser, Z. C., Beckler, D. T., Marasco, P. D., Bensmaia, S. J., & Clark, G. A. (2019). Biomimetic sensory feedback through peripheral nerve stimulation improves dexterous use of a bionic hand. *Science Robotics*, *4*(32). https://doi.org/10.1126/scirobotics.aax2352

Goodman, J. M., & Bensmaia, S. J. (2018). The Neural Basis of Haptic Perception. In *Stevens' Handbook of Experimental Psychology and Cognitive Neuroscience* (pp. 1–39). American Cancer Society. https://doi.org/10.1002/9781119170174.epcn205

Hsiao, S. (2008). Central mechanisms of tactile shape perception. *Current Opinion in Neurobiology*, *18*(4), 418–424. https://doi.org/10.1016/j.conb.2008.09.001

Kim, S. S., Gomez-Ramirez, M., Thakur, P. H., & Hsiao, S. S. (2015). Multimodal Interactions between Proprioceptive and Cutaneous Signals in Primary Somatosensory Cortex. *Neuron*, *86*(2), 555–566. https://doi.org/10.1016/j.neuron.2015.03.020

Lutz, O. J., & Bensmaia, S. J. (2021). Proprioceptive representations of the hand in somatosensory cortex. *Current Opinion in Physiology*, *21*, 9–16. https://doi.org/10.1016/j.cophys.2021.04.002

Okorokova, E. V., Goodman, J. M., Hatsopoulos, N. G., & Bensmaia, S. J. (2020). Decoding hand kinematics from population responses in sensorimotor cortex during grasping. *Journal of Neural Engineering*, *17*(4), 046035. https://doi.org/10.1088/1741-2552/ab95ea

Saal, H. P., Delhaye, B. P., Rayhaun, B. C., & Bensmaia, S. J. (2017). Simulating tactile signals from the whole hand with millisecond precision. *Proceedings of the National Academy of Sciences*, *114*(28), E5693–E5702. https://doi.org/10.1073/pnas.1704856114

Shenoy, K. V., Sahani, M., & Churchland, M. M. (2013). Cortical control of arm movements: A dynamical systems perspective. *Annual Review of Neuroscience*, *36*, 337–359. https://doi.org/10.1146/annurev-neuro-062111-150509

Suresh, A. K., Goodman, J. M., Okorokova, E. V., Kaufman, M., Hatsopoulos, N. G., & Bensmaia, S. J. (2020). Neural population dynamics in motor cortex are different for reach and grasp. *ELife*, *9*, e58848. https://doi.org/10.7554/eLife.58848